

Dislocation Density Based Material Model Applied in FE-simulation of Metal Cutting

Dan Wedberg



Dislocation Density Based Material Model Applied in FE-simulation of Metal Cutting

Dan Wedberg

Luleå University of Technology
Department of Applied Physics and Mechanical Engineering

Printed by Universitetstryckeriet, Luleå 2010

ISSN: 1402-1757

ISBN 978-91-7439-126-8

Luleå 2010

www.ltu.se

Abstract

Simulation based design enables rapid development of products with increased customer value in terms of accessibility, quality, productivity and profitability. However simulation of metal cutting is complex both in terms of numeric and physics. The work piece material undergoes severe deformations. The material model must therefore be able to accurately predict the deformation behavior for a large range of strain, strain rates ($>50000 \text{ s}^{-1}$) and temperatures. There exist a large number of different material models. They can be divided into empirical and physically based models. The far most common model used in simulation of metal cutting is the empirical Johnson-Cook plasticity model, JC model. Physically based models are based on the knowledge of the underlying physical phenomena and are expected to have larger domain of validity. Experimental measurements have been carried out in order to calibrate and validate a physical based material model utilizing dislocation density (DD) as internal variable.

Split-Hopkinson tests have been performed in order to characterize the material behavior of SANMAC 316L at high strain rates. The DD model has been calibrated in earlier work by Lindgren *et al.* based on strain rate up to 10 s^{-1} and temperatures up to $1300 \text{ }^{\circ}\text{C}$ with good agreement over the range of calibration. Same good correspondence was not obtained when the model was extrapolated to high strain rate response curves from the dynamic Split-Hopkinson tests. These results indicate that new deformation mechanisms are entering. Repeating the calibration procedure for the empirical JC model shows that it can only describe the material behavior over a much more limited range.

A recalibrated DD model, using varying obstacle strength at different temperatures, was used in simulation of machining. It was implemented in an implicit and an explicit finite element code.

Simulation of orthogonal cutting has been performed with JC model and DD model using an updated Lagrangian formulation and an implicit time stepping logic. An isotropic hardening formulation was used in this case. The results showed that the cutting forces were slightly better predicted by the DD model. Largest error was 16 % compared to 20 % by the JC model. The predicted chip morphology was also better with the DD model but far from acceptable.

Orthogonal cutting was simulated using an updated Lagrangian formulation with an explicit time integration scheme. In this case were two hardening rules tested, isotropic hardening and a mixed isotropic-kinematic hardening. The later showed an improvement regarding the feed force prediction. A deviation of less than 8% could be noticed except for the feed force at a cutting speed of 100 m/min. The time stepping procedure in combination with the mesh refinement seems to be able to capture the chip segmentation quite well without including damage evolution in the material model.

Further works will mainly focus on improving the DD-model by introducing relevant physics for high strain rates.

Preface

This work has been carried out at AB Sandvik Coromant and at Luleå University of Technology with Professor Lars-Erik Lindgren as supervisor and PhD Ales Svoboda as co-supervisor. The financial support was provided by the Swedish Research Council and AB Sandvik Coromant and is gratefully acknowledged. It is highly appreciated to have been giving the opportunity to work with this research project. Thank you all who have been involved and enabled this.

There are many people who in one way or another have contributed to the work of this thesis. To mention everyone is hardly possible, but I wish to express my gratitude to all of you who contributed. However, there are some people to whom I especially would like to express my thanks. First of all I want to thank my supervisor Professor Lars-Erik Lindgren for his enthusiasm, support and friendship during this work. Then I would like to thank my co-authors PhD Ales Svoboda and PhD Vahid Kalhori. Many interesting discussions have taken place. I would also like to thank Professor Veli-Tapani Kuokkala and his research group at the Tampere University of Technology. Special thanks to M.Sc Jari Rämö for good collaboration and sharing of knowledge and experience around the Split-Hopkinson. I also wish to thank the PhD-student Bijish Babu, who like me has an interest in material behavior and modeling, for meaningful discussions and contributions.

Dan Wedberg

Graz, January 2010

Förmågan att idag tänka annorlunda än igår skiljer den vise från den envise.

John Steinbeck

Contents

1	Introduction	1
1.2	Scope of this work.....	2
2	Mechanics of metal cutting	3
2.1	Cutting forces	5
2.2	Tool and chip interaction.....	6
2.3	Heat generation in metal cutting	7
2.4	Chip formation	7
3	Plastic behavior of solid polycrystals	10
3.1	Imperfections in solid polycrystals	11
3.1.1	Point defects	11
3.1.2	Line defects	12
3.1.3	Planar defects	13
3.2	Deformation mechanisms.....	13
3.2.1	Deformation by slip.....	13
3.2.2	Deformation by twinning	16
3.2.3	Deformation via martensite transformation	16
3.2.4	Martensite formation in AISI 316L.....	17
3.3	Consequences of the deformation mechanisms.....	18
3.3.1	Hardening	18
3.3.2	Softening	19
4	Strengthening at high strain rates.....	21
4.1	Strain rate effects on dislocation substructure.....	21
4.2	Dislocation drag	23
5	Constitutive models	26
5.1	Empirical models.....	26
5.2	Physically based models.....	28
6	Dislocation density based model.....	30
6.1	Flow stress.....	30
6.2	Evolution of immobile dislocation density	33
6.2.1	Hardening	34
6.2.2	Recovery.....	35
6.2.3	Generation and migration of vacancies	36
7	Determination of mechanical properties at high strain rates.....	38
7.1	Expanding ring test.....	40
7.2	Taylor and rod impact tests	41
7.3	Split-Hopkinson	42
7.3.1	Split Hopkinson - One dimensional wave equation	44
7.3.2	Dispersion effects and corrections to the one-dimensional wave equation	47
7.3.3	Geometric constraints on dimensions of test specimen in SPHB	49
8	Stainless steels	51
8.1	Ferritic stainless steels.....	52
8.2	Martensitic stainless steels	53
8.3	Austenitic-ferritic stainless steels	53
8.4	Precipitation hardening stainless steels	53
8.5	Austenitic stainless steels	53

9	Distribution of works and summary of results in appended papers.....	54
9.1	Paper A.....	54
9.2	Paper B.....	55
9.3	Paper C.....	56
9.4	Paper D.....	56
10	Conclusions.....	58
11	Future work.....	61
12	References.....	62

Chapter 1

Introduction

Machining is one of the most commonly occurring manufacturing processes within the industry to produce components based on specific requirements. Demand for new products with increased customer value in terms of accessibility, quality, productivity and profitability along with demands for a shorter time to market has lead to that simulations are given a central role in product development cycle. However machining can be characterized as a chip-forming process that is complex in its nature. The chip is formed under severe and rapid deformation in combination with increased temperature due to plastic dissipated energy and friction from the workpiece/tool contacts. Furthermore, the material may undergo various micro-structural changes, which also contributes to the complications. This will of course also depend on the work piece material and its stability. Hence, simulation of metal cutting is complex both in terms of numeric and physics. The physical phenomena may include large elasto-plastic deformation under rapid process, thermo-mechanical coupling, microstructural changes, nontrivial interface between chip and tool and chip formation mechanisms. Hence the material model must be able to adequately represent the deformation behavior as hardening and softening under a great range of strain, strain rate and temperature. Correct description of material behavior is therefore crucial for simulation of metal cutting in order of reliable results for prediction of chip shape, cutting forces, temperature distribution, wear, and surface integrity including residual stresses.

There exist a large number of different material models and many are designed to take into account various phenomena. Material models can be divided into empirical and physically based material models. Empirical models do not take the underlying physical phenomena in account. Equations and parameters are adapted to experimental data by curve fitting. One of the most frequently used models is the Johnson & Cook power law model. Physical models are on the other hand models based on knowledge of the underlying physical phenomena and are expected to

have a larger domain of validity. This is necessary for simulation of metal cutting where strains, strain rates and temperatures vary over a wide range.

Plastic deformation of crystalline metals may occur by different mechanisms and is by no means trivial. Slip is the far most common deformation mechanism where the plastic flow is primarily governed by the motion of dislocations [1, 2]. Results from experimental tests reveal that the stress increases slowly with the logarithm of strain rate for low strain rates up to about 1000 s^{-1} . A marked increase in the strain rate sensitivity has however been noticed in excess of approximately 1000 s^{-1} [3, 4]. This change in rate dependency may be attributed to a change of rate controlling mechanisms. The most common explanation is that dislocation drag becomes dominant. This example illustrates that a model based on a given physics can not be stretched to a larger strain rates without adding the relevant mechanism. However, it is expected to be valid outside its calibration range provided the mechanisms it has been calibrated for are still dominating.

Characterization of the mechanical behavior of metals and alloys are important and can be done by different methods and machines. Available methods are usually grouped into two classes depending if the inertial forces are negligible or not [5, 6]. Conventional testing with screw or servo hydraulic machines are mainly used for quasi-static tests in strain rates range 10^{-4} - 1 s^{-1} [7] while the Taylor test, the Split Hopkinson pressure bar (SHPB) test and the expanding ring test are used for high strain rates. The most widely used test method for high strain rates is SHPB.

1.2 Scope of this work

The aim of this work is to develop validated models for machining. Particular emphasis is placed on the material modeling, which is crucial, and particularly from a physical perspective. The current work has been limited to a stainless steel, AISI 316L, although the models can be calibrated for other metals.

The approach has been to review the literature about flow stress models and phenomena at high strain rates. Furthermore, experimental work has been done to calibrate and validate material models. Experiments have also been performed for orthogonal cutting in order to validate the machining model.

Chapter 2

Mechanics of metal cutting

Metal cutting occurs frequently within the manufacturing industry and can be regarded as the most common and widely used machining operations. The main objective of metal cutting can be described by generation of newly created work surface through removal of unwanted material by a chip removal process. Several industrial applications of metal cutting exist for e.g. turning, milling and drilling. However the principal of metal cutting is the same regardless of application. Generally, a wedge-shaped tool with a cutting edge is moving relative a workpiece material with an overlap. The material that flows towards the cutting edge is instantaneous forced to change flow direction and forming a chip. The wedge-shaped tool consists basically of a tool face (rake face) along which the created chip flows and a flank on the other side of the cutting edge. However, various micro-geometric designs exist. The positioning of the cutting edge is described in relation to the movement of the cutting tool. When the cutting edge is perpendicular to the movement of the tool orthogonal cutting is performed. Otherwise the metal cutting is referred to as oblique cutting, see Figure 2.1.

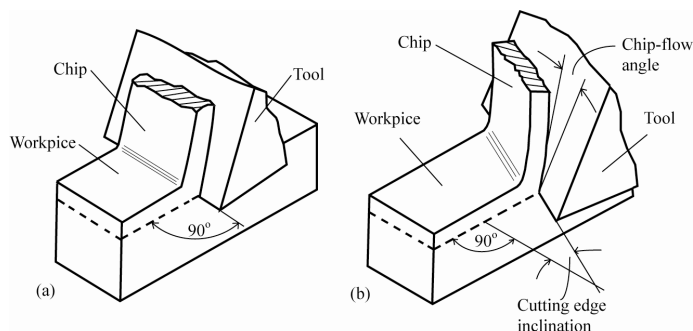


Figure 2.1 – a) Orthogonal and b) oblique cutting, from [8].

well as utilizing the cutting tool in order to meet the requirements on surface integrity, dimensional accuracy and production efficiency. This section aims to introduce the basic of metal cutting.

2.1 Cutting forces

Cutting forces have a great impact on the cutting system and are therefore of great interest. For e.g. cutting forces causes deflections and provide energy to the cutting system which in turn may raise the cutting temperature and/or excite one of structural modes of the system causing vibrations. The latter may be detrimental for the cutting tool and the machined surface. The cutting speed, the feed and the tool angles are some important factors that influence the cutting forces [10, 11, 12].

The acting force on the cutting tool during the cutting process is distributed over the chip-workpiece-cutting tool contact area and may for a turning lathe commonly be divided into three force components, cutting force F_c , feed force F_f and a force in the radial direction. The latter is the smallest of the force components and strive to push the cutting tool outwards in the radial directions. The largest force component is the cutting force which acts in the same direction as the cutting velocity. The feed force acts in the direction of the feed. Figure 2.3 shows the orientation of the forces.

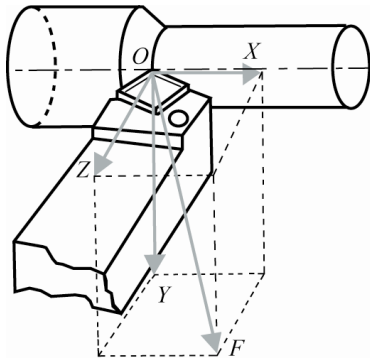


Figure 2.3 – Acting cutting forces on the tool in oblique cutting, Z-radial force, Y-cutting force, X-feed force. From [10].

Cutting tools are not perfectly sharp and some kind of transition, cutting edge, exists. Hence the force in orthogonal cutting is variable distributed along the chip-workpiece-cutting tool contact area. However, the force that acts over the cutting edge and the flank is referred as plowing force and will not contribute to the chip

formation [8]. This effect become more and more pronounced as the feed is reduced.

2.2 Tool and chip interaction

The interaction between tool and chip along their common interface is complex. It is difficult to study and model. Experiments for studying this process in detail and under similar conditions as during cutting is currently not possible. The relative motion between two bodies in contact is opposed by the friction force in the area of contact where the friction behavior is referred to the work by Amonton and subsequent Coulomb. The work states that the friction is proportional to the normal load, independent of the apparent area of contact and independent on the speed of sliding [8, 13]. However, the mean coefficient of friction in metal cutting has been observed to vary with rake angle and cutting speed indicating a behavior that does not follow the classical friction models.

The real area of contact, A_r , under ordinary loading conditions is established between the asperities of the irregular contact surfaces. This area is usually much smaller than the apparent contact area, A_a , giving rise to a metallic contact. The normal pressure is extremely high in case of metal cutting, especially around the tool edge. Pressure up to several GPa has been observed. These circumstances influence the area of contact so that the real area of contact approaches the apparent contact area, $A_r / A_a \rightarrow 1$. The real area of contact becomes independent of the normal load and the ordinary laws of friction are no longer valid. Hence the frictional force will be independent of the normal load. Under these extreme conditions the frictional force becomes the force needed to shear the weaker of the two materials along the apparent area of contact, not at asperities. The interface region where this appears in metal cutting is referred to as the sticking region [8, 10] and occurs adjacent to the tool edge where the normal stress is high. A well established model of the chip-tool friction is shown in Figure 2.4. Further up the tool face where both the normal and the shear stress are lower and have a declining profile a sliding region appears. It should also be mentioned that the interface between the chip and tool affects the heat transfer and thus the amount of heat that may flow into the tool. Good heat transfer is obtained if the real area in the contact interface is large.

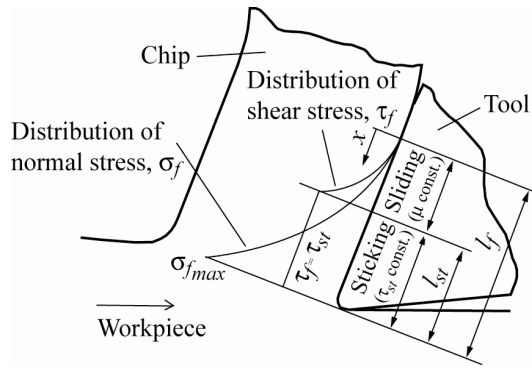


Figure 2.4 – Interaction model between chip and tool in orthogonal cutting where σ_f is the normal stress distribution, τ_f is the shear stress distribution, l_f is the chip-tool contact length, l_{st} is the length of the sticking region. From [8].

2.3 Heat generation in metal cutting

Most of the energy used to deform a material plastically is converted into heat. Since cutting cause large plastic strains, part of the plastic dissipated energy will be converted into heat and increase the temperature in the cutting zone. This will affect the behavior of the work piece material and most probably will its strength and ductility decrease respectively increase and thereby change the metal cutting conditions. Conversion of energy into heat occurs mainly in the primary deformation and the secondary deformation zones. Shear stress from the friction will also contribute to generation of heat in the latter deformation zone. The generated heat will usually dissipate by heat conduction, convection and radiation. However the cutting velocity has a strong influence on the heat conduction in metal cutting. As the cutting speed increases, the time for heat conduction reduces. This produces adiabatic conditions, with sometimes high local temperatures.

2.4 Chip formation

The chip formed in metal cutting depends among others on the cutting process parameter, tool geometry and of the workpiece material being machined - the mechanical properties as well as the thermal properties. The cutting tool thermal conductivity has also shown to have an influence on the cutting forces, contact length, chip form and chip breaking due to temperature gradient in the contact zone [14]. Hence the cutting forces, temperature and strains are directly related to the chip formation and flow [15] and thus chip control is necessary. Although there exist many different shapes of chips they are generally classified as continuous,

continuous with built up edge (BUE), discontinuous, and shear-localized [8, 10, 11]. Formation of continuous chips occurs basically when machining ductile materials under steady-state conditions at relatively high cutting speeds [8, 10] for e.g. mild steel, copper and aluminum. The chip does not move straight up but turns off and goes on sliding along the rake (tool) face before it curls away. Reducing the cutting speed increases the risk of continuous chip with built up edge. In this case the workpiece material welds it self to the tool face which in turn obstruct the following materials and a pile of materials is formed in front of the insert, see Figure 2.5. Hence cutting is now performed outside the cutting edge of the tool with a blunt created cutting edge of the accumulated material and this will most likely leave detrimental footprints on the machined surface and increase the cutting forces [8]. A common action to overcome this is to increase the cutting speed so the built up edge become unstable, breaks down and is carried away by the chip.

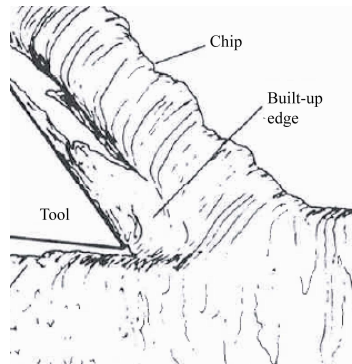


Figure 2.5 – Schematic view of BUE, from [8].

The work piece material in the cutting zone undergoes severe strains. These will, in combination with discontinuities, continuously break the chip into small segments when the critical fracture strain is reached. This is referred to as discontinuous chip formation. This chip form appears usually when machining brittle materials and/or machining with low cutting speeds and high feeds [8]. The final shape, the shear localized chips have a well appearance serrated form on there free surface. These chips contain heavily recurrent deformed shear bands which are a consequence of thermo-plasticity instability. Shear localization starts usually at discontinuities and when the generated heat doesn't dissipate quickly enough the material softens and a localized straining occurs leading to failure. Materials with low thermal conductivity and heat capacity have an increased capability to form these kinds of chips [8, 16]. Likewise machining at very high cutting speed may also cause this chip formation.

Chip formation is fundamental in metal cutting and comprises severe plastic deformations under high strain rates and heat generation. Sometimes it is desirable to examine the workpiece material in the vicinity of the cutting edge in order to study the chip morphology. One useful technique is the quick-stop technique where the cutting process is "frozen" by instantaneous removal of the cutting tool. This technique is usually based on shear-pin design which breaks and removes the tool under an impact load [17].

Chapter 3

Plastic behavior of solid polycrystals

The word "plastic" comes originally from the classical Greek meaning "to shape" [18]. This meaning corresponds well with the remaining deformation that can be observed after plastic straining and unloading of a metallic material. However, it is well known that the shear stress needed to cause plastic deformation of metallic materials is significant lower compare to the theoretical shear stress of a perfect crystal [1, 19] and that the behavior are to be explained by irregularity in the crystal structure disturbing the regular atom structure. The words defects or imperfections are commonly used in order to describe these irregularities. The word defect will henceforth be used. Hence, defects play an important role since they are closely related to the behavior of the material, not always in an adversely way.

Plastic deformation is characterized by permanent deformation at crystal level involving different kinds of mechanism. Metals and alloys are mainly an aggregate of many crystals. During plastic deformation an evolution of the microstructure will take place which impacts the overall behavior of the material. Hence there is a link between the so frequent mentioned stress-strain diagrams on the global scale and the microstructure and its evolution. Good understanding of the structure-sensitive mechanism, their interaction and evolution is indispensable for physical based material modeling. This chapter aims to give a brief introduction into plastic behavior, strain hardening and softening. Firstly, different kinds of defects in the crystal lattice are discussed as they play important roles in plastic deformations. Thereafter some processes or mechanisms are shortly described. Finally, the effects of these processes together with the defects and other microstructural features on the flow stress are discussed. The effects are split into hardening and softening behavior.

3.1 Imperfections in solid polycrystals

The atoms in a perfect crystal are arranged in a regular and repeated three-dimensional array. Several different possible arrangements of the individual atoms exist and hence, different crystal structures exist. Hexagonal close packed (hcp), body-centered cubic (bcc) and face-centered cubic (fcc) are the most common crystal structures in metals.

The original microstructure of the material is principally determined from the solidification process where different grains are formed from the crystallization characterized by solid nucleation and grows [2]. Nucleation starts at many different positions at the same time. The embryos that reach a critical size, will continue to grow along favorable direction into crystalline aggregate where the structure of the grains can differ considerably or be more congruent. In case of great diversity between adjacent grains a high-angle grain boundary is formed characterized with great misfit in crystal orientation. These grain boundaries constitute favorable sites for diffusion, phase transformation, precipitation reactions and obstacles for dislocations and contribute to the properties of the material [2, 20]. They may also acts as sources as well as sinks for dislocations [21]. Hence this will facilitate and contribute to the different phenomenon that occur during plastic deformation and will affect the material's mechanical response. The smaller substructure features, LEDS, discussed in 4.1, can be even more important than the grain boundaries affecting the motion of dislocations. However, this section will focus on different kinds of defects. They are usually divided after their geometrical extension into point, line, planar defects [19, 25] and volume defects [1]. Voids are examples of the latter defect.

3.1.1 Point defects

Point defects are generally associated with a small localized disturbance in the crystal structure as well as the stress field and can be divided into vacancies, interstitials and impurities [1, 19, 23]. Vacancy is an atom site where the atom is missing and an interstitial is when an atom is occupying the space in between the atoms in the regular crystal structure. Vacancies and interstitials can be formed by self-interstitials when atoms from the crystal structure moves to interstitial sites. The concentration of both vacancy and interstitials are affected by the temperature, increase with increasing temperature. However the formation of vacancy is generally favored due to lower energy for formation [1, 19].

Impurities defects are formed by substitutional or interstitial of foreign atoms. The former originates when the original atom is replaced with a foreign atom in the

crystal structure. The differences in size are closely related to the distortion in the crystal structure as well as the activation energy. In case of small or insignificant difference the distortion and activation energy is small. The temperature has a strong influence on formation of point defects. Increasing the temperature increase the probability of forming point defects. Irradiation, plastic deformation and quenching are other ways introducing point defects.

3.1.2 Line defects

Line defects are two-dimensional defects that geometrical can be characterized by a line. The so important dislocation belongs to this category, see Figure 3.1. Two types of dislocations occur frequently in the literature, edge and screw dislocations. Edge dislocations are disruptions in the crystal structure constituted by an extra half plane of atoms squeezed in between the regular atom sequence forming a dislocation line. This extra half plane of atoms cause a distortion and affect the local stress field in a way that compression and tension stresses are created above respectively below the slip plane for a positive edge dislocation. A screw dislocation can be visualized by moving half of the upper part of the crystal to right relative the lower part so that a hack is created on each side. However dislocations do not need to form straight lines or even lie in a single plane. Both types of dislocation may appear together forming a mixed dislocation. To be noted is the difference in the direction of propagation towards direction of applied force.

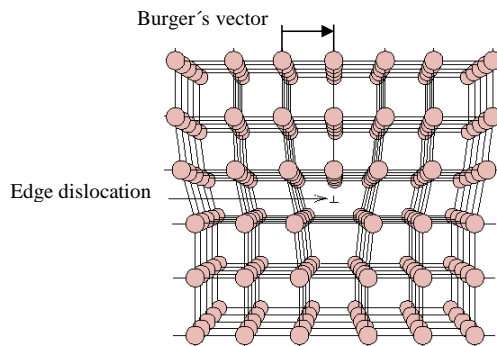


Figure 3.1 – Edge dislocation.

There are a large number of dislocations that have become immobile during the plastic deformation. They contribute to the hardening of the material as discussed later. The density of the moving dislocations is smaller. A dislocation causes a misfit in the lattice. This is a stored energy in the lattice and thus a stored energy is

associated with the dislocation. They form different patterns in order to reduce the total stored energy due their existence. These patterns are called LEDS and are further discussed in section 4.1.

3.1.3 Planar defects

Metals are in their usual form composed of a large number of randomly oriented grains forming a polycrystalline aggregate where each grain has an atom arrangement of a single crystal. The different crystal orientations form a grain boundary which separates the various individual grains. The created crystal structure has its source from the dispersed nucleation and following growth and therefore the extent of miss-fit between the grains may vary. Generally, the miss-fits are defined as Low Angle Grain Boundaries (LAGB) and High Angle Grain Boundary (HAGB) where the tilt and twist boundaries belong to the former group [19, 25]. Other planar defects are twinning and stacking faults [1, 18]. The former is a mechanism where a portion of the crystal structure will form a mirror image of the unchanged crystal structure under applied shear stress. The atom movements are small but a noticeable change in the regular crystal structure appears. Stacking faults is an error in the regular stacking sequence of atom planes. The atoms are not in the expected position they would have with respect to a perfect crystal. The width of the stacking fault is closely related to the energy the stacking fault possesses [2].

3.2 Deformation mechanisms

Plastic deformation of crystalline metals may occur by different mechanisms, slip, twinning and phase transformation [6, 22]. Diffusional creep is another mechanism [20]. However slip is the far most common deformation mechanism, especially at low temperatures [1, 2]. Therefore plastic flow is primarily governed by the motion of dislocations. Slip and twinning are discussed below.

3.2.1 Deformation by slip

Two basic types of movements exist, glide and climb [1]. Slip is a manifestation of many dislocation glides.

The movement of an edge dislocation occurs subsequently by small interatomic distance through out the crystal with Burgers vector perpendicular to the dislocation line. The applied stress is relative low since only the nearest atoms in the continuous plane beside the extra half plane will disconnect and form bonds with the atoms in the extra half plane (dislocation). A screw dislocation move with

Burgers vector parallel to the dislocation line and do not form a unique glide plane. By this a screw dislocation can cross slip onto another slip plane unlike edge dislocations that only move in a specific slip plane, see Figure 3.2.

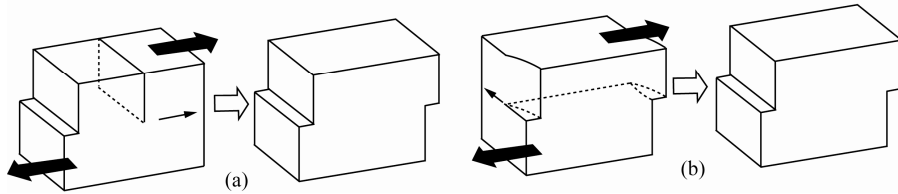


Figure 3.2 – Dislocation movements and final state of deformation for a) edge dislocation and b) screw dislocation. From [25].

In case of absence of point defects the motion of dislocation is more or less limited to glide. However, the crystal structure is rarely perfect, it contains defects that may contribute to as well as prevent dislocation glide. The latter is the case when dislocations get trapped at an obstacle. The ability to cross slip may in this case contribute to the movement. Climb is a thermally activated process which also may assist dislocations to circumvent the obstacle. It occurs by diffusion of atoms and vacancies towards or away from the dislocation [1, 2]. When vacancies or atoms diffuse to dislocations in a way that part of the dislocation line move to an adjacent slip plane, then a jog is created. If diffusion takes place forming a jog in the slip plane, then a kink is formed. Both jogs and kinks are characterized by a step rectangular deviation from the dislocation line, see Figure 3.3. The local stress state around dislocation has an influence on its behavior. The probability that an atom will diffuse from the dislocation increases in case of compressive stresses and vice versa. Jogs and kinks may also be produced when dislocation intersect each other during the movement. For example intersection between two orthogonal edge dislocations with Burgers vector at right angle will form a jog [23].

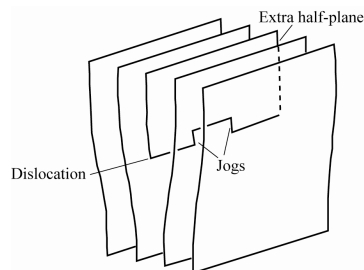


Figure 3.3 – Schematic view of a single jog on an edge dislocation. From [1].

The deformation is seldom homogenous, regions with different orientations are usually formed within the grains characterized by different features. These different heterogeneous features, formed by slip, are shown schematically in Figure 3.4. Shear bands, Figure 3.4a, is a form of plastic instability and are extended across grains and grain boundaries independently of the grain structure. The temperature and the size as well as the orientation of the grains have shown to influence the shear band formation. The ability to shear banding increases with the grain size. Increased temperature has shown to have the opposite effect [24]. Shear bands are commonly seen after rolling. The next scale is grains divided by deformation bands, Figure 3.4b. They form the coarsest subdivision of the grains. In cases where there is a big difference in orientation between the regions, a deformation-induced grain boundary is formed [24]. However deformation bands are consequences of the deformation and the deformation condition and are dependent of the grain orientation, grain size and temperature. Deformation banding is more easily formed in coarsened grains and decreases with increasing temperature [24]. Formation of cell structures is the next feature in the hierarchy, Figure 3.4c, followed by dislocations, Figure 3.4d. Dislocations and cell formation is discussed in section 4.

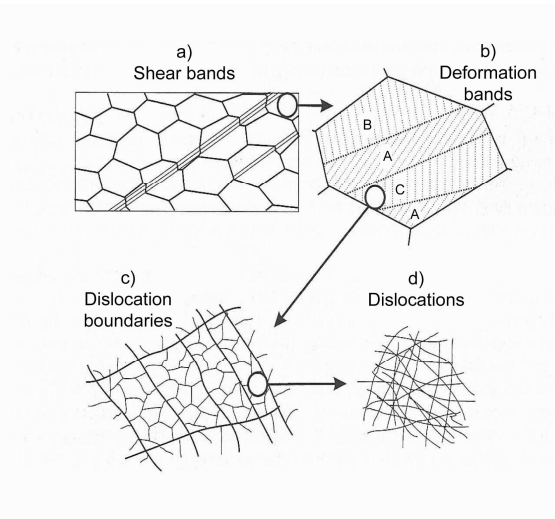


Figure 3.4 – Schematic view of the hierarchy of the microstructure deformed by slip a) shear bands b) deformation bands c) dislocation boundaries d) dislocations. Reference [24].

3.2.2 Deformation by twinning

Twinning is a mechanism where a portion of the crystal structure will undergo a transformation upon shear loading, twin about a mirror plane and forming a mirror image of the undeformed crystal structure. The atomistic mechanism for formation is still unclear [24]. The atom movements are smaller than an atomic distance and takes place on preferable planes and directions [23]. Hence the plastic strain is small. Twinning is more easily developed when slip systems are restricted and hence can be regarded as a low temperature deformation mechanism [23, 25]. However twinning does not only occur during plastic deformation. It may also occur during solid state transformation and annealing. One differs between mechanical and annealing formed twins. Annealing twins may be formed during recrystallisation, recrystallisation and during grain growth [24].

3.2.3 Deformation via martensite transformation

Austenitic stainless steels may go through a transformation where part of the austenitic microstructure transforms into a martensitic structure. This is of particular interest since it increases the work-hardening and affects the ductility of the steel [26, 27]. Spontaneous thermal driven martensite formation during cooling may starts when the temperature sinks below the M_s -temperature. This may occurs in the least alloyed grades [28]. However, deformation induced martensite transformations may starts above the M_s -temperature at much higher temperatures [26, 29, 30]. Estimation of the temperature for which 50% α' -martensite are formed after a true strain of 30% can be done by the following relationship for AISI 316L [29, 30, 31]

$$M_d(\alpha') = 413 - 9.5\%Ni - 13.7\%Cr - 8.1\%Mn - 9.2Si - 18.5\%Mo - 462\%(C + N) \text{ [}^\circ\text{C]} \quad (3.1)$$

Deformation induced martensite is divided into two categories; stress assisted martensite (SAM) and strain-induced martensite (SIM) [29, 32]. Observation reveals, however, that there exist two types of deformation induced martensite with a microstructural diversity, ϵ -martensite (hcp) and α' -martensite (bcc). The former has an hcp structure while the latter is made up of a bcc structure. Nucleation and growth of SAM by aid of the applied stress has been reported [32] to take place in a similar way as the formation of the thermal martensite. Nucleation of α' -martensite is well established to take place at intersections of shear bands [26, 27, 32, 33]. The growth occurs by nucleation and coalescence. The plastic deformation behavior is influenced by the stacking fault and the stacking fault energy should therefore have a considerable influence on the α' -martensite since it nucleates at intersected shear bands. Further, stacking fault energy depends among other things on temperature

and alloying likewise α' -martensite formation. Generally, the ability to form α' -martensite depends strongly on the alloying, temperature and strain rate as well as strain. Results in [27] showed that the fraction of α' -martensite increase with strain and decreases with increasing temperature and alloying. The effects of strain rate was similar to the effects of temperature for the stainless steel AISI 301LN while it was inversely at small strains for AISI 304. The latter results were consistent with the results in [26] for steel grade AISI 304LN. There increased strain rate generated more α' -martensite as more shear bands was formed at the higher strain rate. This is counteracted by the increase in temperature due to the plastic dissipation at higher rates as the time for heat conduction is too short. This is called adiabatic heating. Results presented in [26] revealed that the α' -martensite formation is suppressed due this adiabatic heating despite an increase in shear bands. The grain size has also an effect on the formation on α' -martensite. More α' -martensite was found in coarse-grained specimens of AISI 304LN [26, 32]. The strengthening effects were also higher compared to fine-grained specimens.

3.2.4 Martensite formation in AISI 316L

The stacking fault of the stainless steel AISI 316L is low as well as the M_d -temperature. Chemical composition according to EN 10088-1:2005 (E) gives a M_d -temperature of -35 °C based on the equation (3.1). The M_s -temperature is even lower and the grade is stable regarding spontaneous martensite transformations [28]. However the chemical composition and the temperature have a large influence on the stacking fault energy [27]. During deformation the stacking fault may even change, increase with strains and temperature [27]. This would generally reduce the M_d -temperature and suppress the α' -martensite. Presented results in [32] for AISI 316 showed that no α' -martensite is formed under tensile testing but it also reveals that the deformation mode is important. α' -martensite was formed under a rolling operation, increased with increasing strains. The grain size was also reported to influence during this deformation mode. The volume fraction martensite increased with the grain sizes. However measurements of the magnetic phase of the original material and of a deformed test specimen showed only an insignificant increase in the magnetic phase. The magnetic phase increases from 0.25 % to maximum 1.20 % at a strain rate of 8143 s⁻¹. Martensite formation is more common in metastable austenitic steels where austenite is more easily transformed into martensite.

3.3 Consequences of the deformation mechanisms

The different phenomena discussed in previous sections contribute to the plastic deformation of polycrystals. The effect can be an increase in flow stress, hardening, or decrease in flow stress. This is discussed next.

3.3.1 Hardening

Plastic deformation may take place due to several mechanisms. Different slip systems exist and several mechanisms will occur simultaneously to prevent motions. Dislocation and their motions have a pivotal role. At temperatures lower than approximately $0.5 T_m$ the plastic deformation is primarily governed by slip [2]. The plastic strain rate is proportional to the density of mobile dislocations. However, they become immobilized as they encounter different types of obstacles. These may be grain boundaries, precipitates or other immobile dislocations. Then a higher stress is required in order to create more moving dislocations in order to maintain the plastic deformation. This is the basic mechanism underlying what is called strain hardening or work hardening.

Solid solution and precipitates are examples of point defects that may restrict the dislocation motion. To pass by the dislocation have to climb over, move between or cut through. In case of the latter precipitations are divided into smaller particles with lower resistance for the subsequent dislocations. The splitting may produce cycling softening [2].

When crystals with different orientation form a polycrystalline aggregate, then restraining effects are imposed by the surrounding grains. Thus, dislocations are held up at grain boundaries. It has also been shown that more slip systems are active at grain boundaries and that grain boundary acts as dislocation sources contributing to strain hardening [2, 20]. This observation, that the flow stress is inverse proportional to the square root of the grain size is called the Hall-Petch effect. The grain size has also an effect on the twinning threshold stress, decrease with increasing grain size [34].

Taylor proposed 1931 that the dislocation density constitutes the most important strengthening parameter [2]. It has however been shown that dislocation seldom are uniformly distributed. Dislocation tends instead to form low energy dislocation structures (LEDs). They may form subcells, with high-density-dislocation tangles in the cell walls, and subgrains as deformation proceeds [1, 2, 23]. The size of these cells will then affect the flow stress more than the grain size, as they are smaller than the grains.

3.3.2 Softening

During plastic deformation the microstructure of the material undergoes changes. Most of the work done by the external loads will dissipate as heat and only a small portion of the work will be stored in the material. This stored energy works as driving force for restoration. Restoration is a concept that involves both recovery and recrystallisation. These are competing processes driven by the same stored energy. Hence the extent of recovery depends how easy recrystallisation can occur [24]. Recovery is usually divided into static and dynamic recovery where the latter mechanism competes and counteracts with the hardening during plastic straining [2]. Recovery and recrystallisation is discussed below.

Recovery involves reduction of dislocations, stresses and the local energy level [2] and is very much affected by the temperature. Remobilization of dislocations is also enhanced by thermal activation. Higher temperatures increase the mobility of vacancies and dislocations. Slip is however a process that likewise annihilates dislocation segments at low temperatures. Two primary processes exist, annihilation and rearrangement of dislocations [24]. Recovery is a process that consists of several events. It involves annihilation of dislocations, formation of cells, formation of subgrains and grain growth. Climb is a process that together with glide enables annihilation of dipoles which requires thermal activation. In the high temperature regime the climb is governed by lattice diffusion of vacancies while core diffusion is suggested to govern at intermediate temperatures [35]. However one separates between dynamic and static recovery. Dynamic recovery is active during the deformation while static recovery operates after the deformation and when the external loads have been removed. In the former case, the existing stress field due to the external loads will contribute to the rearrangement of the dislocations into a lower energy structure as well as to their annihilation [2]. Dynamic recovery may occur at lower temperatures than static recovery. An example of dynamic recovery is the change from dislocation tangles to cells that may occur during deformation in many materials. However, to be noted, stacking faults are important for the recovery. It affects the dislocation climb and the cross slips and hence obstructs the recovery process in metals with low stacking fault energy. Another influencing factor is solutes. Solutes may affect the stacking fault energy. But they have also a direct effect like pinning of dislocations and affecting the concentration and mobility of vacancies [24]. Recrystallisation involves nucleation and growth of new grains [36] with a reduced dislocation density. The driving force is the stored energy due to the immobile dislocations interior of the grains. They form subcells that, with increasing immobile dislocation density, is defined as subgrains as their misorientations with the rest of the lattice increases. Then it may be more energy efficient for the

microstructure to form new, smaller grains with a lower dislocation density in their interior. The existing immobile dislocations then go into the grain boundary and the reduction in stored energy is driving the process. The deformation needs to exceed a certain limit before recrystallisation start. The higher dislocation density, the lower temperature is required for recrystallisation [19]. The sizes of the newly created grains are influenced by the existing immobile dislocation density as well as current temperature. However increased temperature increases the risk of unfavorable grain growth, which affects the ductility negatively. Otherwise, the recrystallisation increases the ductility. Recrystallisation occurs at temperatures above approximately $0.5 T_m$ in alloys [19]. Grain boundaries, transition bands, shear bands and twins are examples of inhomogenities that trigger recrystallisation.

Chapter 4

Strengthening at high strain rates

Several experimental tests have been performed on different metals and alloys in order to characterize the mechanical response at different strain rates and temperatures. Results reveal that the stress increases slowly with the logarithm of strain rate for low strain rates up to about 1000 s^{-1} . A marked increase in the strain rate sensitivity has however been noticed for strain rates higher than approximately 1000 s^{-1} [3, 4]. The rate dependency can be attributed to different rate controlling mechanism. The significant increased strain rate sensitivity has been interpreted as change in controlling deformation mechanisms. The authors in [3] attributes this to increased dominance of dislocation drag mechanism. Others [4] discuss enhanced rate of dislocation and twin generation as possible explanations. Formations of subcells, subgrains and martensite are other parameters affecting the behavior of steels that may contribute to the observed enhanced rate sensitivity of the flow stress. These effects were discussed in section 3.2.3 and 3.2.4.

4.1 Strain rate effects on dislocation substructure

The role of defects and different deformation mechanisms were discussed in sections 3.2. The focus in the current work is on dislocation motion as the important contribution to plastic deformation. It is observed that dislocation may form coplanar arrays during the early stage of plastic deformation. The plastic straining leads to a nonuniform dislocation low energy dislocation structure (LEDS). The dislocations may form subcells, with high-density-dislocation tangles in the cell walls, and subgrains as deformation proceeds [1, 2, 23]. Other configurations of the LEDS are also possible. The driving force for the cell formation has been recognized as the strain energy and its efforts of finding a lower energy state. The dislocations must have sufficient mobility to organize into the LEDS configurations. Hence the stress, temperature, elastic constants and the stacking

fault energy will all have an important influence [37]. Kuhlman-Wilsdorf [38] writes that *dislocation structures are always as close to thermodynamical equilibrium as the constraints of limited mobility and geometry of slip system permit*. Holt [37] starts out from the interaction energy between the dislocations and derives a relation between the dislocation cell diameter and the dislocation density according to

$$s = K_c \rho_i^{-1/2} \quad (4.1)$$

where K_c is constant. However the equation is not valid when the dislocation mobility is low or high. Michel *et al* [39] investigated the temperature influence on the evolution of the substructure in the stainless steel AISI 316. A gradual increase in the cell diameter could be notice up to $\sim 0.5 T_m$ where a transition from cell structure to subgrains could be observed causing a significant increase in the measured diameter with increasing temperature. Increased recovery effect promoted by increasing temperature was mentioned as reason for the rapid increase in the subgrain diameter. K_c was found to be 16 for temperatures above 704°C. Hence temperature sensitivity has been noticed. Studies performed on Cu showed that that the dislocation cell size decreases and converge towards a critical value when the strain increases [40, 41].

It has been observed in some studies that an increase in temperature has the same influence on rate dependent phenomena as a decrease in strain rate and vice-versa. The effects of strain rate on dislocation cell formation have been studied by Sil and Varma [42], Rao and Varma [43] and Shankaranarayan and Varma [44] for the fcc metals Al, Ni and Cu in the strain rate range $1.7 \cdot 10^{-4} - 8.3 \cdot 10^{-2} \text{ s}^{-1}$ in a tensile testing machine. One unexpected observation in Ni was that smaller dislocation cells were observed at smaller strain rates and as the strain rate increased their size increase but also that the cell walls become less sharp. Increase in size of cell walls with strain rate was also observed in Al for strain rates up to $\sim 4 \cdot 10^{-3} \text{ s}^{-1}$ but as the strain rate increased further, then the dislocation cell size started to shrink again. In Cu with the lowest stacking fault energy of the three metals the cell size decreased initially with increasing strain rate but started then to increase as the strain rate increased. This is however contrary to expected results in [40]. Hence the strain rate seems to have an impact on the cell evolution but in various ways. Other notable observation was that smaller cell sizes could be observed in smaller grain sizes and vice versa which also have been observed in [40]. In [45] was the microstructure evolution examined for AISI 4340 at higher strain rates ranging from $2 \cdot 10^{-2} - 4.4 \cdot 10^3 \text{ s}^{-1}$. The results revealed that the strain rate has an influence on

the evolution of the dislocation formation and it was observed that the dislocation cell size was reduced with increasing strain rate.

However, it would be expected that increased strain rate will affect the time-dependent dynamic recovery. Cheval and Priester [46] compared the evolution of the dislocation structure in Cu for low and high strain rates, $5 \cdot 10^{-4}$ respectively $2.5 \cdot 10^3 \text{ s}^{-1}$, and observed a significant difference. In contrast to the dynamic deformation a well defined dislocation cell structure was developed with increasing strains in the case of the static deformation. Most of the cell structure had however vanished after 65 % compression strains. The conclusion was that the dislocations do not seem to manage to recover to lower energy cell formations during dynamic deformations.

4.2 Dislocation drag

Many metals and alloys have been reported to have a significant increase in the strain rate sensitivity of the flow stress. This is usually observed around 1000 s^{-1} [3], see beginning of section 4. This marked increase in flow stress is often in the literature attributed to a change in the dominated deformation mechanism. It changes from thermal activation control of dislocation at low strain rates to dislocation drag effects at high strain rates [47, 48, 49, 50, 51]. The latter has a retarding effect on the moving dislocations and therefore a larger stress is required to maintain a high strain rate.

The resistance to the movement of dislocations may be considered from a viscous perspective. Hence, the dislocation drag coefficient may be defined from a Newtonian viscous material according to

$$f_v = Bv \quad (4.2)$$

where f_v is the force acting on a unit length of a dislocation, B is the viscous damping coefficient and v is the dislocation velocity [52]. Dislocation drag is a process that prevents dislocations motion through interaction with phonons and electrons [53]. In addition to phonon drag and electron drag movement of dislocations may under certain circumstances be counteracted by a third mechanism. Moving dislocations may emit or absorb phonons and this result in something called radiation drag [54]. Hence the overall dislocation drag process may be described by

$$B = B_p + B_e + B_r \quad (4.3)$$

where B_p is the phonon drag, B_e is the electron drag and B_r is the radiation drag. Phonon drag is temperature dependent in contrast to what electron drag and radiation drag are. When the temperature decreases the density of phonons is reduced and this will affect its activity and hence affect the drag coefficient. If the temperature drops much it may thereby affect the dominant mechanism so the electron drag will for example become dominant [54].

The movement of dislocations for low strain rates is dominated and controlled by short range obstacles. Thermal activated vibration will together with the applied stress help the dislocation to pass the obstacle. Thus a higher temperature requires a lower stress for a given strain rate. If the stress is high enough, then it is assumed that the dislocations may emancipate themselves and the movement becomes solely limited by dissipative drag mechanisms. It was early shown that the critical resolved shear stress for single aluminum crystals was a linear function of the strain rates for very high strain rates, 10^4 s^{-1} and it was believed to be due to the drag forces [52]. The flow stress in the high strain rate damping region was modeled by the equation

$$\tau = \tau_G + \tau^* + \tau_D \quad (4.4)$$

where τ_G is the athermal stress, τ^* is the required thermally activated stress component for overcome obstacles and τ_D represent the stress attributed to the dislocation damping which in a perfect crystal was attributed to phonons and electrons. The damping term is negligible at low strain rates but becomes significant with increasing strain rates and is dominating at very high strain rates [52]. The strain rate sensitivity becomes attributed to viscous damping. The strain rate sensitivity for copper was divided into thermally activated region ($<10^2 \text{ s}^{-1}$) and viscous damping region ($>10^3 \text{ s}^{-1}$). This definition of flow stress has also been used for modeling the deformation behavior of Nitronic-50 and AL-6XN stainless steels of others [50, 51]. In these cases it has been assumed that the viscous drag component is a function according to

$$\tau_D = g \left(\frac{M^2 B}{(\rho_m b^2)}, \dot{\gamma} \right) = m_0 [1 - e^{-\alpha \dot{\gamma}}] \quad (4.5)$$

where M is the Taylor factor, B is the drag coefficient, ρ_m is the mobile dislocation density, b is the magnitude of the Burgers vector, $\dot{\gamma}$ is the shear strain rate and m_0 is a material constant.

However, all researchers do not agree that the observed and significant increase in the strain rate sensitivity is caused by dislocation drag. The frequently used linear relationship for high strain rates is according to [55] an inadequate description due to the use of strain as a state variable without allowing the historical impacts and since the strain rate sensitivity is much higher than the actual constant-structure strain rate sensitivity. Follansbee and Kocks [55] claim that the increased strain rate sensitivity observed in copper and other metals with fcc structure is an artifact. Evaluation and comparing of stress at constant strain is not preferable since strain is not a proper state variable in this case. If instead the comparison is made on basis of the mechanical threshold stress or the flow stress at 0 K as state variable, then no significant increase in strain rate sensitivity can be observed. This has been shown for copper for strain rates up to 10^4 s^{-1} . Hence the transition in controlling deformation mechanism, from thermally activated to dislocation drag, that often is reported does not occur according to Follansbee and Kocks for strain rates below 10^4 s^{-1} . This has also been reported in [56]. Studies of deformation of 304L stainless steel showed that the strain rate had a strong influence on the stress response. The increased strain rate sensitivity that was observed around 10^3 s^{-1} was declared to be an effect of enhanced rate of dislocation generation [47] and not due to dislocation drag effects.

Chapter 5

Constitutive models

Constitutive models describing the relation between the stress and strain are needed to describe e.g. the stress state in a material. The model should be able to describe the strain dependence, strain-rate dependence, temperature dependence and the deformation history in order to handle the complex phenomena work-hardening and thermal-softening. The constitutive models are generally divided into empirically and physically based models. Empirically based models are solely based on fitting a function to existing data without any underlying physical interpretation and theoretical basis. Therefore empirical models are limited and are mainly used for prediction of behavior within the range of experimental data. Hence extrapolation outside the range is unreliable. Physically based models, on the other hand, consider the underlying physical processes that have been discussed in the previous chapter. Physical based models can be extrapolated outside the range of data used for calibration of the models provided that the mechanisms included in the models are still dominating the behavior.

5.1 Empirical models

There exist several empirical models of which some are described here.

Hollomon (1945) [57] proposed the following relation, also referred as Ludwik relation [58, 59] or the Ludwik-Hollomon relation [60], between true stress and true plastic strain

$$\sigma = K \varepsilon^p{}^n \quad (5.1)$$

where ε^p is the plastic strain, K and n are material constants. Ludwigson [58] observed however that the relation could not describe the behavior of austenitic

stainless steels at low strains well and therefore proposed a correction term Δ to account for the deviations at low strains. The modified equation, [58, 59], is written

$$\sigma = K_1 \varepsilon^{p^{n_1}} + \Delta \quad \text{where} \quad \Delta = e^{(K_2 + n_2 \varepsilon^p)} \quad (5.2)$$

This equation has shown capability to describe the plastic behavior of nickel free high nitrogen steels as well as 316L and 316 LN with different nitrogen contents at room temperature and at a certain constant strain rate [58, 59]. An extended hardening model proposed by Ludwik [60] is given by

$$\sigma = \sigma_0 + K \varepsilon^{p^n} \quad (5.3)$$

where σ_0 are the yield strength, K and n are material constants.

A commonly used model, particularly for high strain rates, is the Johnson and Cook model. Temperature and strain-rate effects are included in the model. It is a multiplicative composition of a strain-hardening term, strain-rate sensitivity term and a thermal-softening term. The flow yield stress is given by

$$\sigma = (A + B \varepsilon^n) (1 + C \ln \dot{\varepsilon}^*) (1 - T^{*m}) \quad (5.4)$$

where ε is the equivalent plastic strain, $\dot{\varepsilon}^* = \dot{\varepsilon} / \dot{\varepsilon}_0$ is the dimensionless plastic strain rate, $\dot{\varepsilon}_0$ is the reference plastic strain rate, T^* is the homologous temperature defined as

$$T^* = \frac{T - T_r}{T_m - T_r} \quad (5.5)$$

where T_r is the reference temperature at which yield stress is measured and T_m is the melting temperature of the material [61]. The five parameters, A , B , C , m and n are determined by means of curve fitting. Some optimized values from different researchers are presented in Table 5.1 for material 316L [62].

Table 5.1 – Optimized material parameters from different researchers [62], material 316L.

	A	B	C	n	m	$\dot{\varepsilon}_0$
1	305	1161	0.01	0.61	0.517	1
2	305	441	0.057	0.1	1.041	1
3	301	1472	0.09	0.807	0.623	0.001
4	280	1750	0.1	0.8	0.85	200
5	514	514	0.042	0.508	0.533	0.001

However there exist several modifications of Johnson-Cook model. Andrade *et al* incorporated a fourth term with respect to consider dynamic recrystallisation [20]. For increased strain rate sensitivity following modified model [63] has been proposed

$$\sigma = (A + B\varepsilon^n)(\dot{\varepsilon}^*)^\alpha (1 - T^{*m}) \quad (5.6)$$

where α is an empirical exponent. However, the strain rate sensitivity is not significantly enhanced so Rule [63] proposed a revised model

$$\sigma = (C_1 + C_2\varepsilon^n) \left(1 + C_3 \ln \dot{\varepsilon}^* + C_4 \left(\frac{1}{C_5 - \ln \dot{\varepsilon}^*} - \frac{1}{C_5} \right) \right) (1 - T^{*m}) \quad (5.7)$$

for increased strain-rate sensitivity in regimes where needed while keeping the strain-rate behavior in satisfactory regimes. Another modification of the Johnson-Cook model for increased strain-rate sensitivity [64] is

$$\sigma = (A + B\varepsilon^n)(\dot{\varepsilon}^{*C}) (1 - T^{*m}) \quad (5.8)$$

Hung and Liang [65] proposed a modification in the thermal-softening term according to

$$\sigma = (A + B\varepsilon^n)(1 + C \ln \dot{\varepsilon}^*)(D - ET^{*m}) \quad (5.9)$$

5.2 Physically based models

The physically based models are usually characterized after how they have been developed. They can be divided into explicit or implicit physical models. Explicit physical models include the physical model as an evolution equation in the constitutive formulation. An example of this is discussed in the next chapter. In implicit models the constitutive equation is determined based on the knowledge about the physical process. However plasticity as phenomena is complex. The approach used here is referred as "model-based-phenomenology" [53]. A well-known implicit physical based model is the Zerilli-Armstrong model. They [66] noticed a difference in the area of activation between bcc and fcc metals and proposed two different models in order to take into account the observed different behavior of fcc and bcc metals. Both models include a thermal and an athermal term. A third term was added in order to take in account the grain size dependence. The fcc-model is given by

$$\sigma = \Delta\sigma'_G + C_2 \bar{\epsilon}^{1/2} e^{(-C_3 T + C_4 T \ln \dot{\bar{\epsilon}}^p)} + k g^{-1/2} \quad (5.10)$$

where g is the average grain size diameter, $\Delta\sigma'_G$, k , C_2 , C_3 , C_4 is material parameters.

Chapter 6

Dislocation density based model

Dislocations and their movements have a crucial role in plastic deformation. They may move by slip in preferable slip planes or in a non-conservative motion out of the slip plane by climb. The latter are related to diffusions of vacancies and/or atoms and hence is favored by thermal activation. During the movement dislocations interact with other imperfections, precipitates, grain boundaries, sub-cells etc and obstructing the motion. The local internal stresses in the lattice may also hinder or contribute to further motion. Dislocations may also annihilate by interaction with other dislocations or grain boundaries. Bear in mind that dislocations as well as vacancies are created during deformation.

This model is a phenomenological based model where the evolution of dislocation density and vacancy concentration are used to describe the hardening/softening behavior of the material. The movements are assumed to take place by glide and climb. The model uses the dislocation density and vacancy concentration as internal state variables for calculation of the evolution of the structure. Kinematics hardening, twinning, crack nucleation and growth are not considered. The dislocation model that has been used in papers A, C and D in this thesis is presented below.

6.1 Flow stress

The stress required to move dislocations is split into two contributions, one short range and one long-range component. The distortion of the lattice due to existing dislocations and other defects makes it more difficult to move dislocations, i.e. drive a plastic deformation. If the lattice disturbance is over a smaller region, then the driving stress may be assisted by thermal vibrations that may help the dislocation to move on. However, if the lattice distortion is distributed over a larger region, then the stress needed to drive the dislocation motion must be

sufficient large on its own. This stress component is the long-range or athermal contribution to the flow stress.

The flow stress is then written as [53, 67]

$$\sigma_y = \sigma_G + \sigma^* \quad (6.1)$$

where σ_G and σ^* are the long range respectively the short-range contributions. The first component, σ_G , is due to the dislocation substructure. The second component, σ^* , is the explicit rate dependent stress contribution needed for the dislocation to pass through the lattice and to pass short-range obstacles where thermal activation may assist to overcome these obstacles.

The opposing long-range stress component is written as

$$\sigma_G = m\alpha Gb\sqrt{\rho_i} \quad (6.2)$$

where m is the Taylor orientation factor, α is a proportionality factor, G is the temperature dependent shear modulus, b is the magnitude of Burgers' vector and ρ_i is the immobile dislocation density. The basic mechanism of dislocation glide for plasticity is a shearing process. Usually, the fundamental relations used in the current models are expressed in terms of shear stress and strain. The Taylor factor translates the effect of the resolved shear stress in different slip system into an effective stress quantity for a polycrystal without texture. It depends on the kind of lattice in the metal. It does change with deformation but this is neglected in the current work.

When the dislocations are moving through the lattice, they encounter obstacles. The strain rate is dependent on their average velocity. It is assumed that the time for the dislocation to move from one obstacle to another, flight time, is small compared to the waiting time. The latter is the time when a dislocation is near an obstacle trying to bypass it. The stress is assisted by a driving energy due to the thermal vibrations. These vibrations are fluctuation in the lattice and the probability for the energy distribution for a given temperature is described by an Arrhenius expression. Thus it will take some time, i.e. oscillations, before the dislocation will bypass the obstacle. The mean velocity is therefore given by the kinetic equation [53]

$$\bar{v} = \beta b v_a e^{-\Delta G / kT} \quad (6.3)$$

where β is a dimensionless constant, b is the magnitude of Burgers' vector, v_a is the attempt frequency related to the oscillations in the lattice, ΔG is the activation energy, k is the Boltzmann constant and T is the absolute temperature. The plastic strain rate and the velocity of the dislocation motion is related via the Orowan equation

$$\dot{\epsilon}^p = \frac{\rho_m b \bar{v}}{m} \quad (6.4)$$

Combining equations (6.3-6.4) gives

$$\dot{\epsilon}^p = \frac{\rho_m \beta b^2 v_a}{m} e^{-\Delta G / kT} = f(\sigma) e^{-\Delta G / kT} \approx \dot{\epsilon}_{ref} e^{-\Delta G / kT} \quad (6.5)$$

The last step above implies that we simplify the stress dependency of the immobile dislocation density.

The motion of the dislocations in thermally activated glide is facilitated by the contribution of thermal activation energy if the stress in itself is insufficient to drive the dislocation pass an obstacle. The required energy to overcome an obstacle depends on its energy barrier that has a magnitude and a profile. The total energy is the area under the curve between x_1 and x_2 as shown in Figure 6.1. However when the dislocation has reached x_1 , it has reached the obstacle. To overcome the barrier and to reach x_2 additional energy is needed. The required thermal energy is the total energy minus the mechanical energy.

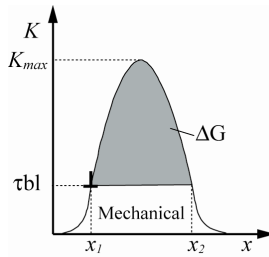


Figure 6.1 – Profile of obstacles resistance.

A general expression for the activation energy is [67]

$$\Delta G = \Delta F \left[1 - \left(\frac{\sigma^*}{\sigma_{ath}} \right)^p \right]^q \quad 0 \leq p \leq 1, \quad 1 \leq q \leq 2 \quad (6.6)$$

where ΔF is the necessary activation energy in order to overcome the obstacles in absence of external stress, $\sigma_{ath} = \tau_0 G$ is the required athermal flow stress for passing the obstacles without aid of thermal energy, p and q determine the shape of the barrier. The activation energy $\Delta F = \Delta f_0 G b^3$. Some guidelines regarding Δf_0 and τ_0 are given in Table 6.1 where l denotes the mean spacing between the obstacles. Combination of equation (6.5) and (6.6) gives after rewriting the short-range stress component

$$\sigma^* = \tau_0 G \left[1 - \left[\frac{kT}{\Delta f_0 G b^3} \ln \left(\frac{\dot{\epsilon}^{ref}}{\dot{\epsilon}^p} \right) \right]^{1/q} \right]^{1/p} \quad (6.7)$$

where $\dot{\epsilon}^{ref}$ is the reference strain rate.

The basic components for the yield stress in equation (6.1) are obtained from equation (6.2 and 6.7). Additional equations for the evolution of the immobile dislocation density are however needed. These are described in the next section.

Table 6.1 - Activation energy factor and shear strength for different obstacles [53].

Obstacle strength	Δf_0	τ_0	Example
Strong	2	$> \frac{b}{l}$	Strong precipitates
Medium	0.2-1.0	$\approx \frac{b}{l}$	Weak precipitates
Weak	< 0.2	$<< \frac{b}{l}$	Lattice resistance

6.2 Evolution of immobile dislocation density

The evolution of the structure is considered to consist of a hardening and a recovery process. The used model assumes that the mobile dislocation density is stress and strain independent and much smaller than the immobile ones [68]. Hence the evolution equation is written

$$\dot{\rho}_i = \dot{\rho}_i^{(+)} + \dot{\rho}_i^{(-)} \quad (6.8)$$

where index i denotes the immobile dislocations.

6.2.1 Hardening

The mobile dislocations may during their movements become immobilized or annihilated. However they are assumed to move an average distance Λ (mean free path) before immobilization or annihilation. The mean free path depends on the distribution of the different obstacles as well as their types. It is well known that grain boundaries acts as obstacles and sinks and also that subcells may stop moving dislocations. Here the mean free path is assumed to be a combination of the distance between grain boundaries, g , and dislocation subcell diameter, s , as

$$\frac{1}{\Lambda} = \left(\frac{1}{g} + \frac{1}{s} + \text{others} \right) \quad (6.9)$$

where "others" denotes possible contributions from varying types of obstacles like precipitates. The well known Petch-Hall effect is accounted via this relation. The formation and evolution of dislocation subcells is assumed to following the relation proposed by Holt where the evolution depends on the dislocation density. It has been added a restriction giving a lower limit for the subcell size, s_{∞} . The subcell size is written as

$$s = K_c \frac{1}{\sqrt{\rho_i}} + s_{\infty} \quad (6.10)$$

This measure does not need to be an actual dimension of a cell as many different patterns of LEDS can be formed. It is taken as an average measure of the effect of the LEDS on the mean free path rather than a geometric measure of LEDS. The density of mobile dislocations is via Orowan's equation related to the plastic strain rate. Therefore, the increase of the immobile dislocation density is assumed to be proportional to the plastic strain rate [69] according to

$$\dot{\rho}_i^{(+)} = \frac{m}{b} \frac{1}{\Lambda} \dot{\epsilon}^p \quad (6.11)$$

where m is the Taylor orientation factor and b is the magnitude of Burgers' vector.

6.2.2 Recovery

Recovery is as contrast to generation of dislocation an annihilation process of dislocations. A mobile dislocation may for example be annihilated by other mobile or immobile dislocation or through interaction with grain boundaries [70].

Vacancies have also an influence on the recovery process since they may diffuse towards dislocations where annihilation and/or remobilization of dislocations may occur by e.g. climb. However, different processes may contribute to the reduction in dislocation density. Bergström [69] formulated a relation where the remobilization of dislocations is proportional to the immobile dislocation density according to

$$\dot{\rho}_i^{(-)} = \Omega \rho_i \dot{\epsilon}^p \quad (6.12)$$

where Ω denotes a recovery function dependent on temperature and strain rate.

Diffusions of vacancies influence the recovery. Militzer et al [71] used following formulation, which also is similar to the formulation in [72], for recovery by climb

$$\dot{\rho} = 2D_v^* \frac{Gb^3}{kT} \rho^2 \quad (6.13)$$

where D_v^* denotes the effective diffusivity coefficient while the recovery process in [73] was formulated according to

$$\dot{\rho}_i^{(-)} = \Omega(\rho_i^2 - \rho_{eq}^2) \quad (6.14)$$

where ρ_{eq} is an equilibrium value towards the density goes to. Based on equation (6.14) the recovery equation by climb, used here, is written as

$$\dot{\rho}_i^{(-)} = 2c_\gamma D_v \frac{c_v}{c_v^{eq}} \frac{Gb^3}{kT} (\rho_i^2 - \rho_{eq}^2) \quad (6.15)$$

where c_v^{eq} is the thermal equilibrium vacancy concentration, c_v is the fraction of vacancies, D_v is the diffusivity and c_γ is a calibration parameter.

6.2.3 Generation and migration of vacancies

Vacancies are important in that sense it render changes of atoms in closed packed structure and by this way render diffusions and recovery of dislocations. Vacancy is considered to be the predominant mechanism for diffusions [19].

The equilibrium concentration of point defects as mono-vacancy at a certain temperature may be given by [74]

$$c_v^{eq} = e^{\frac{\Delta S_{vf}}{k}} e^{-\frac{Q_{vf}}{kT}} = c_{v0} e^{-\frac{Q_{vf}}{kT}} \quad (6.16)$$

where ΔS_{vf} and Q_{vf} is the increase in entropy during creation of a vacancy respective the activation energy for vacancy formation.

The self-diffusion coefficient can be written as [75]

$$D_v = a^2 \nu e^{\frac{\Delta S_{vm} + \Delta S_{vf}}{k}} e^{-\frac{Q_{vm} + Q_{vf}}{kT}} = D_{v0} e^{-\frac{Q_v}{kT}} \quad (6.17)$$

where a is the lattice constant, ν is the lattice vibration frequency, ΔS_{vm} is the increase in entropy due to motion of vacancy and Q_{vm} is the energy barrier for vacancy motion.

By the proposed model by Militzer et al. [71] the excess vacancy can be modeled based on a generation and annihilation component. Rewriting the equation where the subcell evolution is considered gives

$$\dot{c}_v^{ex} = \dot{c}_v - \dot{c}_v^{eq} = \left[\chi \frac{\sigma b}{Q_{vf}} + \zeta \frac{c_j}{4b^2} \right] \frac{\Omega_0}{b} \dot{\epsilon} - D_{vm} \left[\frac{1}{s^2} + \frac{1}{g^2} \right] (c_v - c_v^{eq}) \quad (6.18)$$

where D_{vm} is the vacancy migration, Ω_0 is the atomic volume, χ is amount of the mechanical work spent on vacancy generation and ζ is the neutralization effect by vacancy emitting and absorbing jogs with the following restrictions

$$\begin{cases} 0.5 - \zeta_0 c_j & \text{if } c_j \leq 0.5 / \zeta_0 \\ 0 & \text{if } c_j > 0.5 / \zeta_0 \end{cases} \quad (6.19)$$

Militzer et al. assumed $\chi = 0.1$ and $\zeta = 10$. The concentration of thermal jogs is given by

$$c_j = e^{-\frac{Q_f}{kT}} \quad (6.20)$$

where the energy for formation is approximately given by

$$Q_f = \frac{Gb^3}{4\pi(1-\nu)} \quad (6.21)$$

The vacancy migration is given by

$$D_{vm} = D_{vm0} e^{-\frac{Q_{vm}}{kT}} \quad (6.22)$$

The rate of change in equilibrium concentration is only due to change in temperature as

$$\dot{C}_v^{eq} = C_v^{eq} \left(\frac{Q_{vf}}{T^2} \right) \dot{T} \quad (6.23)$$

Chapter 7

Determination of mechanical properties at high strain rates

Evaluation of the mechanical behavior of metals and alloys are important and can be done by different methods and machines. Machines for mechanical testing have been available for a long time. Already in 1886 was the first commercially machine introduced [5]. The machines have since then gradually developed from pure mechanical machines to more advance electromechanical and servo hydraulic machines with advanced control system in order to meet the changing demands. Furthermore, sensors and software has also been developed. Today there exist several different methods with different range of applications and limitations.

Available techniques are summarized in Figure 7.1. Quasi-static testing and creep testing belongs to the category with isothermal conditions and where the inertia forces are negligible. Special servohydraulic machines, Split-Hopkinson techniques and light gas gun driven impact belongs to the group for testing at higher strain rates where inertia forces become more significant and where adiabatic conditions arise. The transition line regarding strain rate when the inertial forces are negligible or not are in the range of $0.1\text{--}5\text{ s}^{-1}$ in the literature [5, 6, 7, 22]. However, the inertia effects become more pronounced as the loading rate increases, increasing strain rates. The basic and important distinction between quasi-static testing and testing at high strain rates is the prominent inertial and wave propagation effects at the latter. The area where the inertial forces are important to consider is according to [7, 22] divided into intermediate strain rates, high strain rates and very high strain rates. Conventional testing with screw or servo hydraulic machines are mainly used for quasi-static tests in strain rates range $10^{-4}\text{--}1\text{ s}^{-1}$ [7] while the Taylor test, the Split Hopkinson Pressure Bar test (SHPB) and the expanding ring test are used for high strain rates where inertial forces needs to be accounted for. Machines for conventional testing are usually designed with a moving crosshead and an immobile load cell. How the load is applied to the crosshead differs but it is usually

applied through a hydraulic cylinder or screw. Irrespective of load-applying mechanism the speed and the force of the crosshead is limited due to different reasons. Designs for increased crosshead speeds make it more difficult to extract sufficient force. Servohydraulic machines equipped with adapted high-capacity valves can reach strain rates of 200 s^{-1} [5] or even strain rates up to 500 s^{-1} can be reached with special servohydraulic machines [7, 22]. Dynamic tensile test with strain rates up to 200 s^{-1} has successfully been performed with a new special developed dynamic servohydraulic machine [76]. Tests at these dynamic strain rates are difficult and challenging since the inertial and wave propagation effects become more prominent. The elastic stress wave propagates through the specimen, load cell and the frame with the effects that several phenomena as inhomogeneous and time dependent oscillations stress field in the specimen and time dependent oscillations in measured force can appear [76].

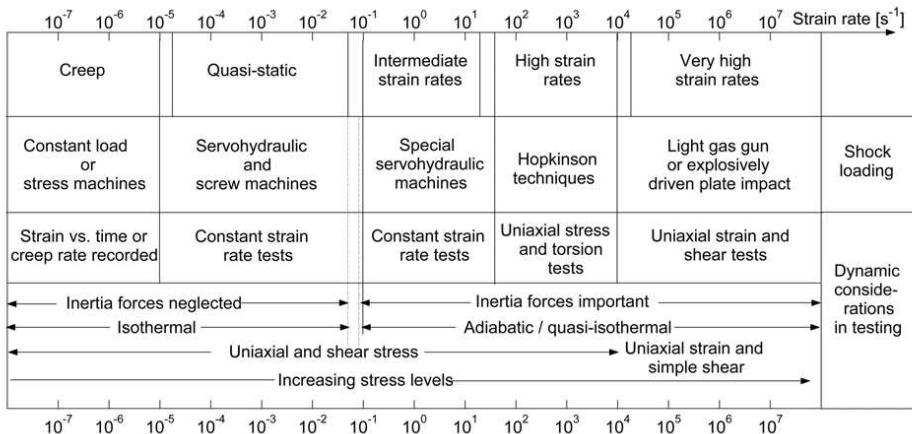


Figure 7.1 – Strain rate region, suitable testing technique and conditions for experiments, [5].

The SHPB method is of particular interest in the current work. Here follows a short history survey. The patent lawyer Bertram Hopkinson, eldest son of John Hopkinson studied dynamic strength of wires [77]. He decided to carry on this father work, which tragically had an accident in 1898 [78]. He extended the work to comprising projectile impact on elastic bars and presented a technique for measure the stress pulse in 1914 [77, 79]. The idea of placing a specimen between two bars and then impact it came much later. Hubert Kolsky was a man with a huge interest and a great influence in the research regarding characterization and quantitative measurements of material properties under sudden applied loads [80]. Shortly after the World War II, 1949 [79], he invented a test equipment based on the idea of compressing a specimen between two bars by introducing a propagating

compressive stress wave at one end. The test equipment is referred as the Kolsky bar but the far more common name is the Split-Hopkinson bars. Several variants have been developed during the years. Ulric Lindholm was one of them that improved the technique in the early 1960 [79] by modifying the length of the bars and the position of the strain gages. The far most common variant is the Split-Hopkinson Pressure Bars (SHPB) after the original design where a compression stress wave is introduced in the bars with the aim of deforming the test specimen. Based on the original idea Split-Hopkinson bars for tensile testing have been developed as well as torsional Split-Hopkinson bars with moving shear waves. Hardin et al (1969) seems to be the first to describe a design for tensile testing [77]. Tensile testing is often referred as Split-Hopkinson Tension Bars (SHTB). The idea is to transform a compression wave into a tensile wave with the aim of accomplish the deformation work. A similar design but with an increased rise time of the tensile stress wave was proposed by Nicholas (1981) [77]. Another approach where the tensile stress wave was introduced by pre-stressing part of the incident bar was announced by Albertini and Montagnani (1976) and Staab and Gilat (1991) [77]. The overall designs of the specimens are generally the same in the presented alternative above regarding tensile testing. Lindholm and Yeakley (1969] presented however a different design adapted for a compressive stress wave in the incident bar, a hat-formed specimen [77]. The current work includes material testing using SHPB and is described sections 7.3.

This section will briefly describe some of the available methods used for high strain testing.

7.1 Expanding ring test

Expanding ring test is a method for determine the tensile stress-strain relation at strain rates of $\sim 10^4 \text{ s}^{-1}$ or more. As the name implies the method is based on expanding a ring in its radial direction. Explosive or electromagnetic loading is placed in the centre of the ring and used to accelerate and expand the ring, see Figure 7.2. The hoop stress can be calculated by

$$\sigma = -R\rho \frac{d^2 R}{dt^2} \quad (7.1)$$

[5, 6] where R is the radius of the ring, ρ is the density and t is the time but it requires that the radial displacement is recorded. The wall thickness of the ring should be less than one-tenth of the diameter in order to evaluate the test correctly by this theory. High-speed cameras or laser interferometers can be used to record the deformation. Use of the latter technique makes it possible to measure the ring

velocity directly with the advantage that only one differentiation is necessary for calculating the stress and that improves the precision substantially [5].

The advantage of the method is the ability of generating stress-strain data at really high strain rates. However to continuously keep the strain rate has shown to be difficult. The strain rate is high at the beginning when the strain is small but as the strain increases the strain rate decreases. Another drawback of the methods is the radial compressive load which in certain cases may be so large that the yield limit of the material exceeds and affecting the stress-strain results [5]. The method is naturally limited to tensile strains.

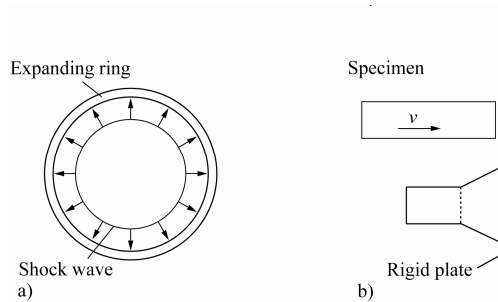


Figure 7.2 – a) Expanding ring test and b) classic Taylor test.

7.2 Taylor and rod impact tests

The Taylor test is a test method where a cylindrical specimen is accelerated and impacts a rigid plate. The specimen undergoes a plastic deformation that is not uniform, see Figure 7.2. During the impact with the stiff plate a highly deformed region starts to develop which Taylor depicted as elastic and plastic waves were introduced. The subsequent analysis is based on one-dimensional rigid-plastic analyses, propagation with different velocity and interaction of the generated waves forming a transition area like a truncated cone. By knowing the fractional change of the length of the specimen the dynamic yield strength could be determined.

The obtained deformation pattern of the rod after the impact does not always correspond to the simplified theory, especially for a high velocity impact. The deformed part in the front part shows a mushroom shape. Furthermore, the transition zone from the plastically deformed and the undeformed area may not be sharp and obvious [6]. However Wilkins and Guinan refined the analysis by including new boundary conditions and were able to predict the relation between

the deformed geometry and the plastic properties with better correspondence to experimental data [6]. Many of Taylors conclusions could then be confirmed [5].

Erlich *et al* developed the classical Taylor technique even further by introducing two major improvements which lead up to a better method for obtaining the stress-strain flow curve under high strain rate, 10^4 - 10^5 s⁻¹, loading [5]. The first improvements included an ultrahigh-speed camera for recording the deformation progress for comparison with two-dimensional computer simulations. The second improvement was to replace the rigid plate with a similar rod as the impacting rod, but stationary, and in this way eliminate the uncertainties regarding the boundary conditions. Then a symmetric impact was obtained and the method is simply designated as the symmetric rod impact test. The moving rod is accelerated with a gas gun by expanding helium. A variant of the symmetric rod impact test exist where a rigid plate is accelerated into the stationary rod. An advantage is that only the stationary rod is heated during elevated temperature tests in contrast to the symmetric rod test, where both rods need to be heated. This is referred as the asymmetric rod impact test.

7.3 Split-Hopkinson

Split-Hopkinson technique is a method based on longitudinal elastic stress wave propagations through bars where the stress wave has been produced by a mechanical impact. This technique has been used for dynamic testing in order to determine material properties at high strain rates. The results have thereafter been used for calibration of the material models in papers A, C and D. In case of a pressure bar for compression testing a compression stress wave is introduced while a tension stress wave has to be introduced for tensile testing. Varying designs of respectively type exist. Devices for tensile testing are more challenging [7], especially high temperature testing. A tensile stress wave must be introduced and the specimen must be tightening to the bars without significantly influence the stress wave and in a way which render tensile deformation. A schematic configuration for compression testing is shown in Figure 7.3.

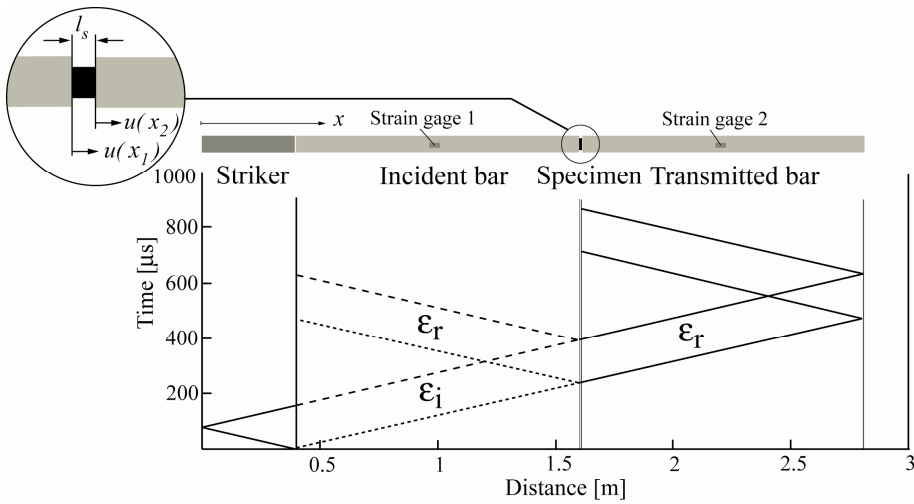


Figure 7.3 – Schematic sketch over a SHPB equipment showing wave propagation of the incident, reflected and transmitted waves.

It is basically composed of a striker, an incident bar, a transmitted bar and in some designs a third momentum trap bar. The latter is added to trap the reflected stress wave and prevent it to propagate back to interface between the specimen and the transmitted bar [7]. The design is rather unpretentious at first sight. No gripping device, moving cross heads or load cell etc. The specimen is placed and sandwiched between two long bars, the incident and the transmitted bar. A striker bar is accelerated to a certain velocity, impacting the incident rod and a compression stress wave is generated. Compressed air system is frequent used for accelerating the striker piston. The wave propagates through the incident bar towards the interface between the bar and the specimen, where the wave is partly reflected back while the remaining part is transmitted to the specimen and to the next interface for reflection and transmission to the transmitter bar. The propagating incident, reflected and the transmitted strain waves, are measured via strain gages on the incident and the transmitter bars. The strain can then be translated into stress by Hooke's law. Therefore and also for avoiding dispersion of the wave, these bars must behave elastic during the deformation. The distribution between reflected and transmitted energy depends on the acoustic impedance of the test specimen. In the case of ideal conditions, specimens of same material and diameter together with perfect alignment and contact conditions, then no reflections will appear at the interface between the different parts. The theory for evaluation of the measurements is given below.

7.3.1 Split Hopkinson - One dimensional wave equation

The displacement field in the bar is described by the well known one-dimensional wave equation,

$$\frac{\partial^2 u}{\partial x^2} = \frac{1}{c_0^2} \frac{\partial^2 u}{\partial t^2} \quad (7.2)$$

where x is the coordinate along the rod, u is the longitudinal displacement, t is time and c_0 is the wave propagation velocity [81]. The latter is defined as

$$c_0 = \sqrt{\frac{E}{\rho}} \quad (7.3)$$

where E is Young's modulus and ρ is the density. The solution of the wave equation is given by D'Alembert's solution according to

$$u(x, t) = f(x - c_0 t) + g(x + c_0 t) \quad (7.4)$$

where $f(x - c_0 t)$ and $g(x + c_0 t)$ correspond to a traveling wave in the increasing respective decreasing x -direction. Hence the longitudinal displacement at a certain coordinate along the bar is given by superposition of two waves. The strain and the particle velocity in the bar may be derived from the expression for the displacement according to

$$\varepsilon(x, t) = \frac{\partial u}{\partial x} = f'(x - c_0 t) + g'(x + c_0 t) \quad (7.5)$$

respectively

$$v(x, t) = \frac{\partial u}{\partial t} = c_0 [-f'(x - c_0 t) + g'(x + c_0 t)] \quad (7.6)$$

The stress state in the bar, under elastic conditions, may be given by

$$\sigma(x, t) = E[f'(x - c_0 t) + g'(x + c_0 t)] \quad (7.7)$$

Evaluation of the equations for the displacement and the stress under assumption of only one propagating wave gives that a negative particle velocity corresponds to a positive stress wave according to

$$\sigma(x, t) = -\frac{E}{c_0} v(x, t) \quad (7.8)$$

Recall that reflection of waves may occur at discontinuities for e.g. at instantaneous cross section changes as in the case of a SHPB. Thus the incident stress wave is reflected and transmitted at the transition between the incident bar and the test specimen and then one transmitted, moving in positive direction, and one reflected wave, moving in the negative direction, exist. A principled description of wave propagations in a transition is shown in Figure 7.4.

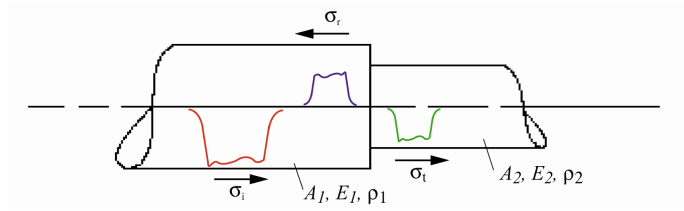


Figure 7.4 – Incident, reflected and transmitted waves at a transition.

Recall from equation (7.5) that the resulting strain field in a rod is based on two propagating waves in opposite direction. Hence the strain and the velocity in the incident rod at the left interface of the specimen, see Figure 7.3, is given by

$$\varepsilon(x_1, t) = \frac{\partial u}{\partial x} = f'(x_1 - c_0 t) + g'(x_1 + c_0 t) = \varepsilon_i + \varepsilon_r \quad (7.9)$$

respectively

$$v(x_1, t) = \frac{\partial u}{\partial t} = c_0 [-f'(x_1 - c_0 t) + g'(x_1 + c_0 t)] = c_0 (-\varepsilon_i + \varepsilon_r) \quad (7.10)$$

where index i and r denote incident and reflected wave.

Integrating equation (7.10) gives the displacement at x_1 according to

$$u(x_1, t) = c_0 \int_0^t (-\varepsilon_i + \varepsilon_r) d\tau \quad (7.11)$$

Applying the same procedure for the transmitted bar gives the following relations for the right interface of the specimen

$$v(x_2, t) = -c_0 \varepsilon_t \quad (7.12)$$

$$u(x_2, t) = -c_0 \int_0^t \varepsilon_t d\tau \quad (7.13)$$

where index t denote the transmitted wave. The strain, strain rate and stress in the deforming specimen are given by

$$\varepsilon_s = \frac{u(x_1, t) - u(x_2, t)}{l_s} = \frac{c_0}{l_s} \int_0^t (-\varepsilon_i + \varepsilon_r + \varepsilon_t) d\tau \quad (7.14)$$

$$\dot{\varepsilon}_s = \frac{c_0}{l_s} (-\dot{\varepsilon}_i + \dot{\varepsilon}_r + \dot{\varepsilon}_t) \quad (7.15)$$

$$\sigma_s = \frac{F(x_2, t)}{A_s} = \frac{E_0 A_0}{A_s} \varepsilon_t \quad (7.16)$$

where s is index for the specimen, l_s is length of specimen and A_s is area of the specimen. Introducing $-\varepsilon_i + \varepsilon_t = \varepsilon_r$ gives

$$\varepsilon_s = 2 \frac{c_0}{l_s} \int_0^t \varepsilon_r d\tau \quad (7.17)$$

$$\dot{\varepsilon}_s = 2 \frac{c_0}{l_s} \dot{\varepsilon}_r \quad (7.18)$$

Equation 7.14 or 7.17 and 7.16 are used to compute the strain and stress in the specimen based on the recorded strains. Examples of recorded strains are shown in Figure 7.5.

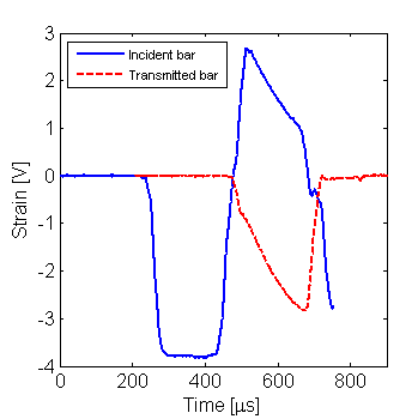


Figure 7.5 – Measured strain gages signal in the incident and transmitted bar.

7.3.2 Dispersion effects and corrections to the one-dimensional wave equation

The previous section showed the one-dimensional wave equation that is often used to evaluate SHPB. The created and propagating elastic stress wave from the impact of the striker and the incident slender bar would be expected to have a shape of a rectangular pulse of length $2L$ from this theory. In this case, L denotes the length of the striker. Strain gage measurements reveal however that a perfectly shaped rectangular pulse doesn't appear. The measured pulses do have a shape of a rectangular pulse but with significant oscillations, rounded corners and increased rise time. However the one-dimensional wave theory is based on more ideal conditions. For example the distortion and the lateral expansions and contradiction are neglected.

When the striker bar comes into contact with the incident bar the boundary conditions change rapidly. The atoms in the interface influence the atoms in the neighborhood and a compression stress wave starts to propagate in the incident bar and as well a tension wave in the striker bar. Due to the longitudinal strains and Poisson's ratio, lateral expansion and contraction occur as a result [6, 7, 22, 81, 82]. These lateral displacements influence the cross section and the stress distribution through the cross section. Radial constraint from the friction in the interface may also change the stress distribution. Also other types of elastic waves, e.g. spherical dilatational and surface waves, may be created due to the existing boundary conditions. The amplitude of the dilatational wave decreases however with the distance to such a degree that it vanishes after a length of 10 diameter of the bar [82]. Therefore, it is advantageous to place the strain gages at locations away from the ends. The generated surface waves trail behind the main wave caused by the impact and interacts continuously with it causing fluctuations in particle velocity, stress and strain and contribute to the oscillation in the measured pulse [6].

The created stress pulse is composed of a spectrum of frequencies [6, 7, 22, 82], where each frequency component travels at different velocity. It is known that low frequency components travel much faster than higher components. This results in retardation of the higher frequency components and a change of the propagating pulse during the propagation due to different velocities of the frequency components, i.e. dispersion occurs. The equation of motion for propagation of a sinusoidal wave in an infinitely long cylinder was independently solved by Pochhammer and Chree [82]. The solution is in the literature mentioned as the Pochhammer and Chree solution but may also be referred as the frequency or dispersion equation [82]. On basis on the theory from Pochhammer-Chree the ratio between the phase velocity c and the longitudinal wave velocity c_0 as function of the ratio between the bar diameter d_{bar} and pulse length Λ_{pulse} has been computed by

Bancroft respectively Davies [6, 22]. The results reveal that $c/c_0=1$ when the ratio d_{bar}/Λ_{pulse} coincides to 0, see Figure 7.6. But as the wavelength decreases the ratio c/c_0 decreases towards a plateau which coincides with Rayleigh waves. Thus higher frequencies leading to higher degree of dispersion effects. The ratio d_{bar}/Λ_{pulse} has also an influence on the displacement field through the cross section. The longitudinal displacement profile is flat when the ratio $\ll 1$ [82].

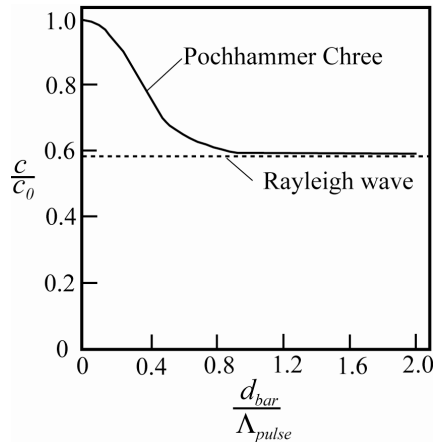


Figure 7.6 – Phase velocity as function of the ratio between the diameter of the bar and the wavelength.

The strains are usually measured some distance from the specimens for practical reasons. The pulse will change in shape as it travels due to the dispersion effect. Different methods are available for dispersion corrections e.g. the methods proposed by Bacon, Follansbee or Gorman [7]. Basically the dispersion correction requires that the measured pulse at position z_0 is transformed from time domain to the frequency domain by a Fast Fourier Transform, FFT. The correction for dispersion for each frequency component is done in the frequency domain by a suitable operation. The measured pulse is thereafter transformed back to the time domain with an inverse FFT. The dispersion correction performed in [82] lead to a smoother stress strain curve. The stress and strain within the specimen are directly related to the measured strains. If the dispersion corrections are not performed on the measured pulses the calculated stress-strain curves in the specimen may not reflect the true state. The curves may contain oscillations that are not representative. Dispersion correction should be used in connection of evaluating the measured pulses in SHPB [82].

7.3.3 Geometric constraints on dimensions of test specimen in SHPB

The evaluation of the stress, strain and strain rate in the specimen in the SHPB method according to the one-dimensional theory described in section 7.3.1 assumes a homogenous uniaxial stress state in the test specimen. This also implies that it static equilibrium exists in the specimen. However the action from a force is not momentary transmitted to the rest of the body with the result that stress equilibrium is not immediately achieved. Stress waves propagate with finite velocities. But force equilibrium is usually obtained after the reflected wave has travel forth and back in the specimen some times. A short specimen compared to the wave length of the impact wave is a condition for assuming force equilibrium in the test piece. However, the friction in the interface between the bars and specimen and the inertia effect are besides the geometry other influencing factors.

The geometry of the specimen is important for reliable data in compression as well as tensile testing. If the specimen is to slim, high l_s/d_s ratio, buckling arise easily in compression testing. Shearing, double barreling, barreling and rapid localized expansion due to work softening are other deformation modes that can appear [5]. Eccentric loading from e.g. non parallel end or die surfaces will leads to shearing. When the specimen is compressed it will expand but the friction in the interface will prevent the lateral flow at the loading surface. The material in midplane is not constrained, it expands and a barreling shape occurs. Severe barreling will occur if the frictional forces are too large. This causes an undesired multiaxial stress state in the specimen [22, 83]. The assumption of uniaxial homogenous stress states do not longer correspond to the actual stress state. Therefore the friction should be minimized since frictionless conditions lead to uniform radial and circumferential expansion with a homogenous stress state in the direction of the compression. Eliminating the friction and selection of a suitable l_s/d_s ratio are essential measure for homogeny uniaxial stress state. Friction can be minimized by appropriate lubricants. The film is however squeezed out when the force is high and metal to metal contact appears. Several designs have been utilized trying to maintain the film in the interface e.g. concentric circular groves and a pocket [5]. l_s/d_s ratios less than 2.0 are often mentioned for reliable results and avoidance of buckling and shearing. When it comes to minimizing the friction errors the l_s/d_s ratio should according to ASTM E9 [5] be within the interval $1.5 < l_s/d_s < 2.0$. The optimum ratio for SHPB test is however one-half of the most favorable ratio for test at low strain rates. Malinowski and Klepaczko found that the optimum ratio could be found from

$$\left(\frac{l_s}{d_s}\right)_{opt} = \left[\frac{2\mu\sigma_z}{\rho_s d_s^2 (\dot{\epsilon}^2 + \ddot{\epsilon})}\right]^{1/3} \quad (7.19)$$

where σ_z is the measured stress, ρ_s the density of the specimen, μ friction coefficient [22]. High strength aluminum alloys and titanium should have a ratio of 1-1.5 while copper, nickel and aluminum should have a ratio of 0.5 to 1. Material with low strength should have a ratio less than 0.5.

The initial response of the specimen affects the stress results. A study by Bertholf and Karnes regarding inertia and friction effects in SHPB tests showed that the inertia effects become more severe at high strain rates appearing as increasing oscillations in the measured stress-strain curve [22]. These oscillations can be reduced by increasing the rise time of the incident pulse [22, 84]. A pulse shaping material is usually placed between the striker and the incident bar in order to increase the rise time. Davies and Hunter also studied the inertia effects [22]. Following equation was presented taking the inertia effects into account

$$\sigma(t) = \sigma_m(t) + \rho_s \cdot \left(\frac{l_s^2}{6} - \nu_s \cdot \frac{d_s^2}{8} \right) \cdot \frac{\partial^2 \epsilon(t)}{\partial t^2} \quad (7.20)$$

where σ_m is the measured stress, ρ_s the density, ν the Poisson's ratio, l_s the length, d_s the diameter of the specimen [5, 22]. The first term in bracket represent the correction for radial inertia effects while the second term accounts for the longitudinal inertia effects. Equation (7.20) shows that the inertia effects cancel out when the strain rate is constant or when the terms in bracket are zero. The latter gives the relation

$$\frac{l_s}{d_s} = \sqrt{\frac{3 \cdot \nu_s}{4}} \quad (7.21)$$

which for $\nu_s=0.3$ results in a ratio of $l_s/d_s=0.47$ for minimum inertia effects. Warren and Forrestal [84] have recently study the radial inertia effects for incompressible specimen. They found out that radial inertia effects can be neglected for steel specimens provided that dynamic force equilibrium is fulfilled. Radial inertia effects can however be important in soft materials.

Chapter 8

Stainless steels

Stainless steels are steels with a chemical composition forming a protecting layer on the surface. The main alloying elements in stainless steels are chromium and nickel. Nickel is an austenitic stabilizer while chromium is a ferrite stabilizer. The chromium content in stainless steels should be at least 10.5% and the maximum contents of carbon should be 1.2% [85]. By high contents of chromium, >11%, a thin passive chromium oxide layer is formed on the surface under oxidizing condition improving the corrosion resistance. The layer is self healed when damaged. Nickel and molybdenum are other alloying elements contributing to enhanced corrosion resistance. The latter has the properties of decreasing the required oxidizing environment to form a passive protected layer and increasing the resistance to chloride induced pitting [29]. Carbon is an alloying element that strongly contributes to the strength and which has the devastating property of forming chromium carbides. The carbon contents vary from really low values to high values depending on type of steel.

However, stainless steels may be subdivided into ferritic, martensitic, austenitic, austenitic-ferritic (duplex) and precipitation hardening steels after their microstructure [29, 86]. It is well known that the alloying elements and the quantity influence the microstructure. A convenient way to estimate the effects of various alloying elements and their quantity on the microstructure is by a Schaeffler-diagram where the ferritic and austenitic forming effects are calculated by chromium respectively a nickel equivalent. The diagram was originally designated for prediction of the microstructure after welding [87]. Several equations exist in the literature for estimation of chromium and nickel equivalent. One example, from [88], is

$$\begin{aligned}Cr_{equivalent} &= Cr + 2Si + 1.5Mo + 5V + 5.5Al + 1.75Nb + 1.5Ti + 0.75W \\ Ni_{equivalent} &= Ni + Co + 0.5Mn + 0.3Cu + 25N + 30C\end{aligned}\quad (8.1)$$

where the individual concentrations are in weight percentage. As can be seen nitrogen and carbon are the greatest austenite stabilizing alloying elements and have a great influence on the nickel equivalent. Carbon and nitrogen have also a strong effect on the strength [29, 30, 86] by interstitially solution. Nitrogen has also the characteristics of forming Cr_2N and thereby reduces the depletion of chromium in the grain boundaries by reducing the precipitation of Cr_{23}C_6 . The intergranular corrosion (IGC) is somewhat reduced. Nickel on the other hand increases the susceptibility to intergranular corrosion [30]. A chromium-depleted zone increases the susceptible of stress corrosion cracking (SCC) and austenitic steels are known to be susceptible to SCC by intergranular stress corrosion cracking (IGSCC) and transgranular cracking (TGSCC) [30]. Figure 8.1 shows the effect of various alloying elements.

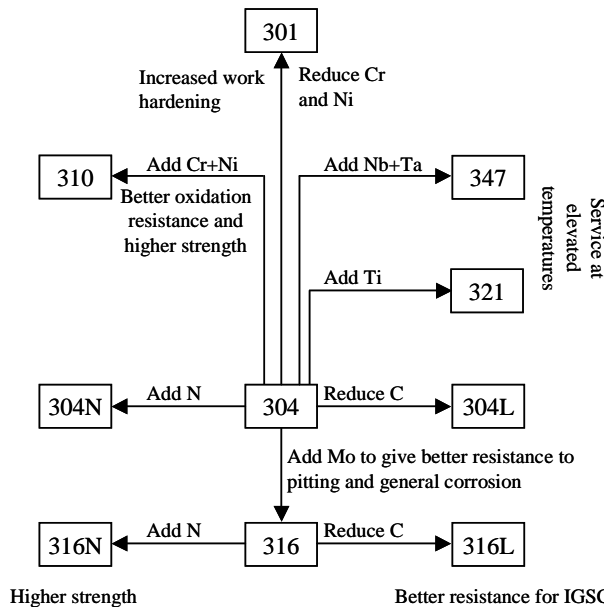


Figure 8.1 – Flow diagram of steels and alloying elements impact.

8.1 Ferritic stainless steels

Ferritic stainless steels have a ferritic microstructure made up by a BCC-structure, are magnetic and have a rather high brittle-fracture transition temperature which strongly depends on the level of carbon and nitrogen. These alloys are somewhat less ductile than the austenitic steels and are not hardenable by heat treatments.

8.2 Martensitic stainless steels

Martensite is magnetic and has a high strength and may be formed during cooling or cold working. Martensitic steels have traditionally high carbon contents ranging from 0.08 to 1% and may be hardened and tempered. In case of high contents of ferrite in the microstructure the steels are called martensitic-ferritic. The weldability decreases with increasing carbon contents. However, steels with a martensitic and austenitic microstructure exist where the carbon content is maximum 0.06% [86]. Steels with this two-phase microstructure are usually called martensitic-austenitic stainless steels. Martensitic steels with really low carbon, maximum 0.030%, contents have been developed for high strength and good impact strength and weldability.

8.3 Austenitic-ferritic stainless steels

Austenitic-ferritic steels have a two-phase microstructure and are commonly called duplex. The apportionments of the individual phases are generally 30-50 % ferrite and the rest is austenite [86]. All modern duplex steels have low carbon contents and the contents of nickel are low.

8.4 Precipitation hardening stainless steels

The characteristic of these steels are the precipitation of intermetallic compounds, carbides, nitrides or copper phases [86]. May be hardened by heat treatments.

8.5 Austenitic stainless steels

Austenitic steels have an fcc-structure and have generally an excellent combination of corrosion resistance, ductility, toughness and weldability [31]. However, the austenitic structure has the ability to transform into martensite during cooling and/or plastic deformation. The stability of the austenitic structure depends on the chemical composition. Carbon and nitrogen are alloying elements that strongly promote an austenitic structure. Austenitic stainless steels that may transform into martensite during cooling and/or plastic deformation are called metastable austenitic steels.

Chapter 9

Distribution of works and summary of results in appended papers

This thesis consists of four papers, all in co-operation with other researchers. The author of this thesis had the main responsibility for planning, performing and evaluation of the experimental work including cutting force measurements, quick-stop measurements, microstructural examinations and high strain testing via SHPB. The calibration was done in co-operation with Professor Lars-Erik Lindgren. The author has taking part of writing in all articles and has also participated in the simulations and evaluations. Article A and B were planned by Professor Lars-Erik Lindgren who also was the main responsible for writing. Article C was planned together with PhD Vahid Kalhori who also was the main responsibly for the simulations and the writing. Article D was planned in collaboration with co-authors, PhD Ales Svoboda was the main responsible for the simulations and the writing. A summary of the appended papers are given blow.

9.1 Paper A

Material modelling and physical based models with particular emphasis on high strain rates

Lars-Erik Lindgren, Dan Wedberg

Machining is a manufacturing process where the material undergoes severe deformation with large strains, high strain rates and high locally temperatures. Simulation of metal cutting is hence challenging from both a numerical and physical perspective. This makes the description of the material behavior important. Different material models exist. This paper compares the empirical Johnson-Cook model with a physical material model for the plastic behavior of the stainless steel AISI 316L. Calibration of test data was conducted using a minimization algorithm.

First was the models calibrated for low strain rates between 0.001 to 10 s^{-1} and temperatures from room temperature up to $1300\text{ }^{\circ}\text{C}$. The dislocation density model showed a good agreement for strain rates between 0.001 to 10 s^{-1} and temperatures between room temperature and $1300\text{ }^{\circ}\text{C}$. The Johnson-Cook model did not show the same consistency throughout the area. Then the models were tested how well they managed to represent the material behavior at high strain rates (1000 to 9000 s^{-1}) and temperatures up to $950\text{ }^{\circ}\text{C}$. None of the models managed to predict the material behavior especially good at these strain rates. The discrepancy indicates that new deformation mechanisms occur at these high strain rates. Thus the physical based model must be extended with these mechanisms. However, the Johnson-Cook model can only be used for a limited test set of high strain rates.

9.2 Paper B

Verification and validation of machining simulations for sufficient accuracy

Lars-Erik Lindgren, Dan Wedberg, Ales Svoboda

Simulation of metal cutting is known to be challenging in terms of numerics and physics. Any created model is supposed to reflect the real world phenomenon of interest with certain accuracy within the scope of the model. With these expectations, verification and validation are essential for a complex process such as machining. Validation means checking of the accuracy of the model with respect to the real world behavior. In the case of machining validation it is usually done by studying the chip morphology from quick stop test, measurements of cutting forces and/or residuals stresses and comparing with simulated results. Validation with respect to measured cutting forces is the most common and straightforward methods but far from trivial without difficulties. For example, variations in material properties of the workpiece materials and the cutting edge radius of the cutting tools cause variations in the measured forces for nominally the same cutting case. An agreement between simulated and measured cutting forces within 10% must therefore be deemed as good considering the common variations in real machining applications.

9.3 Paper C

Simulation of mechanical cutting using a physical based material model

Vahid Kalhori, Dan Wedberg, Lars-Erik Lindgren

In this paper a physical based material model of the stainless steel SANMAC 316L, calibrated with data from high strain rates testing, is implemented in the explicit formulated finite element program AdvantEdge in order to predict the cutting forces and the chip morphology. Both an isotropic and a mixed isotropic-kinematic hardening rule were tested. Interface properties for the interface between the tool and the chip are uncertain. The interface is usually divided into a sticking and a slipping region. It was however not possible to define local friction coefficients in AdvantEdge. A sensitivity study of the friction coefficient was therefore performed. It turned out that there was no significant difference in force level for friction coefficients above 0.6. A value of 0.6 was therefore chosen. The predicted results were then compared with experimental measured results of cutting forces and chip morphology. The latter through comparison of shear plane angle and the ratio between cut and uncut chip thickness. The mixed isotropic-kinematic hardening model gave a better prediction of the feed forces. The predicted cutting forces correspond well with the measured except for the feed force at a cutting speed of 100 m/min where the simulated feed force was 30 % lower. This deviation is believed to be due BUE. The same good agreement was not obtained regarding chip thickness ratio. One possible explanation of this may be that thermal softening is not sufficient to describe the chip formation adequately. A segmented chip form was however obtained.

9.4 Paper D

Simulation of mechanical cutting using a physically based plasticity model

Ales Svoboda, Dan Wedberg, Lars-Erik Lindgren

Simulation of metal cutting is both demanding and challenging, and particular requires a good material model. A physically based dislocation density model (DD) and an empirical Johnson & Cook plasticity model (JC) are both used in this paper to simulate orthogonal cutting of SANMAC 316L using an implicit finite element code. The later is one of the most commonly used material models for simulations of metal cutting. A sensitivity study was performed in order to examine the heat transfer contact coefficient. A value of 5×10^6 (W/m²°C) showed to be realistic and subsequently used. A Coulomb friction model with a friction coefficient of $\mu = 0.5$, estimated as an average value from the whole range of cutting experiments, was

used. The results from the simulations with the two models were compared with measured cutting forces and chip morphology. Quick-stop tests were evaluated with respect to shear plane angle and chip thickness. The predicted feed force was underestimated by the DD model of about 10 (%) compared to 15 (%) by the JC model. Largest deviation in prediction for the JC model was 20 (%) and 16 (%) for the DD model. The cutting forces were slightly better predicted by the DD model. The DD model also predicted the shear plane angle and chip thickness better.

Chapter 10

Conclusions

The results in the papers this thesis consists of are based on experimental measurements used to calibrate and validate the material model. Furthermore, measurements and simulations of machining were performed where the material model is an important part. Some microstructural examinations were also carried out to investigate the potential mechanisms associated with material behavior, hardening. Examination of magnetic phase and some TEM studies were performed. Conclusions follow below.

The performed high strain rate tests have shown that the flow stress for AISI 316L increases with the strain rate and hence confirms a strain rate sensitive behavior. The original calibration of the DD model at low strain rates ($\leq 10 \text{ s}^{-1}$) by earlier work by Lindgren *et al.* [89] was not able to capture the material behavior at high strain rates with good correspondence. This discrepancy in reproducing the material behavior at high strain rates indicates that new deformation mechanisms occur at these high strain rates. A re-calibration of the DD model where the obstacle strength parameters τ_0 and Δf_0 were assumed to be temperature dependent resulted in a better response with reasonably acceptable accuracy. The results are presented in Figure 10.1. This would imply that different obstacles dominate at different temperatures. This is probably not the case. More likely is that the mechanisms discussed in section 4 occur.

Calibration of the empirical JC model showed that it could not reproduce the entire test data at low strain rates as the DD-model. It was not able to model the response in the high strain rate range when extrapolated. It is therefore still believed that physically based models have a greater potential than empirical models to cover wider range of strains, strain rates and temperatures. It is well known that austenitic stainless steel has a tendency of formation of α' -martensite during deformation which may enhance the work hardening. Experimental measurements of the

magnetic phase via magnetic balance were therefore performed. An insignificant increase could only be observed with increasing strain and strain rate. The proportion of magnetic phase was even lower than what was found in [89] for tests at lower strain rates at room temperature. AISI 316L may therefore be regarded as a stable austenitic steel and the above observation may not be explained with formation of α' -martensite. Therefore, most likely is that the cell formation is strain rate dependent and/or that drag forces are significant.

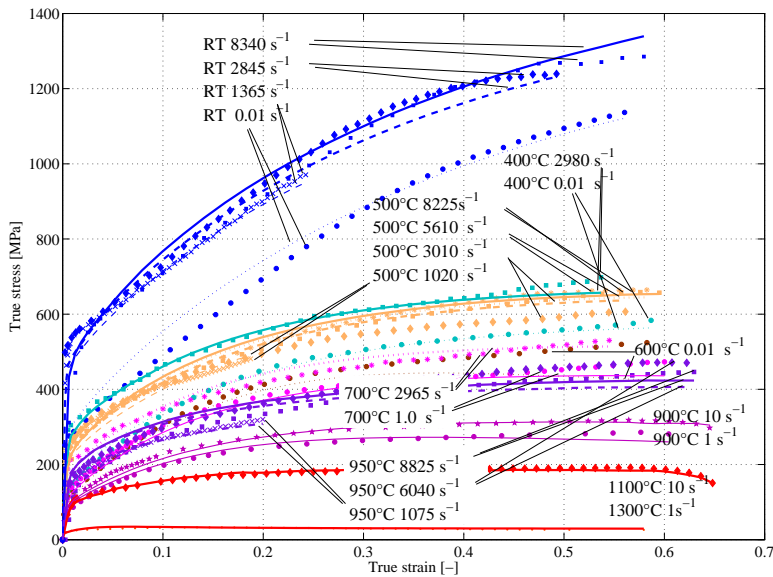


Figure 10.1 – Flow stress curves used for re-calibrated the DD model including high strain rate tests. The lines are computed values.

Validations are important and require robust experimental methods as well as simulations. Obtaining converged results from simulations with respect to the element size as well as time stepping can sometimes be difficult. It can though be concluded that using mesh and convergence criteria that capture local effects are important for the accuracy. Furthermore, it will affect the validation process. Variation in work piece material properties as well as geometric variations from e.g. production of cutting tools influences the validation process. The requirements to consider a model to be validated must therefore also consider the process of variation within the industry. A deviation between the predicted and the measured cutting forces of around 10% are in this respect quite good.

Empirical materials models are commonly used for description of material behavior in commercial FE codes. This work shows that physically based plasticity models can be implemented into FE-codes for simulation of orthogonal cutting. A deviation in cutting forces of less than 8% could be observed when using an updated Lagrangian formulation and an explicit time integration scheme in combination with a DD-model. The same conformance was not obtained regarding the chip shape. The time stepping procedure in combination with the mesh refinement seems though be able to capture the chip segmentation quite well without considering damage evolution.

Chapter 11

Future work

The cutting model using the DD constitutive model gave an error within 10% validation limit for cutting forces but the error for chip geometry is larger. It is believed that this could be improved as it has been found that the DD model is lacking the correct high strain rate deformation mechanism. Despite the agreement between the recalibrated DD model and SHPB data, Figure 10.1, this is needed as the strain rate in the cutting process goes up to 70000 s^{-1} . Therefore, future work will be to

- a) improve the physical based dislocation density model by adding relevant physics for high strain rates. The current hypothesis is that drag forces and/or effect of strain rate on formation of low energy dislocation structures are needed. The model will then need to be recalibrated.
- b) further validation of this new model for machining simulations.
- c) evaluating robustness of process by including statistical information on variation of material properties.

12 References

- [1] Hull D., D. J. Bacon, *Introduction to dislocations*. Butterworth-Heinemann, 2001.
- [2] Stouffer D. C., L. T. Dame, *Inelastic deformation of metals: models, mechanical properties and metallurgy*. John Wiley & Sons, Inc, 1996.
- [3] Regazzoni G., U. F. Kocks, P. S. Follansbee, *Dislocation kinetics at high strain rates*. Acta Metall. 35 (1987): 2865-2875.
- [4] Lee W. S., C-F. Lin, T- J. Liu, *Strain rate dependence of impact properties of sintered 316L stainless steel*. Journal of Nuclear Materials 359 (2006) 247-257.
- [5] ASM handbook, *Mechanical testing and evaluation*, volume 8. Materials Park Ohio, 2000.
- [6] Meyers M. A., *Dynamic behavior of materials*. John Wiley & Sons, Inc, 1994.
- [7] Hokka M., *Effects of strain rate and temperature on the mechanical behavior of advanced high strength steels*. PhD thesis, Tampere University of Technology, Tampere, 2008.
- [8] Boothroyd G., W. A. Winston, *Fundamentals of Machining and Machine Tools*, third edition. CRC Press, Taylor & Francis Group, 2006.
- [9] Moore D. F., *Principles and application of tribology*. A. Wheaton Co., Exeter, 1975.
- [10] Kalhori V., *Modelling and Simulation of Mechanical Cutting*. PhD thesis, Department of Mechanical Engineering, Luleå University of Technology, Luleå, 2001.
- [11] Vaz Jr. M., D. R. J Owen, V. Kalhori, M. Lundblad, L-E. Lindgren, *Modelling and simulation of machining processes*. Arch. Comput. Methods Eng. (2007) 14: 173-204.
- [12] Saoubi R. M., J. C. Outeiro, B. Changeux, J. L. Lebrun, A. M. Dias, *Residual stress analysis in orthogonal machining of standard and resulfurized AISI 316L steels*. Journal of Materials Processing Technology 96 (1999): 225-233.
- [13] Trent E.M., *Metal Cutting*, third edition. Butterworth Heinemann Ltd, 1991.
- [14] Balaji A. K., G. Sreeram, I. S. Jawahir, E. Lenz, *The effects of cutting tool thermal conductivity on tool-chip contact length and cyclic chip formation in machining with grooved tools*. Annals of the CIRP 48 (1999): 33-38.
- [15] Fang N., I. S. Jawahir, P. L. B. Oxley, *A universal slip-line model with non-unique solutions for machining with curled chip formation and a restricted contact tool*. International Journal of Mechanical Sciences 43 (2001): 557-580.

- [16] Shaw C. M., *Metal Cutting Principles*. Oxford Science Publications, 1997.
- [17] Chern G-L., *Development of a new and simple quick-stop device for study on chip formation*. International Journal of Machine Tools & Manufacture 45 (2005): 789-794.
- [18] Lubliner J., *Plasticity theory*. Dover Publications, 2008.
- [19] Jastrzebski Z. D., *The nature and properties of engineering materials*, third edition. John Wiley & Sons, Inc, 1987.
- [20] Meyers M.A *et al.* *Constitutive description of dynamic deformation: physically-based mechanism*. Materials Science and Engineering A322 (2002): 194-216.
- [21] Janecek M., K. Tangri, *The influence of temperature and grain size on substructure evolution in stainless steel 316L*. Journal of Materials Science, 30 (1995): 3820-3826.
- [22] Vuoristo T., *Effect of strain rate on the deformation behavior of dual phase steels and particle reinforced polymer composites*. PhD thesis, Tampere University of Technology, Tampere, 2004.
- [23] Dieter G. E., *Mechanical Metallurgy*. McGraw-Hill Book Company (UK) Limited, 1988.
- [24] Humphreys F. J., M. Hatherly, *Recrystallization and related annealing phenomena*, second edition. Elsevier Ltd, 2004.
- [25] Babu B., *Physical Based Model for Plasticity and Creep of Ti-6Al-4V*. Licentiate thesis, Department of Applied Physics and Mechanical Engineering, Luleå University of Technology, Luleå, 2008.
- [26] Raman S. G. S., K. A. Padmanabhan, *Tensile deformation-induced martensitic transformation in AISI 304LN austenitic stainless steel*. Journal of Materials Science Letters 13 (1994): 389-392.
- [27] Talonen J., H. Hänninen, *Formation of shear bands and strain-induced martensite during plastic deformation of metastable austenitic stainless steels*. Acta Materialia 55 (2007): 6108-6118.
- [28] Garion C., B. Skoczko, S. Sgobba, *Constitutive modelling and identification of parameters of the plastic strain-induced martensitic transformation in 316L stainless steel at cryogenic temperatures*. International Journal of Plasticity 22 (2006): 1234-1264.
- [29] Hedström P., *Deformation induced martensitic transformation of metastable stainless AISI 310*. Licentiate thesis, Department of Applied Physics and Mechanical Engineering Luleå University of Technology, Luleå, 2005.
- [30] Marshall P., *Austenitic stainless steels - Microstructure and mechanical properties*. Elsevier applied science publishers LTD, 1984.

- [31] Totten E., G., *Steel heat treatment handbook -Steel heat treatment: metallurgy and technologies*, second edition. CRC Press, Taylor & Francis Group, 2007.
- [32] Varma S.K., J. Kalyanam, L.E. Murr, V. Srinivas, *Effect of grain size on deformation-induced martensite formation in 304 and 316 stainless steels during room temperature tensile testing*. Journal of Materials Science Letters 13 (1994): 107-111.
- [33] Talonen J., P. Nenonen, G. Pape, H. Hänninen, *Effect of strain rate on the strain-induced $\gamma \rightarrow \alpha'$ -martensite transformation and mechanical properties of austenitic stainless steels*. Metallurgical and Materials Transactions A 36A (2005):421-432.
- [34] Murr L. E., E. V. Esquivel, *Review observations of common microstructural issues associated with dynamic deformation phenomena: twins, microbands, grain size effects, shear bands, and dynamic recrystallization*. Jour. of Mat. Science 39 (2004): 1153-1168.
- [35] Prinz F., A. S. Argon, W. C. Moffatt, *Recovery of dislocation structures in plastically deformed copper and nickel single crystals*. Acta Metall. 30 (1982): 821-830.
- [36] Porter D. A., K. E. Easterling, *Phase transformations in metals and alloys*, second edition. CRC Press, 1992.
- [37] Holt D. L., *Dislocation cell formation in metals*. Journal of Applied Physics 41 (1970): 3197-3201.
- [38] Kuhlman-Wilsdorf D., *Q: Dislocation structures – how far from equilibrium? A: Very close indeed*. Materials Science and Engineering A315 (2001): 211-216.
- [39] Michel D. J., J. Moteff, A. J. Lovell, *Substructure of type 316 stainless steel deformed in slow tension at temperatures between 21 ° and 816 °*. Acta Metallurgica 21 (1973) 1269-1277.
- [40] Shume A. J., Y. J. Chang, M. N. Bassim, *A study of the effect of initial grain size and strain rate on dislocation structures in copper*. Materials Science and Engineering A108 (1989): 241-245.
- [41] Thiagarajan S., S. K. Varma, *Effect of strain rate on dislocation cell size in oxygen-free high-conductivity copper during a tensile test*. Journal of Materials Science Letters 11 (1992): 692-694.
- [42] Sil D., S. K. Varma, *The combined effect of grain size and strain rate on the dislocation substructures and mechanical properties in pure aluminum*. Metallurgical Transaction A 24 (1993), 1153-1161.
- [43] Rao J. G., S. K. Varma, *The effect of grain size and strain rate on the substructures and mechanical properties in nickel 200*. Metallurgical Transaction A 24 (1993), 2559-2568.

- [44] Shankaranarayan H., S. K. Varma, *Strain-rate and grain-size effects on substructures and mechanical properties in OFHC copper during tension*. Journal of Materials Science 30 (1995): 3576-3586.
- [45] Lee W. S., H. F. Lam, *Mechanical response and dislocation substructure of high strength Ni-Cr-Mo steel subjected to impact loading*. Journal de Physique III 4 (1994): 307-312.
- [46] Cheval F., L. Priester, *Effect of strain rate on the dislocation substructure in deformed copper polycrystals*. Scripta Metallurgica 23 (1989): 1871-1876.
- [47] Lee W-S., C-F. Lin, *Impact properties and microstructure evolution of 304L stainless steel*. Materials Science and Engineering A308 (2001): 125-135.
- [48] Follansbee P. S., *High-strain-rate deformation of FCC metals and alloys*, Metallurgical applications of chock-wave and high-strain-rate phenomena, konf.
- [49] Lesuer D. R., G. J. Kay, M. M. LeBlanc, *Modeling large strain, high rate deformation in metals*. Third Biennial Tri-Laboratory Engineering Conference Modeling and Simulation, Pleasanton, 1999.
- [50] Nemat-Nasser S., W-G. Guo, D. P. Kihl, *Thermomechanical response of Al-6XN stainless steel over a wide range of strain rates and temperatures*. Journal of the Mechanics and Physics of Solids 49 (2001): 1823-1846.
- [51] Guo W-G., S. Nemat-Nasser, *Flow stress of Nitronic-50 stainless steel over a wide range of strain rates and temperatures*. Mechanics of Materials 38 (2006): 1090-1103.
- [52] Kumar A., F. E. Hauser, J. E. Dorn, *Viscous drag on dislocations in aluminum at high strain rates*. Acta Metallurgica 16 (1968) 1189-1197.
- [53] Frost H. J., M. F. Ashby, *Deformation mechanism maps – The plasticity and creep of metals and ceramics*. Pergamon Press, 1982.
- [54] Galligan J.M., T. J. McKrell, M. T. Robson, *Dislocation drag processes*. Materials Science and Engineering A287 (2000): 259-264.
- [55] Follansbee P. S., U. F. Kocks, *A constitutive description of the deformation of copper based on the use of the mechanical threshold stress as an internal state variable*. Acta Metall. 36 (1988): 81-93.
- [56] Zerilli F. J., R. W. Armstrong, *The effect of dislocation drag on the stress-strain behavior of F.C.C. metals*. Acta Metall. Mater. 40 (1992): 1803-1808.
- [57] Bowen A. W., P. G. Partridge, *Limitations of the Hollomon strain-hardening equation*. J. Phys. D: Appl. Phys 7 (1974): 969-978.
- [58] Soussan A., S. Degallaix, T. Magnin, *Work-hardening behavior of nitrogen-alloyed austenitic stainless steels*. Materials Science and Engineering A142 (1991): 169-176.

- [59] Hua-bing L., J. Zhou-hua, Z. Zu-rui, X. Bao-yu, L. Fu-bin, *Mechanical properties of nickel free high nitrogen austenitic stainless steels*. Proc. of Sino-Swedish Structural Materials Symposium (2007): 330-334.
- [60] Bergström Y., H. Hallén, *An improved dislocation model for the stress-strain behavior of polycrystalline α -Fe*. Materials Science and Engineering 55 (1982): 49-61.
- [61] Johnson G. R., W. H. Cook, *A constitutive model and data for metals subjected to large strains, high strain rates and high temperatures*. Seventh International Symposium on Ballistics, The Hague, The Netherlands, 1983.
- [62] Umbrello D., R. M'Saoubi, J.C. Outerio, *The influence of Johnson-Cook material constants on finite element simulation of machining of AISI 316L steel*. International Journal of Machine Tools & Manufacture 47 (2007): 462-470.
- [63] Rule W. K., S. E. Jones, *A revised form for the Johnson-Cook strength model*. International Journal of Impact Engineering 21 (1998): 609-624.
- [64] Holmquist T. J., G. R. Johnson, *Determination of constants and comparison of results for various constitutive models*. Journal de Physique IV 1 (1991): 853-860.
- [65] Huang Y., S. Y. Liang, *Cutting forces modeling considering the effect of tool thermal property-application to CBN hard turning*. International Journal of Machine Tools & Manufacture 43 (2003): 307-315.
- [66] Zerilli F. J., R. W. Armstrong, *Dislocation-mechanics-based constitutive relations for material dynamics calculations*. J. Appl. Phys. 61 (1987) 1816-1825.
- [67] Kocks U. F., A. S. Argon, M. F. Ashby, *Thermodynamics and Kinetics of slip*. Progress in Material Science 19, Pergamon Press, 1975.
- [68] Cheng, J. Nemat-Nasser, S., Guo W., *A unified constitutive model for strain-rate and temperature dependent behavior of molybdenum*. Mechanisms of Materials 33 (2001): 603-616.
- [69] Bergström Y., *The plastic deformation of metals – a dislocation model and its applicability*. Reviews on powder metallurgy and physical ceramics (1983): 79-265.
- [70] Bergström Y., *A dislocation model for the stress-strain behaviour of polycrystalline α -Fe with special emphasis on the variation of the densities of mobile and immobile dislocations*. Materials Science and Engineering 5 (1969/70): 193-200.
- [71] Militzer M., W. P. Sun, J. J. Jonas, *Modelling the effect of deformation-induced vacancies on segregation and precipitation*. Acta Metallurgica et Materialia 42 (1994): 133-141.

- [72] Siwecki, T., G. Engberg, *Recrystallisation controlled rolling of steels*. In: Hutchinson, B. et al. (Eds.), *Thermo-Mechanical Processing in Theory, Modelling & Practise [TMP]2*. The Swedish Society for Materials Technology, Stockholm, Sweden, 122-144.
- [73] Li, J., *Recrystallisation, Grain Growth and Texture*. 1966: ASM.
- [74] Haasen P., *Physical Metallurgy*, third edition. Cambridge University Press, 1996.
- [75] Reed-Hill, R. E., R. Abbaschian, *Physical metallurgy principles*. PWS Publishing Company, 1992.
- [76] Boyce B. L., M. F. Dilmore, *The dynamic tensile behavior of tough, ultrahigh-strength steels at strain rates from 0.0002 s^{-1} to 200 s^{-1}* . *International Journal of Impact Engineering* 36 (2009): 263-271.
- [77] Clausen A. H., T. Austad, *Split-Hopkinson tension bar: experimental set-up and theoretical considerations*. Report no. R-16-02, Norges Tekniske Naturvetenskapliga Universitet, Trondheim, 2002.
- [78] Professor Bertram Hopkinson. Available from <http://www-g.eng.cam.ac.uk/125/1900-1925/hopkinson.html>.
- [79] Split Hopkinson Pressure Bar Apparatus. An historic mechanical engineering landmark. Designated by the American Society of Mechanical Engineers. Designation Ceremony Southwest Research Institute, Texas, 2006.
- [80] Kinra V. K., A. Wolfenden, *M³D: Mechanics and mechanisms of material damping*. American society for testing and materials, 1992.
- [81] Graff K. F., *Wave motion in elastic solids*. Oxford University Press, 1975.
- [82] Follansbee P.S., C. Frantz, *Wave propagation in the Split Hopkinson pressure bar*. *Journal of Engineering Materials and Technology* 105 (1983): 61-66.
- [83] Hartley R. S., T. J. Cloete, G. N. Nurick, *An experimental assessment of friction effects in the split Hopkinson pressure bar using the ring compression test*. *International Journal of Impact Engineering* 34 (2007): 1705-1728.
- [84] Warren T. L., M. J. Forrestal, *Comments on the effect of radial inertia in the Kolsky bar test for an incompressible material*. *Experimental Mechanics* (2009).
- [85] Swedish standards institute, *SS-EN 10020: Definition and classification of grades of steel*. SIS, 2000.
- [86] Swedish standards institute, *SS-EN 10088-1:2005- Stainless steels-Part 1: List of stainless steels*. SIS, 2005.
- [87] Ring Groth M., *Adhesive bonding and weldbonding of stainless steel*. Licentiate thesis, Department of Materials and Manufacturing Engineering, Luleå University of Technology. Luleå, 1998.

- [88] Honeycombe R. W. K, H. K. D. H Bhadeshia, *Steels microstructure and properties*, second edition. R. W. K Honeycombe and H. K. D. H Bhadeshia, 1995.
- [89] Lindgren L-E., K. Domkin, S. Hansson, *Dislocations, vacancies and solute diffusion in physical based plasticity model for AISI 316L*. Mech. of Materials 40 (2008): 907-919.

Paper A

MATERIAL MODELLING AND PHYSICAL BASED MODELS WITH PARTICULAR EMPHASIS ON HIGH STRAIN RATES

Lars-Erik Lindgren, Dan Wedberg

International Symposium on Plasticity 2009

MATERIAL MODELLING AND PHYSICAL BASED MODELS WITH PARTICULAR EMPHASIS ON HIGH STRAIN RATES

Lars-Erik Lindgren*, and Dan Wedberg**

*Department of Mechanical Engineering, Luleå University of Technology, 971 87
Luleå, Sweden, lel@ltu.se

**AB Sandvik Coromant, Metal Cutting Research, 811 81 Sandviken, Sweden,
dan.wedberg@sandvik.com

ABSTRACT- The problem of calibrating material models with tests in a limited range of conditions and then applying outside this range is discussed. This is the case when machining simulations are performed where very high strain rates ($>50000\text{s}^{-1}$) can be obtained. The paper discusses the Johnson-Cook model, an empirical model that is common for high strain rate applications and a physical based dislocation density model. Test data for AISI 316L ranging from 0.001 to 10s^{-1} and room temperature up to 1300°C are used for calibration of the models and thereafter additional tests up to 9000s^{-1} at varying initial temperatures are compared with the model predictions.

INTRODUCTION: The description of material behaviour is crucial for all simulations of material deformation processes. Simulation of machining [Vaz jr et al. 2007] has several numerical as well as modelling complications. One problem is to obtain test data for the material at high strain rates. Thus it is always necessary to extrapolate the material model outside the range of calibration. This paper illustrates the complexity of the mentioned problem for two different types of material models describing the mechanical behaviour of AISI 316L.

PROCEDURES, RESULTS AND DISCUSSION: A dislocation density model and the Johnson-Cook model are used as examples when discussion extrapolation of models to high strain rates.

Empirical and physical based models: Physical based models are models where the physical mechanisms are underlying the deformation in contrast to empirical models which are of a more curve-fitting nature. However, due to the need for averaging and also limited knowledge about some of the relations making up the model, physical based models need also be calibrated. Two different types of physical based models exist. One option is to explicitly include variables from physics as internal state variables. The other possibility is to determine the format of the constitutive equation based on knowledge about the physical mechanisms causing the deformation. The latter is a so-called “model-based-phenomenology” [Frost and Ashby 1982]. Some advantages of physical based models are that they may have links, via parameters like grain size etc, to models for microstructure evolution [Kocks & Mecking 2003] and may have a larger domain of validity. It is also hoped that they can be extrapolated outside their range of calibration. This requires that the physical mechanisms implemented in the models still dominate the deformation in the extended range.

Scope of study: A dislocation density model is compared with the classical Johnson-Cook model [Johnson and Cook 1983]. Previous model development [Lindgren et al. 2008] has been based on a strain range up to 0.6, strain rate up to 10s^{-1} , and temperatures up to 1300°C . In this paper the previously calibrated dislocation density model and the Johnson-Cook model are compared with the new data for high strain rates obtained via split Hopkinson pressure bar tests (SHPB).

Numerical procedure: A toolbox has been implemented in MatlabTM where parameter calibration can be done. A constrained gradient method was used in the minimization algorithm and the radial return stress-strain algorithm was used in order to be able to apply varying strain and temperature paths to the model. The temperatures were measured during the tests at low strain rates and computed assuming adiabatic heating for the tests in the high strain rate. The data for the Johnson-Cook model that is used to generate the results shown below are given in Table 1. The model is written as

$$\sigma_y = \left(A + B \bar{\epsilon}^p \right) \left(1 + C \ln \left(\frac{\dot{\bar{\epsilon}}}{\dot{\bar{\epsilon}}_{ref}} \right) \right) \left(1 + \left(\frac{T - T_{room}}{T_{melt} - T_{room}} \right)^m \right) \quad (1)$$

where $\bar{\epsilon}^p$ is the effective plastic strain and T is the temperature.

Table 1: Material Parameters for Johnson-Cook Model.

Case	A	B	n	C	$\dot{\bar{\epsilon}}_{ref}$	m
Low	248 MPa	1007 MPa	0.452	0.0727	1 s^{-1}	0.259
High	245 MPa	580 MPa	0.587	0.117	1 s^{-1}	0.733

Results: Some examples of measured stress-strain curves compared with the dislocation density model are shown to the left in Fig. 1, from Lindgren et al. [2008]. The model gives an overall good agreement in the range from 0.001 to 10s^{-1} and room temperature up to 1300°C . The Johnson-Cook model does not give any good results when subjected to the entire test data in Lindgren et al. [2008] due to its simple form. Therefore only the curves, shown in the right part of Fig. 1, were used to calibrate it. The obtained parameters are called ‘Low’ in Table 1. These two models were then used to model the response in the high strain rate range and the results are shown in Fig. 2. The Johnson-Cook model can be re-calibrated to fit the high strain rate data well (not shown in paper) and the parameters denoted ‘High’ in Table 1 are obtained but then the fit to the low strain rate range will be poor.

CONCLUSIONS: Re-calibration is not a consistent approach using a physical based model. Rather, the discrepancy indicates that new physics are entering during the deformation at these high strain rates. The correct approach will be to determine the underlying physics, implement it into the model and then re-calibrate. The possible phenomena for deviation may be martensite formation, twinning, a more even structure of immobile dislocation or drag forces on moving dislocations.

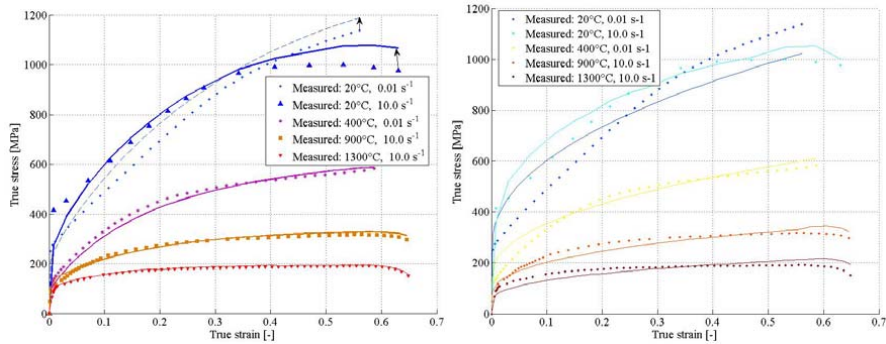


Fig. 1. Flow stress curves for dislocation density model, left, calibrated for strain rates up to 10 s^{-1} , and temperatures up to 1300°C [Lindgren et al. 2008] and, right, for Johnson-Cook model calibrated using the shown curves. The lines are computed values.

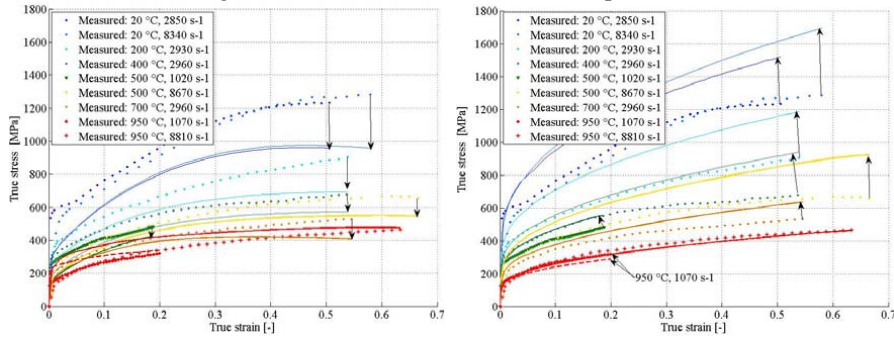


Fig. 2. Flow stress curves for dislocation density model, left, and for Johnson-Cook model, right, extrapolated to high strain rates. The lines are computed values.

Acknowledgement: Swedish Research Council, grant no 1397-2005.

REFERENCES:

- Frost, H.J. and Ashby, M.F., 1982, "Deformation-Mechanism Maps - The Plasticity and Creep of Metals and Ceramics", Pergamon Press.
- Johnson, G. and Cook, W., 1983, "A constitutive model and data for metals subjected to large strains, high strain rates and high temperatures" Proc. 7th Int. Symp. on Ballistics, pp. 541-547. Den Haag, The Netherlands.
- Kocks, U.F. and Mecking, H., 2003, "Physics and phenomenology of strain hardening: the FCC case", Progress in Materials Science **48**, 171.
- Lindgren, L.-E., Domkin, K., and Hansson, S., 2008, "Dislocations, vacancies and solute diffusion in physical based plasticity model for AISI 316L", Mech. of Materials **40**, 907.
- Vaz jr, M., Owen, D., Kalhori, V., Lundblad, M., and Lindgren, L.-E., 2007, "Modelling and simulation of machining processes", Arch Comput Methods Eng **14**, 173.

Paper B

VERIFICATION AND VALIDATION OF MACHINING SIMULATIONS FOR SUFFICIENT ACCURACY

Lars-Erik Lindgren, Dan Wedberg, Ales Svoboda

International Conference on Computational Plasticity 2009

VERIFICATION AND VALIDATION OF MACHINING SIMULATIONS FOR SUFFICIENT ACCURACY

Lars-Erik Lindgren*, Dan Wedberg[†] and Ales Svoboda[‡]

^{*†}Department of Applied Physics and Mechanical Engineering
Luleå University of Technology, 971 87 Luleå, Sweden

*e-mail: lel@ltu.se, [‡]e-mail: ales.svoboda@ltu.se web page: <http://www.ltu.se>

[†]AB Sandvik Coromant
811 81 Sandviken, Sweden

Email: dan.wedberg@sandvik.com - Web page: <http://www.sandvik.com>

Key words: Machining, Robustness, Validation, Variability, Finite element simulation.

1 INTRODUCTION

Finite element simulation of machining processes is still a challenge both with respect to numerical methods and the physics to be modelled. Therefore, verification and validation are essential. The paper discusses these issues and particularly the relation to the variations of the process itself and requirements on accuracy of models when assessing their validity. The numerical problems in modelling this process are several but most notably are the need for reliable remeshing and contact algorithms. The modelling problem is particular problematic regarding the material behaviour and models for the contact behaviour^{1,2}.

2 TERMINOLOGY

A *model* is a device used to represent certain aspects of phenomena, processes and/or objects in the real world. Its purpose is to predict real world behaviour. It is embodied in a finite element model in the current context. Those aspects of a real world phenomenon that are in focus when evaluating a model are the *scope of the model*. The concept of verification and validation (V&V) defined in below is taken the papers by Oberkampf³ and co-workers in the following. The term *verification* is the ‘substantiation that a computerized model represents a conceptual model within specified limits of accuracy⁴. Thus verification is defined as the process of confirming that the equations that are defining the mathematical model are solved correctly and with expected convergence properties. It requires stable and consistent numerical algorithms⁵⁻⁷. This is the code verification process where different analytical solutions, benchmark cases and other numerical tools are used to check the computer code. *Validation* is the checking of the accuracy of the model with respect to real world behaviour. Thus if verification is the checking that the equations are solved correctly, then validation can be considered as the checking that the correct equations are solved. The validation process is strongly related to the scope of the model and the needed accuracy. The aim is to create a *sufficient valid and accurate model*. The validation is done by comparison with experimental results from the studied problem. The use of measurements to determine

necessary input to model parameters, like material properties, is called *calibration*. It is important to keep the distinction between calibration and validation⁸. Belytschko and Mish⁹ discuss different types of uncertainties and the problem of creating a valid model. Errors are introduced due to uncertain input data due to insufficient measurements. They are epistemic or reducible errors¹⁰. Irreducible errors are caused by stochastic variations. This is also related to the question about robustness of the process and the model. *Prediction* is the modelling and simulation of a specific case different from the validated case. Oberkampf *et al.*³ discuss the problem of ‘how nearby’ the prediction case is to the validated case. This determines the confidence the validation case gives that the predicted will also be sufficient accurate.

3 VERIFICATION OF MODELS

The verification of a finite element model, assuming that the used fe-code is correct, focuses on obtaining convergence with respect to the element sizes as well as time stepping. The latter is closely related to convergence criteria in the nonlinear solution procedure. However, for an explicit finite element code, it is only the mesh size that is an issue.

The experience from the authors is that the refinement of a model down to stable results can be very hard. We have found that the results seem to be stable for a number of refined models and then after one more refinement there will be large changes in the results. An example of this is the use of adaptive meshing and time stepping in MSC.Marc. One model was run with the (default) convergence criterions of residual force norm of 0.1 and displacement norm of 0.1. Both criteria must be fulfilled during equilibrium iterations. The model corresponds to a case described later (cutting speed of 240 m/min and feed of 0.15 mm/rev) but another material model was used. The smallest element size was 7.5 μm and the radius of the cutting tool was 45 μm . The adaptive time stepping then required about 3400 increments. We initially believed this was an accurate model and it gave a cutting force of 780 N. Another analysis was executed where the only change was the reduction in the displacement norm criterion from 0.1 to 0.08. The fulfillment of this criterion required 13300 increments in the analysis. The cutting force became 620N.

4 SCOPE OF MACHINING MODELS AND VALIDATION

The scope of machining models can be the need to predict chip formation, i.e. the shape of formed chip, cutting forces and/or residual stresses in the workpiece. The experience from the authors is that predicting chip formation requires a more accurate model than prediction of residual stresses and the determination of cutting forces is ‘easiest’. Validation of models can be done by measuring chip shape from quick stop experiments^{11, 12}, dynamic measurement of cutting forces and x-ray or neutron diffraction measurements for residual stresses. Each of these methods has difficulties. The quick stop case does not preserve the chip shape that exists during the machining as there is an unloading of the chip. The inertia forces, pressure from the tool and, more important, temperature gradients have disappeared. The cutting force experiments are the most established and straightforward to do and are discussed in the next chapter. Measurements of residual stresses is in fact a measurement of existing elastic strains

and do have problem with the resolution of the gradients in along the surface as well as when trying to evaluate the stresses beneath the surface layer in the material².

5 ROBUSTNESS OF MACHINING

A series of cutting force measurements were done by Kalhori and Lundblad, paper V in reference ² and repeated in this study. They were orthogonal cutting tests with velocities and feeds and measurements as shown in Table 1. The difference is computed as

$$\% = \frac{Force_{Current} - Force_{Kalhori}}{Force_{Kalhori}} \cdot 100 \quad (1)$$

Our measurements give larger cutting forces, particularly for the smaller feed cases. An investigation showed that, although the experiments are nominally the same, there are differences with respect to micro geometry of tool as well as variations in the material, AISI 316L. The nominal tool radius is 50µm. The real edge radius was 45µm in the case of Kalhori and 60µm in our case. Furthermore, it has been observed that the material, AISI 316L, has varying properties for different batches in the production. The stress-strain curves at room temperature and a strain rate of 0.01s⁻¹ of the two different batches are shown in figure 1. The batch reaching the highest stress, 820 MPa, has the smallest strain to necking, 0.38 [-], whereas the variant used in our tests has a peak stress of 785 MPa and elongation of 0.40 [-].

Test #	Cutting speed [m/min]	Feed [mm/rev]	Cutting depth [mm]	Kalhori		Current		Difference %	
				Cutting force [N]	Feed force [N]	Cutting force [N]	Feed force [N]	Cutting force [N]	Feed force [N]
180a	180	0.05	3.0	404	360	446	437	10	21
180b	180	0.15	3.0	890	584	960	592	8	1
240a	240	0.05	3.0	391	357	442	439	13	23
240b	240	0.15	3.0	857	520	929	560	8	8

Table 1 : Orthogonal cutting experiments.

6 VALIDATION OF MODELS

Simulation of two of the cases in Table 1 was done with a tool radius of 45µm, as Kalhori had, and with 60µm, corresponding to current measurements, see Table 2. Test 240b was also simulated with a radius of 45µm and an increase of flow stress with 10% at all temperatures and strain rates. That case gave a cutting force of 1114 N (+7%) and feed force of 495N (+5%).

Test #	Cutting speed [m/min]	Feed [mm/rev]	Cutting depth [mm]	Radius 45 µm		Radius 60 µm		Difference %	
				Cutting force [N]	Feed force [N]	Cutting force [N]	Feed force [N]	Cutting force [N]	Feed force [N]
180a	180	0.05	3.0	345	286	429	347	24	21
240b	240	0.15	3.0	1041	470	1061	531	2	13

Table 2 : Computed forces for varying tool radii.

7 DISCUSSIONS

The conclusion is that there is a need for benchmarking software and also a careful check of convergence of used model in the verification process and that the requirements to consider a model to be validated must consider the process variation in industry. This, in the case the scope is cutting forces, may be that agreement between model and measurements around 10% are quite good.

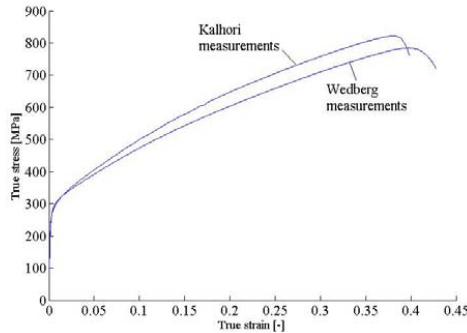


Figure 1: Flow stress curves of two variants of AISI 316L.

REFERENCES

- [1] M. Vaz jr, D. Owen, V. Kalhori, M. Lundblad and L.-E. Lindgren, "Modelling and simulation of machining processes", *Arch Comput Methods Eng* **14**, 173-204. (2007).
- [2] V. Kalhori, "Modelling and simulation of mechanical cutting," *Department of Mechanical Engineering*, Luleå University of Technology, Luleå, 2001.
- [3] W. L. Oberkampf, T. G. Trucano and C. Hirsch, "Verification, validation, and predictive capability in computational engineering and physics", *Applied Mechanics Reviews* **57**, 345-384. (2004).
- [4] W. L. Oberkampf and T. G. Trucano, "Verification and validation in computational fluid dynamics", *Progress in Aerospace Sciences* **38**, 209-272. (2002).
- [5] T. Hughes, "Analysis of transient algorithms with particular reference to stability behavior," *Computational methods for transient analysis*, T. Belytschko and T. Hughes (Editors), vol. 1, North-Holland, (1983).
- [6] X. N. Meng and T. A. Laursen, "Energy consistent algorithms for dynamic finite deformation plasticity", *Computer Methods in Applied Mechanics and Engineering* **191**, 1639-1675. (2002).
- [7] T. Belytschko, W. K. Liu and B. Moran, *Nonlinear finite elements for continua and structures*, John Wiley & Sons, (2000).
- [8] T. G. Trucano, L. P. Swiler, T. Igusa, W. L. Oberkampf and M. Pilch, "Calibration, validation, and sensitivity analysis: What's what", *Reliability Engineering & System Safety* **91**, 1331-1357. (2006).
- [9] T. Belytschko and K. Mish, "Computability in non-linear solid mechanics", *Int J Numer Meth Engng* **52**, 3-21. (2001).
- [10] W. L. Oberkampf, J. C. Helton, C. A. Joslyn, S. F. Wojtkiewicz and S. Ferson, "Challenge problems: Uncertainty in system response given uncertain parameters", *Reliability Engineering & System Safety* **85**, 11-19. (2004).
- [11] J. T. Lin, D. Bhattacharyya and W. G. Ferguson, "Chip formation in the machining of sic-particle-reinforced aluminium-matrix composites", *Composites Science and Technology* **58**, 285-291. (1998).
- [12] G.-L. Chern, "Development of a new and simple quick-stop device for the study on chip formation", *International Journal of Machine Tools and Manufacture* **45**, 789-794. (2005).

Paper C

SIMULATION OF MECHANICAL CUTTING USING A PHYSICAL BASED MATERIAL MODEL

Vahid Kalhori, Dan Wedberg, Lars-Erik Lindgren

International Journal of Material Forming, 3, 2010
International ESAFORM Conference on Material Forming 2010

SIMULATION OF MECHANICAL CUTTING USING A PHYSICAL BASED MATERIAL MODEL

Vahid Kalhori¹, Dan Wedberg¹, Lars-Erik Lindgren²

¹ AB Sandvik Coromant, Metal Cutting Research, 811 81 Sandviken, Sweden

² Luleå University of Technology, Department of Mechanical Engineering, 971 87 Luleå, Sweden

ABSTRACT: A dislocation density material model based on model-based-phenomenology has been used to predict orthogonal cutting of stainless steel Sanmac 316L. The chip morphology and the cutting forces are used to validate the model. The simulated cutting forces and the chip morphology showed good conformity with practical measurements. Furthermore, simulation of cutting process utilizing the dislocation density based material model improved understanding regarding material behaviour such as strain hardening and shear localization at the process zone.

KEYWORDS: Metal Cutting, Chip morphology, Material model, Dislocation density, Finite element simulation

1 INTRODUCTION

Modern product development puts greater demands on the repeatability and a more predictable product development process. Rapid changes in the market require shorter lead-times, higher degree of innovation and more flexible products and services. The consequence is that fewer mistakes are allowed during the product development process. Simulations are used for two purposes: first, they can be used to verify product performance and efficiency within conceptual phase or detail design phase of a product development process. Secondly, instead of time and resource consuming trial and error activities in the workshop, they can be used as a test bench to increase awareness and understanding of the physical behavior of both the work piece materials as well as cutting tools during metal cutting operation in a shorter time. This makes it possible, within a shorter time frame, to produce a number of innovative solutions that create greater customer value in terms of accessibility, quality, productivity and profitability.

However, modelling of work piece material has been one of the more challenging areas of research related to the metal cutting process. Apparently, there is a need for a reliable material model that can predict the thermo-mechanical behaviour of materials at very high deformation rates and high temperatures occurring in metal cutting. This may give more accurate analysis of; chip forming mechanisms, cutting forces, temperature gradients at different cutting zones, wear of the insert, surface integrity and residual stresses on the work piece surface. During recent decades, several different material models have been proposed for this reason. These can be dividing into two major categories. The empirical material models such as Johnson & Cook [2] power law models, etc. which aims to covering the thermo-

mechanical behaviour of work piece material at high strain-rates including the material failure. These are the most frequent used by researchers to characterize the material behaviour, since the data has been more easily available via the literature but also easier to implement in commercial FE-programs. The second category is the physically based material models, which consider the underlying physical process. There are two different types of physical based models. One option is to explicitly include variables from physics as internal state variables. The other possibility is to determine the form of the constitutive equation based on knowledge about the physical mechanisms causing the deformation. The former is a so-called “model-based-phenomenology” [1]. This paper present an improved physical based material model initially developed by Lindgren, Domkin and Hansson [4] which accounts for high deformation rates up to 10000 s⁻¹. The model is used to predict chip formation and cutting forces using finite element simulations.

2 MATERIAL MODEL

A plasticity model with a rate-dependent yield limit is used in the current study. The latter is described below.

2.1 DISLOCATION DENSITY MODEL

The dislocation density model consider dislocation glide and climb processes contributions to the plastic straining. The yield limit in this approach is separated into two components according to

$$\sigma_y = \sigma_G + \sigma^* \quad (1)$$

where σ_G and σ^* are the long-range athermal component respectively the short-range contributions to the flow stress. The first component, σ_G , is the stress needed to overcome the long-range interactions lattice distortions

due to the dislocation substructure. The second component, σ^* , is the stress needed for the dislocation to pass through the lattice and to pass short-range obstacles. Thermal vibrations will then also assist the dislocation when passing an obstacle. The long-range stress component is commonly written as;

$$\sigma_G = m\alpha Gb\sqrt{\rho_i} \quad (2)$$

where m is the Taylor orientation factor, α is a proportionality factor, G is the temperature dependent shear modulus, b is the magnitude of Burgers vector and ρ_i is the immobile dislocation density. The short-range stress components may be written as,

$$\sigma^* = \tau_0 G \left(1 - \left(\frac{kT}{\Delta f_0 G b^3} \ln \left(\frac{\dot{\epsilon}_{ref}}{\dot{\epsilon}} \right) \right)^{1/q} \right)^{1/p} \quad (3)$$

where Δf_0 denote the required free energy needed to overcome the lattice resistance or obstacles without assistance from external stress, τ_0 denote the athermal flow strength required to move the dislocation past barriers without assistance of thermal energy, $\dot{\epsilon}_{ref}$ denote the reference strain rate. The exponent p and q characterize the barrier profiles and usually have values between $0 \leq p \leq 1$ respectively $0 \leq q \leq 2$.

2.1.1 Structure evolution

The evolution of the structure is considered to consist of a hardening and a recovery process. The used model assumes that the mobile dislocation density is stress and strain independent and much smaller than the immobile ones. Hence the evolution equation is written;

$$\dot{\rho}_i = \dot{\rho}_i^{(+)} + \dot{\rho}_i^{(-)} \quad (4)$$

where index i denotes the immobile dislocations. The increase in immobile dislocation density is assumed to be related to the plastic strain rate and may therefore be written according to

$$\dot{\rho}_i^{(+)} = \frac{m}{b} \frac{1}{\lambda} \dot{\epsilon}^p \quad (5)$$

where λ denote the mean free path which is a function of the size of the grains and the dislocation subcell diameter. The recovery may occur by dislocation glide and/or climb. The former is described by

$$\dot{\rho}_i^{(-)} = \Omega \rho_i \dot{\epsilon}^p \quad (6)$$

where Ω is a recovery function which depends on the temperature and strain rate. Recovery by climb is describe by

$$\dot{\rho}_i^{(-)} = 2c_\gamma D_v \frac{c_v}{c_v^{eq}} \frac{Gb^3}{kT} (\rho_i^2 - \rho_{eq}^2) \quad (7)$$

where c_v is the vacancy fraction, c_v^{eq} is the thermal equilibrium vacancy concentration, D_v is the diffusivity and c_γ is a calibration parameter. More details are found in [4].

2.2 CALIBRATION OF MATERIAL MODEL

It is well known that metal cutting is a manufacturing process involving large deformation and deformation at high strain rates. However, the calibration of the dislocation density model presented in [4] was based upon uniaxial compression tests at low strain rates, with a maximum strain rate of 10 s^{-1} , and temperatures ranging up to 1300°C . Additional dynamic tests have therefore been performed. The tests were performed by Split-Hopkinson pressure bar tests (SHPB) for strain rates and temperatures up to maximum 9000 s^{-1} respectively 950°C . From some selected stress-strain curves at different strain rates and temperatures a determination of material parameters was done by a developed toolbox in Matlab using an optimization method.

3 EXPERIMENTAL SET UP

3.1 SANMAC 316L

An austenitic stainless steel of grade SANMAC 316L with the chemical composition given in Table 1 was used in these experimental tests. It is a machinability improved hot worked stainless bar steel which has been annealed, straightened, peel turned and polished to final delivery dimensions.

Table 1: Chemical composition of SANMAC 316L [wt.%]

C	Si	Mn	P	S
0.009	0.31	1.71	0.031	0.023
Cr	Ni	Mo	V	N
16.86	10.25	2.04	0.048	0.040

3.2 MECHANICAL CUTTING EXPERIMENTS

The experimental machining set-up included both force measurements and quick-stop tests in order to capture the cutting and feeding forces and the chip morphology. The former was done under orthogonal cutting using a three component Kistler dynamometer of type 9263 together with a 300 Hz low pass filter. The quick-stop tests were performed with in-house developed equipment based on the "shear pin" design where the turnable tool holder rested on a hardened break pin at the front end. By a sudden impact, in this case by an air-gun, the break pin was broken and the tool holder could accelerated away and out of the cutting action. The chip from the interrupted cutting was then removed, embedded, grounded, polished and etched for estimations of chip thickness and shear angle. All tests were performed using TNMG 160 408-QF insert made by AB Sandvik Coromant. This is a CVD-coated insert for finishing to roughing of steel at turning applications.

Table 2: Experiment planning

Test no	Cutting speed v_c [m/min]	Feed f_n [mm/rev]
1	100	0.25
2	180	0.15
3	240	0.15
4	300	0.25

The combination of CVD TiCN-Al₂O₃-TiN coating and a tough substrate make this grade (4015) a good choice for continuous as well as intermittent turning operations. The cutting insert geometry is designed with a cutting edge radius of 60 μ m, a primary land of 0.15 mm and a rake face angle of -6°. The chosen cutting parameters in order to validate the model is presented in Table 2. The cutting depth was chosen to be 3 mm.

4 FINITE ELEMENT SIMULATION

The orthogonal cutting process has been analysed utilizing the finite element program AdvantEdge[6]. This software is based on an updated Lagrangian formulation combined with an explicit time integration scheme. A staggered method for coupled transient mechanical and heat transfer analysis is used. A six-node quadratic triangle element with four integration points is used. A continuous updating of the finite element mesh facilitates the analysis facing large excessive deformations and shear localization[3]. The mesh refinement at different deformation zones occurs through a plastic strain energy error estimator. Since the physical based material model is not available in AdvantEdge, a user routine for the material model was developed. This was based on a thermo-elasto-plastic with mixed isotropic and kinematic hardening with a multiplicative decomposition plasticity formulation [5] which takes account high strain rates.

4.1 FRICTION

It is generally known that the elasto-plastic behaviour of the moving surfaces is strongly related to an interaction between contact pressure, surface integrity and surfaces temperature. Usually, the chip – insert interface is divided in sticking region and slipping region. The contact behaviour of the sticking region may be treated by implementing the ultimate shear stress principle for the work piece material at the contact [8]. While the state of the shear stress on the interface reaches the maximum value, the relative motion of the contact surfaces at the slipping region use the Coulomb friction model. Consequently, the total amount of feed force is assumed to be the sum of shear forces at the stick and slip regions. However, the contact pressure perpendicular to the cutting insert shear region is often neglected through the discretization error at the tertiary cutting zone but also the way the material model is treated. In the current study the constitutive isotropic hardening material model and the mixed isotropic-kinematic hardening material model was compared. The later showed an improvement

of the feed force comparing to the experimental results when the same friction condition was chosen. However, since it was not possible in AdvantEdge to determine the local friction coefficient at the contact nodes an average friction coefficient of 0.6 was chosen. This was calibrated by varying the friction coefficients from 0.0 to 1.0 with a step of 0.2 and comparing the result with experimental measurements of feed force. It turned out that there was no significant difference in the force level for the friction coefficients above 0.6. Therefore, the friction coefficient of 0.6 was chosen for further simulations.

5 RESULTS

The simulated chip morphology was compared with the experimental measurements through a comparison of shear plane angel Φ and ratio between cut and uncut chip thickness Λ . The shear plane angle was evaluated by drawing a tangent line from the cutting edge to the material/chip intersection point, see Figure 1. However, deformations along the shear plane do not follow a straight line. Therefore, it may be difficult to determine this angel accurately using a straight line [7].

In the case of the cut and uncut chip thickness ratio, the average thicknesses from the quick-stop tests were calculated from the chip profile which was determined via a light microscope.

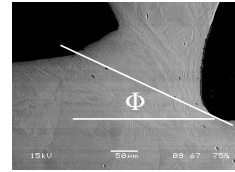


Figure 1: Specimen from a quick-stop test, $v_c=180$ m/min and $f_n=0.15$ mm/rev, showing evaluation of the shear plane angle.

It is shown in Table 3 that the simulated chip is about 40% thicker for the lower feed (0.15 mm) compared with the measured. The measured cutting forces were also compared with predicted. As shown in Table 4 there are a good agreement between predicted and measured cutting forces in both directions except for the feed force at the cutting speed of 100 m / min. The simulated feed force is about 30% lower compared to the measured. However, shear localization for different tests varied depending on the feed from 40 μ m to 100 μ m. Shear band widths were between 5 to 9 elements wide when

Table 3: Measured and computed chip morphology

Test no	Measured		Simulated	
	Λ	Φ	Λ	Φ
1	1.75	22°	1.8	27°
2	1.32	23°	1.9	24°
3	1.35	22°	1.8	23°
4	1.58	26°	1.8	26°

Table 4: Measured and computed cutting forces

Test no	Measured		Simulated	
	F_c [N]	F_f [N]	F_c [N]	F_f [N]
1	1725	1084	1720	800
2	960	592	990	550
3	929	560	980	540
4	1415	718	1500	700

utilizing the error estimator based on plastic strain energy. The thermoplastic shear localisation is shown in Figure 3a-3b, which presents the distribution of the temperature and yield stress for thermal softening. Highly localised plastic deformation causes the temperature to rise sharply, well above the neighbouring regions, which in turn, causes the yield stress to decrease. This corresponds to increasing in dislocation density and vacancies as shown in Figures 4a-4b. The regions of low yield stress are more subjected to larger plastic deformations. The cyclical response of localised plastic deformation, temperature rise, yield stress reduction and large and localised deformation led to a significant upward movement of the portion of the chip above the shear band, which leads to the segmented chip formation process.

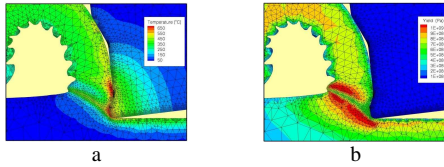


Figure 3: Distribution of temperature and yield stress at primary deformation zone, $v_c=100$ m/min, $f_r=0.25$ mm/rev. a) Temperature distribution. b) Yield stress

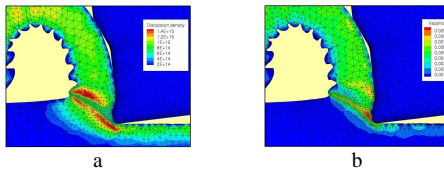


Figure 4: Distribution of dislocation density and vacancies at primary deformation zone, $v_c=100$ m/min, $f_r=0.25$ mm/rev. a) Dislocation density. b) Vacancies.

6 DISCUSSIONS AND CONCLUSIONS

A physical based material model with emphasis on high strain rates, up to 10000 s^{-1} , was developed and used successfully for prediction of chip formation in metal cutting. This enables to make a more detailed microscopic study of the process zone and to build good understanding regarding the interaction between strain hardening, thermal softening and shear localisation during chip formation. This further enhances the understanding of deformation mechanisms in cutting zone and leads to better process planning and

development of cutting tools with improved durability, performance and process safety. The predicted cutting forces agreed well with the experimental measurements. Except for feed force at cutting speed 100 m/min which was about 30% lower in simulation compared to the measured. It is believed that this was due to a tendency to BUE which occur at lower cutting speeds and are difficult to capture in simulations.

Furthermore, in the current study the constitutive isotropic hardening material model and the mixed isotropic-kinematic hardening material model were compared. The later showed an improvement of the feed force comparing to the experimental results when the same friction condition was chosen. This indicates a need for further investigation regarding the effect of hardening rule on deformations especially on the tertiary deformation zone in the future studies.

However, the predicted chip thickness ratio was over estimated comparing to the quick-stop measurements. A discrepancy is believed to happen since no failure criteria were implemented in the model. Thermal softening is not enough to predict the discontinuous chip formation process. Hence the average chip thickness in simulations will be affected. This opens for future work to include the voids nucleation and damage evolution in the material model to achieve more realistic chip morphology.

ACKNOWLEDGEMENT

The financial support from the Swedish Research Council and AB Sandvik Coromant is gratefully acknowledged.

REFERENCE

- [1] Frost H.J., Ashby M.F., Deformation mechanism maps (1st ed.), The plasticity and creep of metals and ceramics, Pergamon Press, p. 6, 1982
- [2] Johnson G. R., Cook W. H.: A constitutive model and data for metals subjected to large strains, high strain rates and high temperatures. In: 7th Internat. Symposium on Ballistics, 514-546, 1983
- [3] Kalhori V., Modelling and simulation of mechanical cutting, Doctoral thesis, ISSN: 1402-1544, 2001.
- [4] Lindgren L-E, Domkin K., Hansson S., Dislocations, vacancies and solute diffusion in physical based plasticity model for AISI 316L, Mechanics of Materials, Volume 40, Issue 11, 907-919, November 2008
- [5] Simo J.C., Hughes T., Computational inelasticity, Springer Verlag, 1998.
- [6] Thirdwave, AdvantEdge User's Manual Version 4.7
- [7] Xie J., Bayoumi A., Zbib H. Characterization of chip formation and shear banding in orthogonal machining using finite element analysis. In *ASME International Conference on Material Instabilities: Theory and Applications*, 1994.
- [8] Zorev N.N., Interrelationship between shear process occurring along tool face and on shear plane in metal cutting. *ASME International Research in Production Engineering*, 85, 42-49, 1963.

Paper D

SIMULATION OF METAL CUTTING USING A PHYSICALLY BASED PLASTICITY MODEL

Ales Svoboda, Dan Wedberg, Lars-Erik Lindgren

Accepted for publication in
Modelling and Simulation in Materials Science and Engineering

Simulation of metal cutting using a physically-based plasticity model

Ales Svoboda¹, Dan Wedberg² and Lars-Erik Lindgren¹

¹Luleå University of Technology, 971 87 Luleå, Sweden

²AB Sandvik Coromant, 811 81 Sandviken, Sweden

Email: ales.svoboda@ltu.se

Abstract

Metal cutting is one of the most common metal shaping processes. Specified geometrical and surface properties are obtained by break-up of the material removed by the cutting edge into a chip. The chip formation is associated with a large strain, high strain rate and a locally high temperature due to adiabatic heating which make the modelling of cutting processes difficult. The present study compares a physically based plasticity model and the Johnson-Cook model. The latter is commonly used for high strain rate applications. Both material models are implemented into the finite element software MSC.Marc and compared with cutting experiments. The deformation behaviour of SANMAC 316L stainless steel during an orthogonal cutting process is studied.

MSC code: 74D10

Submitted to: Modelling and Simulation in Material Science and Engineering

1. Introduction

Cutting tool designs and cutting process parameters may be optimized by experimental measurements or by numerical analysis. In deformation zones in front of the tool and beneath the cutting edge, the material is deformed plastically by simultaneous action of large compressive and shearing stresses. The friction forces and dissipative plastic work generate high temperatures. This makes direct observations in the cutting zone during the machining difficult. Alternatively, the chip generation and flow may be observed by freezing the motion using quick-stop techniques. Nevertheless, these measurements are time consuming and a limited amount of information can be gained from experiments in comparison with simulations.

The finite element method (FEM) is the most common numerical method used to analyse metal cutting operations, see (Vaz *et al* 2007). However, the modelling of the special conditions in the cutting zone requires a robust finite element software including capabilities such as thermo-mechanical coupling, friction models, material models and effective contact algorithms. An additional degree of complexity is caused by the necessity to model material removal. The finite element mesh distortion due to large deformations requires a remeshing technique in the case when a Lagrangian reference frame is used.

An important feature of a model for metal cutting is the material model. It must adequately represent the deformation behaviour during high rate loading and be able to account for strain hardening and strain softening, thermal softening as well as large variations in strain rate and temperature. In the majority of commercial FEM codes, the deformation behaviour of metals is represented by an empirical relationship, mostly in terms of the power law of strain and strain rate. These equations, relating the flow stress to the plastic strain, strain rate and temperature, are not based on any reasoning about underlying physics. The empirical relations are usually lacking in predictive capabilities beyond the derived range of experimental conditions at which they were

curve-fitted. It is therefore preferable to use models which are related to the underlying physics of the deformation coupled to the microstructure evolution. The advantage of using physically-based models is an expected larger domain of validity as compared with phenomenological models. However, the physically-based models must still be feasible for large scale computations. In the present study, which is part of a project aiming at development and validating models for machining, the physically-based dislocation density (DD) model is compared with the phenomenological Johnson-Cook (JC) plasticity model. The latter is commonly used in machining simulations. Both models were used to simulate orthogonal cutting of SANMAC 316L stainless steel, a material with a face-centred cubic (FCC) structure and low stacking fault energy. The steel has significant amounts of alloying elements which improve the corrosion resistance and the strength. These properties may be reduced during the machining when large residual tensile stresses are introduced. Residual stresses in the workpiece may also affect fatigue life of machined components. Therefore it is highly technically relevant to be able to predict a stress field after machining operations in order to optimize the machining parameters. The measurements of cutting forces and quick-stop tests were performed in order to evaluate accuracy and performance of the two material models. The simulated cutting forces, the chip morphology and dimensions are compared with the experimental results.

2. Material modelling

The material models discussed in the following sections were implemented into MSC.Marc software using user subroutine interface WKSPL. The subroutine makes it possible to introduce user-defined relations for the yield stress and the corresponding hardening slope as a function of temperature, equivalent plastic strain and equivalent plastic strain rate. The implementation of the material models is based on the additive decomposition of the spatial rate of the deformation tensor. A radial-return type algorithm was used for the integration of constitutive equations.

2.1 Physically- based plasticity model

Related to the theory of dislocation mechanics, Zerilli and Armstrong (1987) developed a constitutive model including different rate controlling mechanism for body-centred cubic (BCC) and FCC metals. Jaspers and Dautzenberg (2002) investigated the applicability of Zerilli-Armstrong (ZA) model to metal cutting simulations in the comparison with the JC model. Guo *et al* (2006) compared predicted chip morphology obtained using the conventional JC model with the Bammann-Chiesa-Johnson (BCJ) model. The dislocation mechanics based BCJ model, Bammann *et al* (1996), incorporates strain rate and temperature sensitivity, as well as damage, through a yield surface approach. Meyers *et al* (2002) presented a review of physically-based models for plasticity due to dislocation glide as well as twinning. They also discussed high strain rates phenomena. The paper has a particular focus on the ZA model. The current model is an explicit physically-based model which includes a coupled set of evolution equations for the internal state variables, dislocation density and vacancy concentration. Explicit means that these internal state variables are used instead of accumulated effective plastic strain in the previous mentioned (implicit) physically-based models. The concept of the dislocation density is the amount (length) of dislocations for a representative volume element divided by its volume. The model considers two different densities, a mobile and an immobile dislocation density. The microstructure is not represented explicitly, but in average sense. Basic equations of the model are shown in the next section. Details of the model, experimental procedure and parameter optimisation are to be found in Lindgren *et al* (2008) for low strain rates. The model is based on the dislocation glide mechanism; see Frost and Ashby (1982).

2.1.1 Flow stress and long-range term contribution

We assume that the flow stress can be expressed as a combination of the long range and the short range parts of the resistance to the motion of dislocations, e.g. Bergström (1969/70), Estrin (1998), Follansbee and Kocks (1988). Hence, the yield stress is defined by

$$\sigma_y = \sigma_G + \sigma^* \quad (1)$$

where σ_G is due to long-range interactions with the dislocation substructure. It is an athermal contribution and is related to the immobile dislocation density. One common assumption for the long-range term is

$$\sigma_G = m\alpha Gb\sqrt{\rho_i} \quad (2)$$

Here, m is the Taylor orientation factor transforming the effects of resolved shear stress in different slip systems into effective stress-strain relations and is affected by the texture, α is a proportionality factor, ρ_i is the immobile dislocation density, G is a temperature dependent shear modulus and b is the Burgers vector.

2.1.2 Flow stress and short-range term contribution

The short-range term σ^* in (1) is the thermally activated flow stress component. It is the stress needed for a dislocation to pass short-range obstacles and to move it through the lattice. The thermal vibrations of the lattice assist in overcoming obstacles. The velocity and the density of mobile dislocations are related to the plastic strain rate according to the Orowan equation

$$\dot{\epsilon}^p = \frac{\rho_m b \bar{v}}{m} \quad (3)$$

where \bar{v} is the average velocity of mobile dislocations having a density ρ_m . The time taken by a dislocation to move over a distance between two obstacles consists of a waiting time and a running time. The moving dislocation has a waiting time in front of an obstacle before it manages to pass the obstacle (provided it does not become immobile) and then moves to the next one. The average velocity is related to the waiting time, as the running time is assumed to be negligible. The waiting time and thereby the average velocity is assumed to depend on the Gibbs free-energy of activation ΔG for cutting or by-passing of obstacles (see Frost and Ashby (1982)), and on the temperature T . The average velocity is defined as

$$\bar{v} = \Lambda v_a \exp\left(-\frac{\Delta G}{kT}\right) \quad (4)$$

where Λ is the mean free path for dislocations between two obstacles, v_a is the attempt frequency which depends on the characteristics of obstacles and k is the Boltzmann's constant. The previous relations lead to

$$\dot{\epsilon}^p = \frac{\rho_m \Lambda b v_a}{m} \exp\left(-\frac{\Delta G}{kT}\right) \quad (5)$$

The short-range stress component σ^* may have a contribution from the lattice itself as well as from different kinds of obstacles. In FCC structures the lattice resistance to motion of dislocations is smaller as compared to the resistance provided by the discrete obstacles. Large obstacles will make the dislocations immobile and then contribute to the long-range term. One common relation between the activation energy ΔG and the short-range term representing a typical barrier encountered by a dislocation is

$$\Delta G = \Delta F \left[1 - \left(\frac{\sigma^*}{\hat{\tau}} \right)^p \right]^q \quad (6)$$

where ΔF is the total free energy required for a dislocation to overcome the lattice resistance or obstacles without aid from external stress. The quantity $\hat{\tau}$ is the athermal flow strength that must be exceeded in order to move dislocations across the lattice without the aid of thermal energy. The exponents $0 < p \leq 1$ and $0 < q \leq 2$ are related to the shape of energy barriers. The pre-exponential term in (5), which is approximated following Frost and Ashby (1982) to be constant, is expressed as

$$\dot{\epsilon}_{ref} = \frac{\rho_m \Lambda b v_a}{m} \quad (7)$$

Combining (5) with (6) and (7) yields

$$\dot{\epsilon}^p = \dot{\epsilon}_{ref} \exp \left\{ -\frac{\Delta F}{kT} \left[1 - \left(\frac{\sigma^*}{\hat{\tau}} \right)^p \right]^q \right\} \quad (8)$$

Rewriting (8) we obtain the short-range stress component as a function of the effective plastic strain rate, see Nemat-Nasser *et al* (2001)

$$\sigma^* = \hat{\tau} \left\{ 1 - \left[\frac{kT}{\Delta F} \ln \left(\frac{\dot{\epsilon}_{ref}}{\dot{\epsilon}^{pl}} \right) \right]^{1/q} \right\}^{1/p} \quad (9)$$

2.1.3 Evolution of dislocation density

The equation for the flow stress (2) requires evolution equations for internal state variables which are the dislocation density and the vacancy concentration. The mobile dislocation density is assumed to be much smaller than the immobile one, Bergström (1983), Estrin (2003). The immobile dislocation density is expressed in terms of hardening (+) and recovery (-) contributions. The presented model is tracing only the density of immobile dislocations ρ_i

$$\dot{\rho}_i = \dot{\rho}_i^{(+)} - \dot{\rho}_i^{(-)}_{(glide)} - \dot{\rho}_i^{(-)}_{(climb)} \quad (10)$$

Mobile dislocations move over a mean free path Λ before they are immobilized or annihilated. The immobile dislocation density is assumed to increase proportional to the plastic strain rate, which is related to the density of mobile dislocations, shown in (3), and inversely to the mean free path

$$\dot{\rho}_i^{(+)} = \frac{m}{b} \frac{1}{\Lambda} \dot{\epsilon}^p \quad (11)$$

The mean free path Λ is related to the grain size g and the dislocation subcell diameter s

$$\frac{1}{\Lambda} = \frac{1}{g} + \frac{1}{s} \quad (12)$$

The effect of grain size on flow stress, the Petch-Hall effect, is accounted for this way and contributes to the hardening. The size of subcells is related to the immobile dislocation density by the parameter K_c

$$s = K_c \frac{1}{\sqrt{\rho_i}} \quad (13)$$

The dislocation density may be reduced by different processes. Recovery, remobilization and/or annihilation of dislocations are proportional to the current dislocation density and controlled by dislocation climb and glide. Recovery by dislocation glide is described by

$$\dot{\rho}_i^{(-)} \text{ (glide)} = \Omega \rho_i \dot{\epsilon}^p \quad (14)$$

where Ω is a recovery function that depends on temperature and strain rate. This model accommodates only the dynamic recovery due to the strain rate. Static recovery controlled by diffusion climb is assumed to have the form

$$\dot{\rho}_i^{(-)} \text{ (c'limb)} = 2c_\gamma D_v \frac{c_v}{c_v^{eq}} \frac{Gb^3}{kT} (\rho_i^2 - \rho_{eq}^2) \quad (15)$$

In (15), c_v is the fraction of vacancies, c_v^{eq} is the thermal equilibrium vacancy concentration, D_v is the self-diffusion coefficient and c_γ is a material parameter related to the stacking-fault energy. The dislocation density decreases towards an equilibrium value ρ_{eq} .

2.1.4 Vacancy generation and migration

The calculation of the vacancy concentration is required for the solution of (15). The generation and motion of vacancies are coupled with the recovery of dislocations and diffuse solute atoms. The model presented here is only concerned with mono-vacancies. When a crystal is retained a sufficient time at a given temperature, an equilibrium level of vacancies is reached. Deforming the material or changing the temperature generates the excess vacancies. The effect of excess vacancies on the diffusion is accounted for via (16) as

$$\dot{c}_v^{ex} = \dot{c}_v - \dot{c}_v^{eq} = \left(\chi \frac{\sigma_y b}{Q_{vf}} + \varsigma \frac{c_j}{4b^2} \right) \frac{\Omega_0}{b} \dot{\bar{\epsilon}}^p - D_{vm} \left(\frac{1}{s^2} + \frac{1}{g^2} \right) (c_v - c_v^{eq}) \quad (16)$$

The stress in (16) is equal to the flow stress during a plastic deformation, the factor $\chi \sigma_y \dot{\bar{\epsilon}}^p$ is the fraction of the mechanical work needed for the vacancy formation, Q_{vf} is the activation energy for forming a vacancy, Ω_0 is the atomic volume and c_j is the concentration of thermal jogs. The parameter ς describes the neutralisation effect by vacancy emitting and absorbing jogs, c_v^{eq} is the equilibrium concentration of vacancies at a given temperature, c_v is the non-equilibrium vacancy concentration and D_{vm} is the vacancy migration. The equilibrium concentration at a given temperature is defined in (17) as

$$c_v^{eq} = \exp\left(\frac{\Delta S_{vf}}{k}\right) \exp\left(-\frac{Q_{vf}}{kT}\right) \quad (17)$$

In (17) ΔS_{vf} is the entropy increase when creating the vacancy. The rate of change in the vacancy equilibrium concentration is related only to the temperature change

$$\dot{c}_v^{eq} = c_v^{eq} \left(\frac{Q_{vf}}{T^2} \right) \dot{T} \quad (18)$$

Details of the model for vacancies and diffusion are to be found in Militzer *et al* (1994) and Lindgren *et al* (2008).

2.1.5 Stress update algorithm

The radial return operator for the integration of constitutive equations is used for updating the flow stress. Most plasticity models use the plastic strain as an internal variable. The DD model uses the immobile dislocation density ρ_i and the vacancy concentration c_v as internal state variables. The computation of the increment of effective plastic strain, which fulfils the consistency condition, requires calculation of the yield stress and hardening modulus for the current iteration of the plastic strain and internal state variables. The evolution of the internal state variables is governed by the coupled differential equations. The rate of change in immobile dislocation density given by (19) comes from (11) - (15). The rate of change in vacancy concentration, (20), is given by (16), (17) and (18).

$$\dot{\rho}_i = \left(\frac{m}{b} \frac{1}{\Lambda} - \Omega \rho_i \right) \dot{\bar{\epsilon}}^p - 2c_\gamma D_v \frac{c_v}{c_v^{eq}} \frac{Gb^3}{kT} (\rho_i^2 - \rho_{eq}^2) \quad (19)$$

$$\dot{c}_v = \left[\chi \frac{\Omega_0}{Q_{vf}} (\sigma_G + \sigma^*) + \varsigma \frac{c_j}{4b^2} \frac{\Omega_0}{b} \right] \dot{\bar{\epsilon}}^p - D_{vm} \left(\frac{1}{s^2} + \frac{1}{g^2} \right) (c_v - c_v^{eq}) + c_v^{eq} \left(\frac{Q_{vf}}{T^2} \right) \dot{T} \quad (20)$$

These equations are solved incrementally by an implicit Newton-Raphson method. Once the dislocation density and vacancy concentration are known, the hardening modulus and the flow stress can be evaluated. During the increment iteration the plastic strain rate is assumed constant. The hardening modulus in the incremental form is given by

$$H' = \frac{d\sigma_y}{d\bar{\epsilon}^{pl}} = \frac{\partial \sigma_y}{\partial \rho_i} \left(\frac{\partial \rho_i}{\partial \bar{\epsilon}^{pl}} + \frac{\partial \rho_i}{\partial c_v} \frac{\partial c_v}{\partial \bar{\epsilon}^{pl}} \right) + \frac{\partial \sigma^*}{\partial \bar{\epsilon}^{pl}} \quad (21)$$

Details of the stress update algorithm are shown in Lindgren *et al* (2008).

2.2 The Johnson-Cook plasticity model

The phenomenological Johnson-Cook (1983) plasticity model is commonly used in FE simulations of metal cutting. In the study by Shatla *et al* (2001), Özel and Zeren (2004) a modification of the JC model was applied to develop the methodology of flow stress determination for metal cutting simulations. Mabrouki and Rigal (2006) investigated thermo-mechanical effects during chip formation using this model. Nasr *et al* (2007) used the JC model to simulate the effects of tool-edge radius on residual stresses. Calamaz *et al* (2008) introduced a strain softening effect in a modified JC model to predict the saw-tooth chip formation. The JC model assumes an independent effect of the strains, strain rates, and the temperatures. The model provides numerical stability and shows good fit to measured stress-strain data within a limited experimental range of strains, strain rates, and temperatures. The model is lacking the capability to capture the complex effects that are common in machining, see Guo *et al* (2006). In the classical form, the flow stress σ_y is expressed as

$$\sigma_y = \left(A + B \bar{\epsilon}^{pl n} \right) \left[1 + C \ln \left(\frac{\dot{\bar{\epsilon}}^{pl}}{\dot{\bar{\epsilon}}_{ref}} \right) \right] \left[1 - \left(\frac{T - T_{room}}{T_{melt} - T_{room}} \right)^m \right] \quad (22)$$

The parameter A is related to the initial yield strength at room temperature, $\bar{\epsilon}^{pl}$ is the effective plastic strain, $\dot{\bar{\epsilon}}^{pl}$ is the effective plastic strain rate, $\dot{\bar{\epsilon}}_{ref}$ represents the highest strain rate for which no rate adjustment to the flow stress is needed, T_{melt} is a melt temperature. Parameters A , B , C , n , m are user defined material constants. The expression in the first bracket of (22) gives a nonlinear hardening law; the expressions in the second and third bracket represent the effects of strain rate and temperature, respectively.

3. Experimental procedures

An austenitic stainless steel SANMAC 316L which is a machinability improved steel grade of AISI 316L was used in the experimental study. The chemical composition is given in table 1. The material parameters at room temperature are presented in A1.

Table 1. Chemical composition of SANMAC 316L wt (%)

C	Si	Mn	P	S	Cr	Ni	Mo	V	N
0.009	0.31	1.71	0.031	0.023	16.86	10.25	2.04	0.048	0.040

The hot worked steel bar was annealed, straightened, peel turned and polished to final delivery dimensions with a diameter of 190 mm. Several orthogonal turning and quick-stop tests were performed in order to measure cutting forces and to capture morphology of the chip. All cutting tests were performed on specimens with an outer diameter of 170 mm after the hardened surface was removed.

In order to characterize the mechanical properties at the position where the forces were measured, quasi-static uni-axial tension tests were performed in the longitudinal and the transversal directions of the test bar. The average value of the yield strength and the tensile strength were found to be 276 (MPa) and 541 (MPa) respectively in the longitudinal direction and 280 (MPa) and 538 (MPa) respectively in the transversal direction.

3.1 Measurements of cutting forces and quick-stop tests

All tests were performed using the triangular CVD TiCN-Al₂O₃-TiN coated insert TNMG 160408-QF in grade 4015. This coating and substrate is preferable for continuous as well as intermittent turning operations. The insert having a wedge angle of 90° was mounted on a tool holder PTGNL 3225P in order to achieve a clearance angle of 6°. The insert used had a grooved geometry made up by a radius, a primary land of 0.15 (mm) and a rake face with an active rake face angle of -6 (°) due to the tool holder. There are always some dimensional deviations associated with manufacturing. In order to characterize the actual edge geometry, the radius was measured at three positions along the cutting edge. Inserts with the edge radius of 60 (µm) were subsequently chosen for the cutting force measurements and the quick-stop tests.

Orthogonal cutting operations were performed on a George Fischer CNC turning lathe on prefabricated tubes with one closed end having an outer diameter of 170 (mm), a thickness of 3 (mm) and a length of 115 (mm). A three component Kistler dynamometer of type 9263 was used together with a 300 Hz low pass filter for measuring the cutting and feed force components. Cutting data used for both experiments and simulations are presented in table 2.

Table 2. Cutting data in experiments and simulations

Test No.	Cutting speed v_c (m/min)	Feed f_n (mm/rev)	Cutting depth a_p (mm)
1	180	0.05	3.0
2	180	0.15	3.0
3	240	0.05	3.0
4	240	0.15	3.0

The measured history of the cutting forces can be divided into four regions: the ramp-in; the dynamic response; the steady state and the ramp-out, see Ivester *et al* (2007). All evaluations were done by averaging the signal in the steady state region where the force oscillations converged towards a plateau of stable oscillations, independent of time. During the dynamic response section, which follows after the short ramp-in, the forces are reduced down to steady state conditions. The time histories of measured and simulated cutting forces are presented in figure 6.

A number of quick-stop tests were performed in order to study the chip morphology. One important prerequisite and challenge of the test is to freeze the chip formation process during cutting without affecting the cutting action and distorting the chip. This can be done by instantaneous reducing the relative velocity between the insert and the work material to zero. In this study, in-house developed quick-stop equipment based on the “shear pin” design was used; see Childs *et al.* (2000) and Satheesha *et al.* (1990). The tests were performed on the same

specimen geometry as used for the measurements of the cutting forces. When the steady state conditions in the orthogonal turning operation were reached the process was instantaneously stopped and the chip geometry evaluated. The chip was cut off and then embedded, grounded, polished and etched for further examinations in a microscope for estimations of the thickness and the shear plane angle. The chip geometry from quick-stop tests showed some serrated form. Hence, the average chip thickness was obtained from the estimated chip area and the chip length which were calculated from the microscope image.

The chip geometry for test case No 2 is shown in figure 1(a). The evaluation of the shear plane angle was done by drawing a tangent line from the cutting edge to the intersection of the undeformed surface of the work material and the chip as shown in figure 1(b).

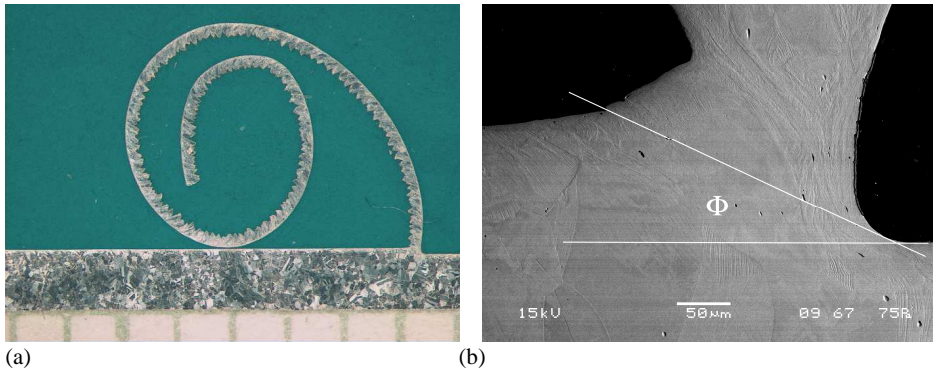


Figure 1. Quick-stop test – case No 2: (a) chip geometry, (b) evaluation of the shear plane angle from the quick-stop specimen

However, deformations along the shear plane do not generally follow straight lines which influenced the accuracy of the evaluation.

3.2 High strain rate testing

The Split-Hopkinson bar is commonly used when determining the inelastic response of metals at high strain rates. This technique has the capability to measure the response of metallic materials at strain rates up to 10^4 (s^{-1}), see Nemat-Nasser (2000). In the present work the high strain rate testing was performed using the Split-Hopkinson pressure bar (SHPB) over a broad range of temperatures and strain rates. The temperatures were ranging from room temperature up to 950 ($^{\circ}C$) and the strain rates varied up to maximum 9000 (s^{-1}).

Characteristics of Split-Hopkinson technique are that the strain and the strain rate both are affected by the impact velocity of the striker and the initial length of specimen. Different impact velocity of the striker, initial length of specimens and length of the striker were used to obtain different strains and strain rates. The impact velocity of the striker could in this case be adjusted by different settings of pressure. A more detailed description of the test equipment used in the current work is given in Apostol *et al* (2003).

The tests at elevated initial temperature were performed by pushing an arm, loaded with the specimen, into a stand alone furnace. When the desired temperature was reached, the specimen was pulled out and placed between the incident and the transmitted bars but still without physical contact. The transmitted bar was then push towards the specimen with a pneumatic manipulator

establishing contact just before the stress pulse reached the transition between the incident bar and the specimen, all in accordance to prevents thermal gradients in the specimens. The signal was measured using strain gages in front of and beyond the specimen in the incident respectively the transmitted bar. The recorded signal consisted of several frequency components. To make up for the dispersion, a fast Fourier transform (FFT) was used in the evaluation process where the frequency components were shifted, see Gorman (1983). Passive damping was used to reduce the elastic oscillations.

3.3 Calibration of material models

Very high strain rates exist in the primary and secondary shear zones while the rest of the workpiece deforms at low strain rates. The primary shear zone is where the major shearing of workpiece material occurs, in a secondary shear zone adjacent to the tool-chip interface shearing due to contact conditions takes place. Thus, tests with both low and high strain rates for varying temperatures are needed. The calibration of the DD model in Lindgren *et al.* (2008) was based on uni-axial compression tests conducted at strain rates ranging from 0.001 - 10 (s⁻¹) and temperature in the range 20 - 1300 (°C). Therefore, recalibration of the model by using additional high strain rate tests was needed.

Deformation behaviour of AISI 316L steel during machining and optimization of material parameters for the JC model were addressed in several papers. In the study conducted by Umbrello *et al.* (2007), the influence of different sets of material constants for the JC model on machining simulation of AISI316L is discussed. Determination of parameters for the JC model based on orthogonal cutting tests and analytical modelling is presented by Özel and Zeren (2004). The set of stress-strain curves used in the current study for the calibration of the JC model and the response of the model to varying load paths is presented in figure 2.

The JC model can not give a good accuracy when subjected to the entire test set. Therefore, only data from the high strain rate tests were used to calibrate the model as shown in figure 2.

Furthermore, the JC model response was never extrapolated outside the experimental range.

It was found that the hardening due to large strains but still low strain rates at the start of the simulation was too large. This prevented the initiation of chip formation. The chip formation did not proceed in a similar way as shown in figure 4b for the test case No 2 and the DD model.

Therefore, in the implementation of the JC model into MSC.Marc software, strain rates larger than 9000 (s⁻¹) were set to this cut-off value. The same was done with plastic strain. This cut-off value was 60 (%). The use of cut-off means that when evaluating the flow stress according to (22), the effective plastic strain was never larger then $\max(\bar{\epsilon}^p, 0.6)$ and its rate never higher then $\max(\dot{\bar{\epsilon}}^p, 9000)$. Thus, the actual strain and strain rate in the simulation was overruled by the cut-off limits when evaluating (22).

The obtained parameters for the JC model that were used for simulations are given in table 3.

Table 3. Material parameters for the JC model

A (MPa)	B (MPa)	<i>n</i>	<i>C</i>	$\dot{\bar{\epsilon}}_{ref}$ (s ⁻¹)	<i>m</i>	<i>T_{melt}</i> (°C)
111	358	0.49	0.257	1	0.805	1358

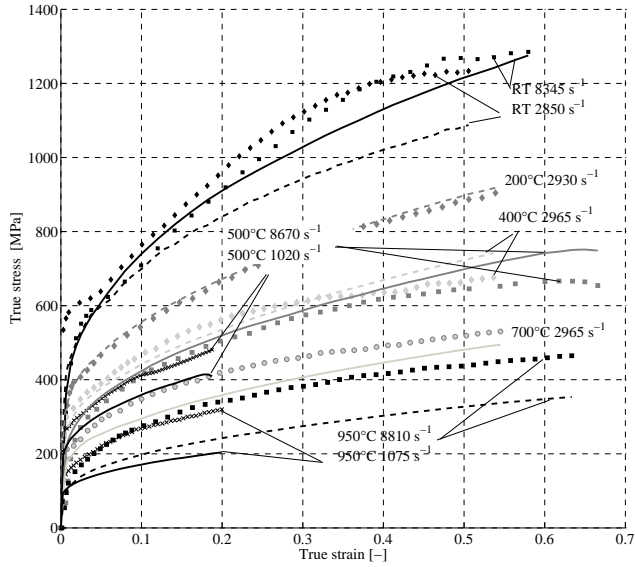


Figure 2. Flow stress curves used for calibration of the JC model. The lines are computed values.

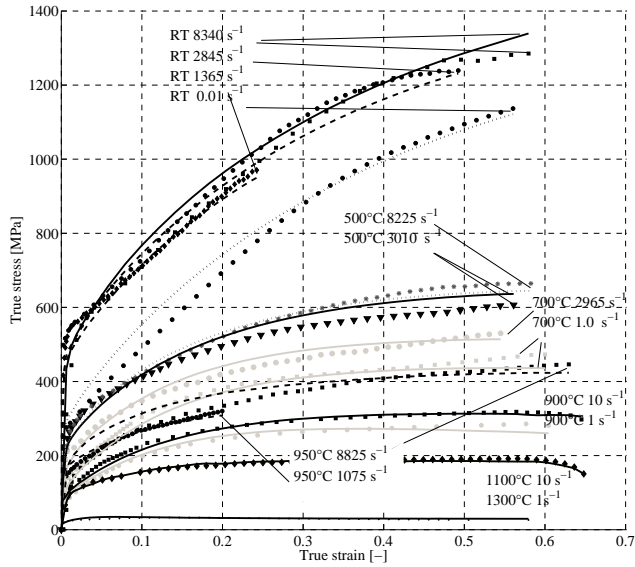


Figure 3. Flow stress curves used for calibration of the DD model. The lines are computed values.

For the calibration of the DD model, the entire test set (both low and high strain rate data) was used. The response of the DD model to varying load paths over the entire test range shown acceptable accuracy, see figure 3. The figure shows only half of the calibration set in order to make the figure readable. The excluded curves show the same quantitative agreement between model and measurements as those included in the figure. No cut-off was used in the implementation of the DD model.

The parameters obtained from low strain rate tests, including known or assumed parameters from literature, are presented in Lindgren *et al.* (2008). Temperature-dependent parameters determined by calibration of the model with Split-Hopkinson pressure bar tests are presented in A2 and A3.

4. Finite element formulation

The implicit FE software MSC.Marc was used together with an updated Lagrangian formulation accounting for large deformation and strains. The ability of Marc software to adaptively remesh is crucial in the used approach. Then, it is possible to maintain a reasonable shape of elements and also capture gradients of strain, strain rate and temperature. This remeshing strategy does not require a criterion for modelling of the chip separation from the workpiece.

A staggered step approach for coupled transient mechanical and heat transfer analysis was utilized. The full Newton-Raphson method was applied to solve the global system of equilibrium equations and the nonlinear system of equations for state variables, respectively.

The friction condition is an important factor that influences chip formation. Friction on the tool-chip interface is not constant and is a function of normal and shear stress distribution. Normal stresses are largest in the sticking contact region near the tool tip. The stress in the sliding zone along the contact interface from the tool tip to the point where the chip separates from the tool rake face is controlled by frictional shearing stress. A variety of complex friction models exists, however, the lack input data to these models is a limiting factor. The model for tool-chip interface employed in the current study is a generalized Coulomb friction model. A value for the friction coefficient was estimated from the measured force components at the tool rake angle using Merchant's theory of chip formation; see Childs *et al.* (2000). The friction coefficient $\mu = 0.5$ was taken as an average value from the whole range of cutting experiments.

The heat generated in metal cutting has a significant effect on the chip formation. The heat generation mechanisms are the plastic work done in the primary and secondary shear zones and the sliding friction in the tool-chip contact interface. Generated heat does not have sufficient time to diffuse away and temperature rise in the work material is mainly due to localized adiabatic conditions. Experimental and modelling efforts were devoted to determine the amount of dissipated energy during severe plastic deformation since Taylor and Quinney (1937) presented their work. They found that the fraction of dissipation was typically in the range [0.8, 1.0] for the materials they studied. Vivier *et al.* (2009) investigated the amount of dissipated and stored energy in structures containing frictional cracks and elasto-plastic zones and stated that the Taylor-Quinney coefficient was not a constant. Stainier and Ortiz (2010) presented the variational theory of thermo-mechanical coupling that results in precise predictions of the rate of heating due to dissipation and its dependency on the strain and the strain rate. A standard practice in FEM simulations of mechanical cutting is to assume the fraction of plastic work transformed into heat equal to 0.9, e.g. Shi *et al.* (2002), Özel (2006).

In the current study the fraction of plastic work converted into heat was assumed to be constant and equal to 90%. The heat generated by friction was also calculated and applied as a surface flux; see also Grzesik and Nieslony (2004), Abukhshim *et al.* (2006) and Dogu *et al.* (2006). The heat generation conversion factor between energy due to friction and heat generated in a coupled contact analysis was assumed to be equal to 0.9, default value in MSC.Marc software.

Chip formation is also influenced by the contact heat transfer coefficient. Different values were reported, such as 1×10^5 (W/m² °C) in Özel (2006) or 50×10^6 (W/m² °C) in Mabrouki *et al* (2006). A number of numerical trials were run with varying values of the heat transfer coefficient to obtain a homogeneous temperature field across the nearest region of the contact. The value 5×10^6 (W/m² °C) was used in the presented work.

An orthogonal cutting operation was employed to mimic 2D plane strain conditions. The depth of cut, used for all test cases, was equal to 3 (mm). Coupled thermo-mechanical plane strain elements were used for the discretization of the workpiece and the tool, respectively. Fully integrated bilinear quadrilateral thermo-mechanical elements were used for the workpiece. The mean dilatational formulation and constant temperature distribution over the element were used to avoid a problem with incompressibility. The initial mesh was defined by 900 elements, see figure 4a. The tool geometry was discretized by 2298 tree-node thermo-mechanical elements. The dimension of the workpiece in the FEM model was 8x1.6 (mm). A horizontal velocity corresponding to the cutting speed was applied to the nodes at the bottom of the workpiece. The nodes along the horizontal and vertical outer edges of the tool were fixed.

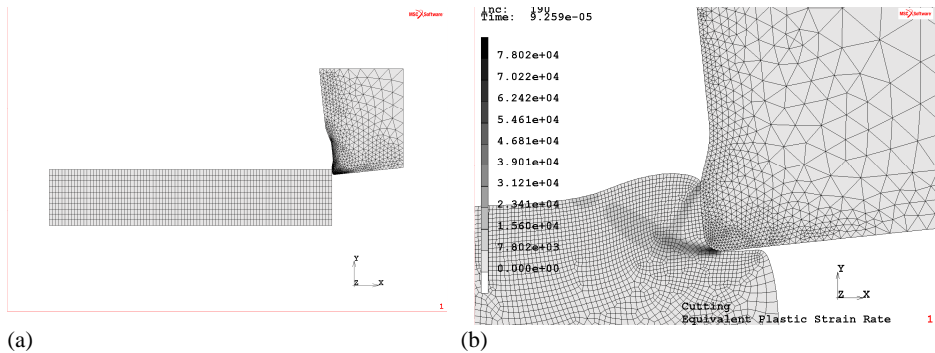


Figure 4. 2D plane strain FE model of orthogonal cutting: (a) initial mesh, (b) initiation of the chip

Due to adaptive remeshing, the average number of elements increased up to 14 000. The effect of remeshing near the tool tip is illustrated in figures 4(b), 5(a)-(b) for the test case No 2 with the DD model. The mesh adaptivity was controlled by the global remeshing parameters. Elements having the effective size larger than 0.1 (mm) were automatically remeshed. The lower bound for element size was 2.5 (μm). This element size is approximately equal to the shortest tool element edge in the tool-chip contact. Furthermore, the mesh was updated every fourth increment to prevent the severe element distortion.

The adaptive time stepping procedure with multi-criteria such as automatic reducing/increasing time step size was used to control the analysis. Initial time step size equal to 10^{-10} (sec) was increased to 10^{-6} (sec) during the steady state part of the simulation.

Material properties for the workpiece material are shown in A1. Material properties of the tool were assumed thermo-elastic.

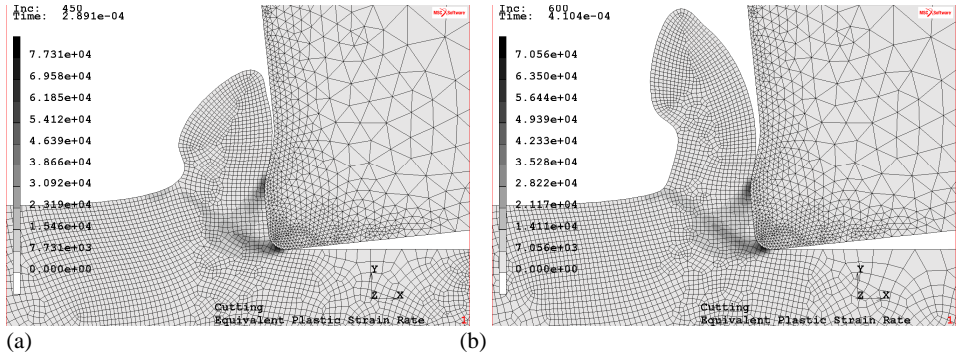


Figure 5. Intermediate stages of the chip formation: (a) time 9.251e-5 (sec), (b) time 2.891e-4 (sec)

5. Results

Finite element simulations were carried out for the cutting data that were used for the experiments. Observations on the formation of chips and forces needed to create them are compared with simulation results in the next section.

5.1 Cutting forces

The measured histories of cutting force F_c and feed force F_f for the test case No 2 are shown in figure 6(a). The force values presented in table 4 were evaluated by averaging the measured signal in the steady state region. The steady state in the experiment was reached approximately during 3 (sec) after the start of measurements.

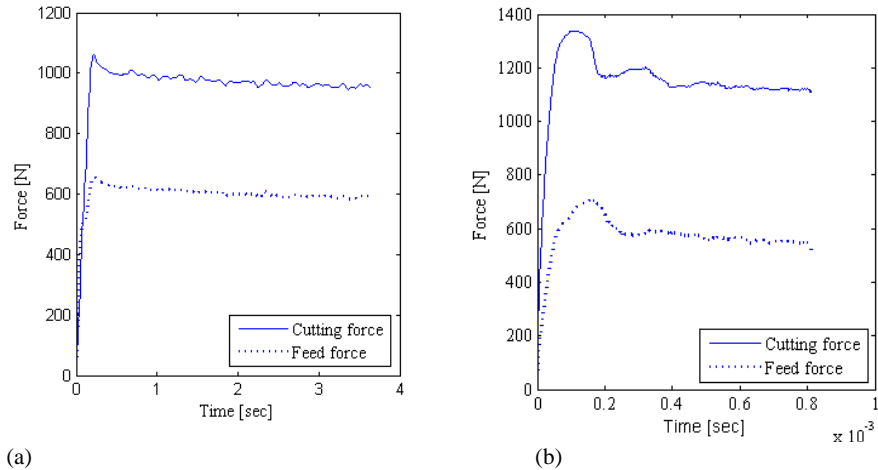


Figure 6. Cutting force F_c and feed force F_f - test case No 2; (a) measured, (b) simulated

The loading histories of simulated forces, see figure 6(b), were evaluated at the chip tool interface. Average values of the computed forces in the steady state region are compared with the experimental results in table 4. The error used for the evaluation of the computed results is defined as

$$e = \frac{\text{Computed} - \text{Measured}}{\text{Measured}} \times 100\% \quad (23)$$

Table 4. Measured and simulated cutting forces

Test No.	Measured			Simulated JC			Simulated DD			
	F_c (N)	F_f (N)	F_c (N)	e (%)	F_f (N)	e (%)	F_c (N)	e (%)	F_f (N)	e (%)
1	446	437	425	-4.7	350	-19.9	485	8.7	400	-8.5
2	960	592	1065	10.9	515	-13.0	1100	14.6	545	-7.9
3	442	439	440	-0.5	355	-19.4	480	8.6	390	-11.2
4	929	560	1050	13.0	510	-8.9	1075	15.7	530	-5.4

5.2 Chip geometry and shear plane angle

The formation of the chip involves a shearing of the workpiece material at the shear plane, the region of progressive plastic deformations extending from the tool edge to the position where the upper surface of the chip leaves the work surface. The highest strain rates are localized into a narrow band starting in front of the tool edge radius. They are significantly larger in the primary shear zone than in the remaining material, see figure 7.

The chip formation was simulated as a continuous process without taking into account any damage criteria. The chip geometry from the quick-stop test was compared with simulated results achieved by the DD model and by the JC model. The simulated chip thickness was obtained by averaging values evaluated at three subsequent sections along the chip edge. Measured and simulated chip thicknesses are presented in table 5.

The shear plane angle was estimated using strain rate plots according to figure 7. Measured and simulated values of the shear plane angle are also presented in table 5. The error in the computed chip thickness and shear plane angle was evaluated using (23).

Table 5. Measured and simulated chip thickness t and shear plane angle ϕ respectively

Test No.	Measured			Simulated JC			Simulated DD			
	t (mm)	ϕ (°)	t (mm)	e (%)	ϕ (°)	e (%)	t (mm)	e (%)	ϕ (°)	e (%)
1	0.129	20	0.095	-26.4	34	70.0	0.102	-20.9	23	15.0
2	0.198	23	0.294	48.5	33	43.5	0.241	21.7	25	8.7
3	0.119	27	0.111	-6.7	26	-3.7	0.097	-18.5	31	14.8
4	0.203	28	0.293	44.3	32	14.3	0.240	18.2	32	14.3

5.3 Material response

All figures presented in this section correspond to the steady state conditions. The results shown are for the cutting velocity of 180 (m/min) and feed of 0.15 (mm). Results from the DD model and the JC model are presented side by side. Figure 7 illustrates distribution of effective plastic strain rates in the primary and secondary shear zones. Figure 7(a) presents a maximum plastic strain rate value of $68000 \text{ (s}^{-1}\text{)}$ calculated by the DD model. The distribution of plastic strain rates having a maximum value of $70\,000 \text{ (s}^{-1}\text{)}$ calculated using the JC model is shown in figure 7(b).

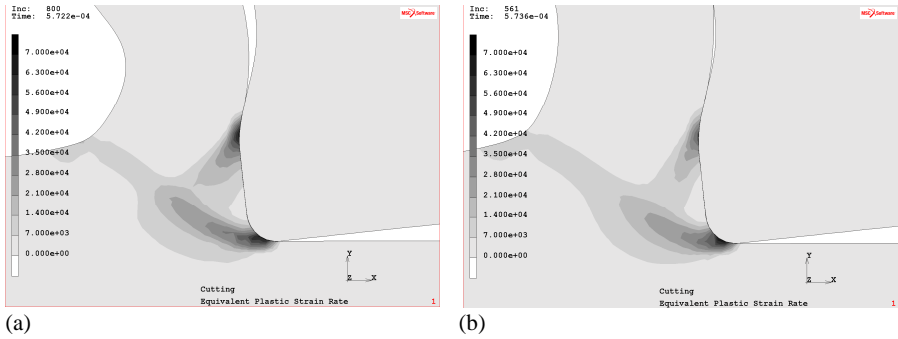


Figure 7. Effective plastic strain rate; (a) the DD model, (b) the JC model.

Temperature fields are presented in figure 8. Maximum temperature was generated in the contact between chip and rake face of the tool. Figure 8(a) shows the temperature field generated by the DD model with a maximum value of $695 \text{ (}^{\circ}\text{C)}$, temperature distribution related to the JC model having maximum of $673 \text{ (}^{\circ}\text{C)}$ is shown in figure 8(b).

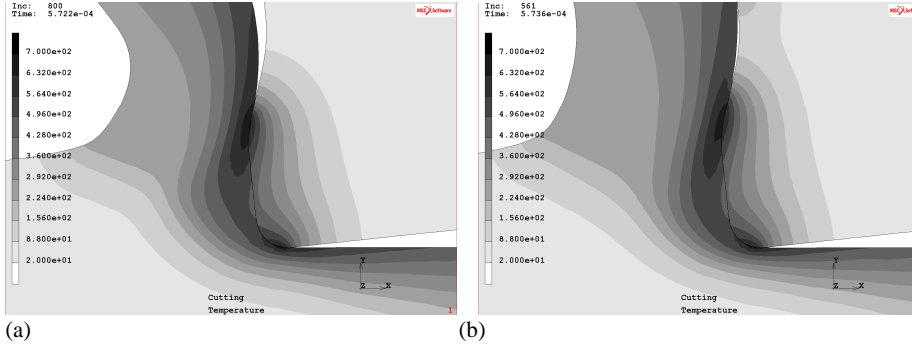


Figure 8. Temperature distribution; (a) the DD model, (b) the JC model.

The material response simulated by the DD model during the dynamic loading history is controlled by the state variables. The vacancy concentration and the dislocation density are shown in figure 9. In the domains of highest temperature concentrated close to the tool rake face, see figure 8(a), the significant generation of vacancies coupled with the dislocation recovery is present, see figure 9(a). In the area close to the outer surface of the formed chip with lower

temperature level, the increased dislocation density controls the hardening, figure 9(b). Initial value of dislocation density 10^{12} (m/mm³) was increased up to 10^{15} (m/mm³).

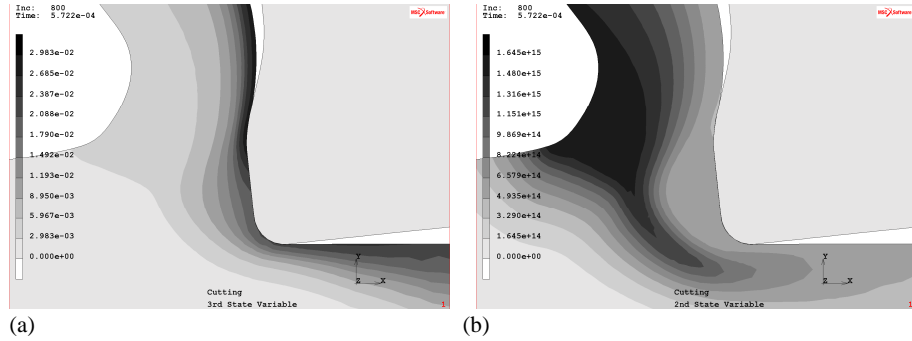


Figure 9. State variables for the DD model; (a) vacancy concentration, (b) dislocation density

6. Discussions and conclusions

The aim of the presented work was to compare the predictive capability of the DD model with the JC model. The scope of the evaluated models was to predict chip formation in terms of chip thickness and shear plane angle, and cutting forces.

The numerical problems in modelling the cutting process are numerous, particularly the need for reliable remeshing and contact algorithms. The solution for cutting forces and chip formation are strongly influenced by criteria for the element size as well as time stepping. A number of numerical experiments were run to determine the parameters for a stable solution. Remeshing of the work material was controlled by a set of control parameters. Tool penetration into the work material was suppressed. When it occurred, the work material was remeshed and a new boundary in the tool-chip contact was determined. A minimum element edge length $2.5e-3$ (μm) was used for the remeshing of the workpiece.

Other parameters influencing the chip form and the level of simulated forces are convergence criteria. Default values in Marc software, residual checking (relative force tolerance 0.1) together with displacement checking (relative displacements tolerance 0.1) resulted in cutting force F_c equal to 1155 (N) and feed force F_f equal to 555 (N) for the test case No 2. The modification of these criteria, (relative force tolerance 0.01) and (relative displacements tolerance 0.01), provided 5% change in the cutting force and 2% change in the feed force. The latter values of convergence criteria proved to be acceptable for sufficient accuracy.

It can be concluded that using mesh and convergence criteria that capture local effects in shear zones are important factors for a sufficient valid and accurate model.

Forces were slightly better predicted by the DD model. The feed force was underestimated by the DD model by about 10 (%), largest deviation of the feed force predicted by the JC model was 20 (%). The largest error in the cutting force predicted by the DD model was 15.7 (%). The JC model both overestimated and underestimated the cutting force with a largest deviation of 13 (%). The DD model shows also good prediction capability of the chip morphology in comparison with the JC model. Largest error of the chip thickness was predicted by the JC model for the cutting speed 180 (m/min) and feed 0.15 (mm). The shear plane angle was overestimated the most by the JC model by about 70 (%) for cutting speed 180 (m/min) and feed 0.05 (mm). The discrepancy in the simulated results can be related to the fact that the chip formation was simulated as a continuous process and no strain softening or damage was included.

The question whether the models are useful for evaluating cutting forces and chip geometry for a given tool design, depends naturally on the context. Sometimes it is sufficient to have a model that gives a qualitative correct answer. However, during later design stages, then more quantitative correct results are required. The errors in tables 4 and 5 must be related to the context where they will be used, namely the cutting tool manufacturing industry. Results in Lindgren *et al.* (2009) indicates that variations in tool radius in the industrial production of nominally identical cutting tool as well as variations in material properties of nominally the same workpieces can cause variations around 10% in forces. We then estimated that errors below 10% indicate a model fit for the purpose. The dislocation density model can predict forces near the wanted precision.

Both material models were calibrated with SHPB test for strain rates up to 9000 (s^{-1}). It is obvious that the calculated values of the plastic strain rate gained by both material models are significantly larger than the experimental range. Physically based plasticity models are supposed to have larger domain of validity and can be extrapolated outside their range of calibration. But, this requires that the mechanisms controlling the deformation in the calibration set are still dominating in the extrapolated range. The model presented in Lindgren *et al.* (2008) was used without any particular mechanisms to account for very high strain rates. Future work will address implementation of those particular mechanisms which are significant for high strain rate deformations such as phonon or electron drags as discussed in Frost and Ashby (1982), Regazzoni *et al* (1987), Guo and Nemat-Nasser (2006).

Acknowledgements

The presented work is a part of the project financed by the Swedish Research Council and AB Sandvik Coromant. The authors would also like to thank Veli-Tapani Kuokkala and Jari Rämö, Tampere University of Technology Finland, for their technical assistance with the high strain rate testing.

References

- Abukhshim N A, Mativenga P T and Sheikh M A 2006 Heat generation and temperature prediction in metal cutting: A review and implications for high speed machining *Int Journal Machine Tools & Manufacture* **45** 1687-1695
- Apostol M, Vuoristo T and Kuokkala V-T 2003 High temperature high strain rate testing with a compressive SHPB *Journal de Physique IV* **110** 459-464
- Bammann D J, Chiesa M L and Johnson 1996 Modeling large deformation and failure in manufacturing processes *Tatsumi T et al, eds, Theor App Mech* 359-376
- Bergström Y 1969/70 Dislocation model for the stress-strain behaviour of polycrystalline alpha-iron with special emphasis on the variation of the densities of immobile and immobile dislocations *Materials Science & Engineering* **5** 193-200
- Bergström Y 1983 The plastic deformation of metals – a dislocation model and its applicability *Reviews on powder metallurgy and physical ceramics* **2/3** 79-265

- Bil H, Engin S and Erman Tekkaya A 2004 A comparison of orthogonal cutting data from experiments with three different finite element models *Int Journal Machine Tools & Manufacture* **44** 933-44
- Calamaz M, Coupard D and Girot F 2008 A new material model for 2D numerical simulation of serrated chip formation when machining titanium alloy Ti6Al4V *Int Journal Machine Tools & Manufacture* **48** 275-288
- Childs T, Maekawa K, Obikawa T and Yamane Y 2000 *Metal machining - Theory and applications* Arnold Publishers (London)
- Dogu Y, Aslan E and Camuscu N 2006 A numerical model to determine temperature distribution in orthogonal metal cutting *Journal Materials Processing Technology* **171** 1-9
- Estrin Y 1998 Dislocation theory based constitutive modelling: foundations and applications *Journal of Materials Processing Technology* **80-81** 33-39
- Estrin Y 2003 High temperature plasticity of metallic materials *Finel A et al eds, Thermodynamics, Microstructure and Plasticity* **108** Kluwer Academic Publications 217-238
- Follansbee P S and Kocks U F 1988 A constitutive description of the deformation of copper based on the use of the mechanical threshold stress as an internal state variable *Acta Metall* **36** 81-93
- Frost H J and Ashby M F 1982 *Deformation mechanism maps - The plasticity and creep of metals and ceramics* Pergamon Press (Oxford)
- Gorman D 1983 A numerical method for the correction of dispersion in pressure bar signals *Journal of Physics E: Scientific Instruments* **16** 477-479
- Grzesik W and Nieslony P 2004 Physics based modelling of interface temperatures in machining with multilayer coated tools at moderate cutting speed *Int Journal Machine Tools & Manufacture* **44** 889-901
- Guo W-G and Nemat-Nasser S 2006 Flow stress of Nitronic-50 stainless steel over a wide range of strain rates and temperatures *Mechanics of Materials* **38** 1090-103
- Guo Y B, Wen Q and Woodbury K A 2006 Dynamic material behaviour modelling using internal state variable plasticity and its application in hard machining simulations *Journal of Manufacturing Science & Engineering ASME* **128** 749-759
- Ivester R, Whiteman E, Heigel J, Marusich T and Arthur C 2007 Measuring chip segmentation by high-speed microvideography and comparison to finite element modelling simulation *Proc 10th CIRP International workshop on modelling of machining operations (Reggio Calabria)*
- Jaspers S P F C and Dautzenberg J H 2002 Material behaviour in conditions similar to metal cutting: flow stress in primary shear zone *Journal Materials Processing Technology* **122** 322-330

- Johnson G R and Cook W H 1983 A constitutive model and data for metals subjected to large strains, high strain rate, and temperatures *Proc. International Symposium on Ballistics (Hague)* 1-7
- Lindgren L-E, Domkin K and Hanson S 2008 Dislocations, vacancies and solute diffusion in a physically based plasticity model for AISI 316L *Mechanics of Materials* **40** 907-19
- Lindgren L-E, Wedberg D and Svoboda A 2009 Verification and validation of machining simulations for sufficient accuracy *Proc. International Conference on Computational Plasticity COMPLAS X 2009 (Barcelona)*
- Mabrouki T and Rigal J-F 2006 A contribution to a qualitative understanding of thermo-mechanical effects during chip formation in hard turning *Journal Materials Processing Technology* **176** 214-21
- Meyers M A, Benson D J, Vöhringer O, Kad B K, Xue Q and Fu H-H 2002 Constitutive description of dynamic deformation: physically-based mechanisms *Material Science and Engineering* **A322** 194-216
- Militzer M, Sun W and Jonas J 1994 Modelling the effect of deformation-induced vacancies on segregation and precipitation *Acta Metallurgica et Materialia* **42** 133-144
- Nasr M N A, Ng E-G and Elbestawi M A 2007 Modelling the effects of tool-edge radius on residual stresses when orthogonal cutting AISI 316L *Int Journal Machine Tools & Manufacture* **47** 401-411
- Nemat-Nasser S 2000 Introduction to High strain rate testing *ASM Handbook Volume 8 Mechanical Testing and Evaluation*
- Nemat-Nasser S, Guo W-G and Kihl D P 2001 Thermo-mechanical response of AL-6XN stainless steel over a wide range of strain rates and temperatures *Journal of the Mechanics and Physics of Solids* **49** 1823-1846
- Özel T (2006) The influence of friction models on finite element simulations of machining *Int Journal Machine Tools & Manufacture* **46** 518-30
- Özel T and Zeren E 2004 Determination of work material flow stress and friction for FEA of machining using orthogonal cutting tests *Journal Materials Processing Technology* **153** 1019-1025
- Regazzoni G, Kocks U F and Follansbee P S 1987 Dislocation kinetics at high strain rate *Acta Metall* **35** 2865-2875
- Satheesha M, Jain V K and Kumar P 1990 Design and development of a quick-stop device (QSD) *Precision Engineering* **12** 205-212
- Shatla M, Kerk Ch and Altan T 2001 Process modelling in machining. Part I: determination of flow stress data *Int Journal Machine Tools & Manufacture* **41** 1511-1534
- Shi G, Deng X and Shet Ch 2002 A finite element study of the effect of friction in orthogonal metal cutting *Finite Elements in Analysis and Design* **38** 863-883

- Stainier L and Ortiz M 2010 Study and validation of a variational theory of thermo-mechanical coupling in finite visco-plasticity *Int Journal Solids and Structures* **47** 705-715
- Taylor G I and Quinney H 1937 The latent heat remaining in a metal after cold working *Proc. of the Royal Society of London Series A* **163** 157-181
- Umbrello D, M'Saoubi R and Outeiro J C 2007 The influence of Johnson-Cook material constant on finite element simulation of machining of AISI 316L steel *Int Journal Machine Tools & Manufacture* **47** 462-70
- Vaz Jr M, Owen D R J, Kalhori V, Lundblad M and Lindgren L-E 2007 Modelling and Simulation of Machining Processes *Arch. Computer Methods Engineering* **14** 173-204
- Vivier G, Trumel H and Hild F 2009 On the stored and dissipated energies in heterogeneous rate-independent systems: theory and simple examples *Continuum Mech Thermodyn* **20** 411-427
- Zerilli F J and Armstrong R W 1987 Dislocation-mechanics-based constitutive relations for material dynamics calculations *J Appl Phys* **61** 1816-1825

Appendix A

A1. SANMAC 316L - material parameters

Young's modulus E (GPa)	Poisson's ratio ν	Heat capacity C_p (J/kg°C)	Thermal expansion α (1/°C)	Thermal conductivity λ (W/°Cm)	Density δ (kg/m ³)
201	0.3	445	15.5e-6	14	7900

A2. Parameters determined by the calibration

Notation	Equation No.	Value	Dimension
α	2	0.4	
ρ_{i0}	Initial immobile dislocation density	1.10^{12}	m/mm ³
K_c	13		
c_γ	15		
$\hat{\tau}$	7		
ΔF	7		
Ω	14		
p	7	0.333	
q	7	1.902	

A3. Parameters determined by calibration that are temperature dependent

Temp (°C)	K_c	c_γ	$\hat{\tau}$	ΔF	Ω
20	59.73	0.0275	0.010390	0.5056	4.499
200	32.64	0.0275	0.010000	0.8609	7.329
400	56.09	0.0275	0.007392	0.9117	10.58
600	48.15	0.0275	0.005643	0.9913	10.29
700	45.69	0.0275	0.006256	0.9297	13.68
800	46.69	0.0275	0.007939	0.7789	13.54
900	55.13	0.0275	0.005409	0.6795	13.05
1100	121.1	0.0275	0.032410	0.6242	14.73
1300	200.0	0.0275	0.050000	0.6615	28.62

